In-operando characterization of transport and transformation processes in lithium-ion and metal-air battery cells

In-Operando Charakterisierung von Transport und Transformationsprozessen in Lithium-Ionen- und Metall-Luft-Batteriezellen

Von der Fakultät für Mathematik, Informatik und Naturwissenschaften der RWTH Aachen University zur Erlangung des akademischen Grades eines Doktors der Naturwissenschaften genehmigte Dissertation

vorgelegt von

Steffen Alexander Kayser, M.Sc.

aus

Düsseldorf

Berichter*:* *Prof. Dr. rer. nat. Josef Granwehr*

Prof. Dr. rer. nat. Joachim Mayer

Tag der mündlichen Prüfung*:* *21.01.2019*

Abstract

To improve the lifetime of lithium-ion batteries, a detailed understanding of degradation mechanisms is indispensable. Nuclear magnetic resonance (NMR) is able to unravel reversible as well as irreversible transient shape change mechanisms occurring in a battery cell, such as lithium microstructure growth and the formation of metallic lithium upon Li deposition on electrodes. Such investigations require gas-tight and non-metallic cell housings. This thesis reports on the development and evaluation of a cylindrical battery container in combination with a numerically optimized saddle coil that is suitable for *in-operando* NMR investigations of battery cells over hundreds of charge–discharge cycles. Alternatingly with NMR data acquisition, *in-situ* electrochemical impedance spectra (EIS) can be recorded, which allows correlative analysis of the two techniques. The reliability of the cell container is demonstrated by rate capability tests with $LiCoO_2$ (LCO) vs. Li-metal electrodes as well as a charge–discharge experiment of a LCO vs. graphite battery cell over more than 3000 hours. Long-run *in-operando* NMR measurements on a Li-metal vs. graphite cell reveal the formation and evolution of mossy and dendritic Li microstructures over a period of 1000 h, which illustrates the capabilities of NMR to identify dendrite mitigation strategies in cells operated under realistic conditions. In-operando NMR measurements on LCO vs. graphite cells revealed irreversible phase changes of the LCO material caused by high cell voltages. In a fast charging *in-operando* experiment of a LCO vs. graphite cell at -20 °C Li-plating on the graphite electrode was observed. Li-plating and the formation of Li microstructures can cause internal cell shorting and thus present a striking safety risk. Si-air battery cells, which present a more environmentally friendly alternative to Li-ion cells, were investigated by ^{29}Si NMR measurements. First the corrosion reaction of Si-wafer anodes in different aqueous KOH electrolytes and the resulting silicate compositions were studied. The growth of the corrosion products was measured time-resolved at different temperatures. Furthermore, in one experiment an electrolyte additive was used to inhibit the Si corrosion. For ^{29}Si *in-operando* NMR measurements of Si-air batteries a cylindrical cell container with gas and electrolyte supply was developed. For the connection of the air cathode 1000 nm thin gold layers were used. Almost the complete consumption of the Si anode was possible upon discharging and the formation of chained, cyclic and complex silicates in a Si-air cell was observed.

The abstract was adapted from Kayser et al.[1,2]

Statement of authorship

I hereby certify that this thesis has been composed by me and is based on my own work. Except where references are made in the text of this thesis, no material, which is published somewhere else, has been used. Parts of this work have been published by me as first author[1,2]. Chapters adapted from these publications are labeled with * and reference is made in footnotes. Reference [2] refers to the preprinted e-paper version of reference [1], which was adapted to the requirements of the corresponding journal. All NMR experiments and the associated data analysis were performed by me. Numerical simulations were performed by Dr. Achim Mester and EIS data analysis was performed by Dr. Andreas Mertens.
A patent[3] about parts of the development described in this work was accepted by the German Patent and Trade Mark Office (German: Deutsches Patent- und Markenamt (DPMA)). The two technical drawings shown in Fig. 11 were adapted from this patent and were made by me. The text of the patent was written by me and adapted by Karin Hoppe. The entire work presented in this thesis was supervised and reviewed by Prof. Dr. Josef Granwehr and Prof. Dr. Rüdiger-A. Eichel.

Neuss, 30th August 2018

_____

Steffen A. Kayser

"Act always so as to increase the number of choices."

[Heinz von Foerster]

Index

Abstract 1

Statement of authorship 2

Index 4

List of abbreviations 6

1. Introduction 7

2. Basic principles 10

2.1. Battery cells 10

2.1.1. Li-ion cells 10

2.1.2. Metal-air cells 15

2.2. Nuclear magnetic resonance (NMR) 17

2.2.1. Quantum mechanical theory 17

2.2.2. Classical description, spectroscopy and basic data processing 23

2.2.3. Data analysis of *in-operando* experiments on battery cells 28

3. Experimental setup 31

3.1. Overview of the *in-operando* NMR setup 31

3.2. *In-operando* NMR battery cell container development 32

3.2.1. History of cell container design 32

3.2.2. Gas-tight Li-ion cell container 35

3.2.3. Metal-air cell container with gas and electrolyte supply 37

3.3. *In-operando* NMR probes 39

3.3.1. Cell container mounting and connections 41

3.3.2. B_1 magnetic field rf coil 43

3.4. Battery cell materials and experimental parameters 45

3.4.1. Li-ion cells 45

3.4.2. Si-air cells 47

3.4.3. Cycling protocols 48

4. Performance tests of the *in-operando* NMR setup 51

4.1. Thin-film connection sticks 51

4.2. Numerical simulations and nutation curves of the B_1-field rf coil 54

4.3. Current rate capability 55

4.4. Long-time battery operation 56

4.5. *In-situ* electrochemical impedance spectroscopy (EIS) 59

5. NMR experiments on Li-metal vs. graphite cells 61
5.1. Li microstructure formation on Li-metal electrodes 62
5.2. Long-run *in-operando* NMR of the Li microstructure growth 64
6. NMR experiments on lithium cobalt oxide (LCO) cells 67
6.1. Li microstructure formation in LCO vs. Li-metal cells 68
6.2. Standard operation and overcharging of LCO vs. graphite cells 71
6.3. Li plating on graphite electrodes at low temperature 74
7. Experiments on Si-air cells 77
7.1. Silicate compositions in aqueous KOH electrolytes 78
7.2. Time-resolved *in-situ* NMR measurements of the Si corrosion 80
7.3. *In-operando* NMR measurements of Si-air cells 86
8. Conclusion & outlook 90
9. Acknowledgement 94
10. References 95
11. List of figures 105
12. Appendix 107
12.1. Rectangular iOC for metal-air and electrolysis cells 107
12.2. iOC v.3.7 with segregated NMR reference 108
12.3. iOC v.4.1 with encapsulated NMR reference 109
12.4. Signal filtering of the battery connections 110

List of abbreviations

CAD	**C**omputer-**A**ided **D**esign
DFT	**D**iscrete **F**ourier **T**ransformation
DOS	**D**ensity **O**f **S**tates
DRT	**D**istribution of **R**elaxation **T**imes
EIS	**E**lectrochemical **I**mpedance **S**pectroscopy
EPR	**E**lectron **P**aramagnetic **R**esonance
FEM	**F**inite-**E**lement **M**ethod
FWHM	**F**ull **W**idth at **H**alf **M**aximum
FZJ	**F**orschungs**z**entrum **J**ülich (Jülich Research Centre)
HPBBHT	**H**igh-**P**ower **B**road-**B**and **H**igh-**T**emperature
IEK	**I**nstitut für **E**nergie- und **K**limaforschung (Institute of Energy and Climate Research)
iOC	**i**n-**O**perando **C**ontainer
KOH	Potassium **H**ydr**o**xide
Li	**Li**thium
LiC	**Li**thium **C**arbon
LiCl	**Li**thium **C**h**l**oride
LCO	**Li****C**o**O**$_2$ (**L**ithium **C**obalt **O**xide)
LIB	**L**ithium-**I**on **B**attery
LMO	**Li****Mg****O**$_2$ (**L**ithium **M**anganese **O**xide)
LSM	**L**aser **S**canning **M**icroscopy
MoM	**M**ethod **o**f **M**oments
MRI	**M**agnetic **R**esonance **I**maging
NEC	**N**umerical **E**lectromagnetics **C**ode
NMR	**N**uclear **M**agnetic **R**esonance
OCV	**O**pen **C**ircuit **V**oltage
PCTFE	**P**oly**c**hloro**tri****f**luoro**e**thylene
PEEK	**P**oly**e**ther**e**ther**k**etone
PEG	**P**oly**e**thylene **G**lycol
PFA	**P**er**f**luor**a**lkoxy
rf	**r**adio **f**requency
SEM	**S**canning **E**lectron **M**icroscopy
Si	**Si**licon
STRAFI	**Stra**y **Fi**eld
SW	**S**pectral **W**idth
TMS	**T**etra**m**ethyl**s**ilane
XPS	**X**-ray **P**hotoelectron **S**pectroscopy
ZEA	**Z**entralinstitut für **E**ngineering, Elektronik und **A**nalytik (Central Institute of Engineering, Electronics and Analytics)

1. Introduction*

To develop and improve state-of-the-art battery systems, a detailed understanding of degradation mechanisms is indispensable. Nuclear magnetic resonance (NMR) is able to unravel transport properties of ions in battery materials as well as reversible and irreversible transformation reactions occurring in a battery cell, such as dendrite growth in lithium-ion and corrosion products in silicon-air cells[1,4–7].

The first *in-situ* experiments on lithium-ion batteries (LIBs), reported in 2000 by Gerald et al.[8–10], were performed using coin and cylindrical cell containers with integrated NMR coils. For coin cells with metal housings, a solid copper disk inside these batteries acted simultaneously as current collector and as NMR radio frequency (rf) central conductor for excitation and detection. In the cylindrical cell design a straight centered wire was used for excitation/detection and current collection. For these *in-situ* NMR measurements the battery operation had to be stopped, but the cell was charged and discharged inside the NMR magnet.

The first *in-operando* NMR measurements were performed using a solenoid coil wherein a hermetically sealed bag containing a LIB was placed[11]. The cell was connected to a battery cycler and the NMR spectra were acquired during charging and discharging. One possible design suitable for bag cells is Bellcore's laminated cell[12], which is enclosed in heat-sealable plastic bags[13]. For the electrical connections, meshes attached to the electrodes have been generally used[14–20]. Conductive foils for the connections are possible as well, but sealing is known to be more challenging[21–23]. Bag cells are flexible and low-cost. They do not require external pressure to maintain contact, but undefined or missing pressure on the cell components can lead to increased resistance inside the battery and poor reproducibility. Because most bag materials without coating are permeable to air, the lifetime of a bag cell is rather short. For a LIB in a polyester bag a lifetime of around five days has been reported[24]. By using aluminum-coated bags, which protect the cells for a longer time but decrease the overall NMR signal intensity, the capacity fading of LIBs within 300 cycles was investigated[25].

Another promising approach for *in-operando* measurements on batteries and other electrochemical systems are cylindrical cell containers[26]. Inside the NMR magnet a horizontal or a vertical orientation is possible. The orientation of the electrodes is particularly important with regard to bulk susceptibility effects[17,24,27] and rf shielding[28]. The NMR signal of a Li-metal electrode is shifted by approximately 245 ppm in case of an orientation perpendicular to the external static magnetic field, B_0, and shifted by around 272 ppm in case of a parallel orientation. This can be attributed to the temperature independent paramagnetism of Li-metal[24]. An electrode orientation perpendicular to the direction of the oscillating magnetic rf field, B_1, leads to weak signals from the main faces of the electrodes but high signals from the edges. Using an orientation parallel to the B_1 field enables an almost uniform excitation of the electrode's main faces[27]. When the cell container is placed lying in a solenoid rf coil, disk-shaped electrodes can be oriented parallel to the B_0 field[26,29]. By using specifically designed inserts[30] for the cell assembly the electrode orientation can be turned to enable a horizontal arrangement in a solenoid rf coil[31–33]. Configurations with electrodes perpendicular to B_0 and parallel to B_1 can be realized as well by using Helmholtz, saddle, or Alderman–Grant rf coils placed around a vertically standing cylindrical cell container[9,34,35].

Numerical simulations offer great potential for the optimization of rf coils in NMR experiments. Thereby calculation of the electrode orientation dependent rf shielding and B_1 field strength becomes possible[27]. At present, the most common approach is the finite-element method (FEM) that offers a

*Adapted from Kayser et al.[1,2]

broad flexibility in the design of the electrical system and enables the analysis of effects due to dielectric materials in the vicinity of the coils[36,37]. An alternative method to optimize the impedance of an rf coil design is the method of moments (MoM) that is used in software packages such as NEC[38]. This technique, however, has been rarely used for magnetic resonance probe design to date.

The filling factor and thereby the NMR signal intensity can be enhanced by increasing the electrode separator thickness. A cylindrical container design with approximately 8 mm spacing between the electrodes was used to study the correlation between the electrolyte concentration gradient and microstructure growth on a Li-metal electrode with one-dimensional magnetic resonance imaging (MRI)[39]. Similar cylindrical setups were tested by other groups before[40,41]. Such vertically standing battery housings were used for slice selective probing of a LIB in the stray field of a permanent magnet[42,43] and in combination with an additional coil for pulsed field gradients[34,35,44]. Moreover, three-dimensional ^{1}H MRI was applied to investigate the Li microstructure growth indirectly[45]. Crucial for all types of cell containers are sealing systems, current collector design and the choice of chemically resistant materials. For cylindrical cells, wires and screws were tested as well as sealing by rings or epoxy[26,34,43,46].

Batteries containing metallic Li exhibit a very high energy density (3860 mAh/g theoretical specific capacity), yet dendrite growth prevents large cycle numbers and pose an inherent safety risk. Therefore understanding the formation of mossy and dendritic Li structures is of rising interest[15,16,19,32,47]. To our knowledge, long-time *in-operando* NMR experiments of the Li microstructure growth have not been reported so far.

For this work a gas tight NMR cell container design was developed, which enables long-time investigations. This is demonstrated by current rate capability tests, long-time (>3000 h) cycling experiment and electrochemical impedance spectroscopy (EIS). The *in-operando* NMR setup includes a customized high-power, broad-band, high-temperature probe. The *in-operando* cell container is supported by a 3D printed mount with an integrated 15 mm rf coil for NMR excitation. Since conductive parts, such as wires, current collectors and electrodes lead to disturbances of the magnetic field and screening of the NMR pulses, metallic parts in the cell containers were minimized by thin-film conductive coatings[3]. The B_1-field homogeneity of the rf coil with inserted batteries was investigated by numerical simulations and nutation experiments.

With ^{7}Li *in-operando* experiments of a Li-metal vs. graphite cell before and after a working time of 1100 h the possibility of long-run experiments is demonstrated. Thereby increasing mossy and dendritic Li microstructures with charge–discharge dependent growth and depletion are described. In addition a correlative analysis by *in-operando* NMR and high-resolution EIS was performed with another Li-metal vs. graphite cell. The high resolution becomes possible by a 2D distribution of relaxation times (DRT) calculation of the EIS data and yields the potential to identify processes relevant for the electrochemical impedance response of a battery.

In-operando NMR measurements of $LiCoO_2$ vs. graphite cells cycled in different voltage ranges are presented and reveal irreversible $LiCoO_2$ (LCO) phase changes depending on the upper cutoff voltage. Thereby it is demonstrated that such investigations might be used to determine optimal battery cycling parameters for different materials and conditions. Moreover, the formation of microstructured as well as metallic Li on a graphite electrode observed in a fast charging *in-operando* experiment of a LCO vs. graphite cell at -20 °C is described. Upon this by using NMR it may become possible to determine the

maximum charging rate without Li plating. The formation of microstructured and metallic Li can cause internal cell shorting and thus present a striking safety risk.

Si-air battery cells present a non-polluting alternative to Li-ion cells. With ^{29}Si NMR measurements the possibility to follow transformation processes in these cells is demonstrated. For the discharge operation, the greatest challenge is to distinguish between corrosion products (~95 % at.) and products from electrochemical discharge reactions (~5 % at.)[48]. To meet this problem, the corrosion reaction of Si-wafer anodes in different aqueous KOH electrolytes and the resulting silicate compositions are discussed first. Then the growth of the corrosion products measured time-resolved, at different temperatures and, in one experiment, with an electrolyte additive to inhibit the Si corrosion is described.

For *in-operando* NMR measurements of Si-air battery cells a cylindrical cell container with gas and electrolyte supply was developed. This container enables almost the complete consumption of the Si-wafer anode before the discharge current ends. For the connection of the air cathode 1000 nm thin gold layers are used. To our knowledge thereby we realized the first well performing setup for *in-operando* NMR investigations of metal-air batteries. A corresponding experiment is presented and possible mitigations to reduce corrosion reactions are discussed.

2. Basic principles

The basic principles of Li-ion and metal-air battery cells are described in chapter 2.1. To follow the electrochemical reactions in cells non-invasive NMR measurements can be performed. In chapter 2.2 the theory of nuclear spins and their NMR is discussed first. Then the data processing of a NMR measurement is described and finally the visualization of an *in-operando* NMR measurement on a battery cell is illustrated.

2.1. Battery cells

On the 20th of March 1800 Alessandro Volta (1745-1827) proposed the construction of an apparatus for current generation in a letter to the Royal Society in London. With respect to the findings of Luigi Galvani (1737-1798) this apparatus was described as an artificial electric organ and was composed of several galvanic cells connected in series. Earlier, Galvani had described the muscle contraction of frogs' legs caused by touching the legs with two different metals (a copper and an iron part), which have been electrically connected to each other by a wire. Instead of a frog leg Volta used among other things a cotton cloth soaked with saltwater to separate the two different metals from each other. Thereby the metals, called electrodes, were electrically isolated from each other but a salt-ion flow through the separator cloth was possible. By connecting the electrodes with a wire an electric circuit was closed and an ion flow between the metals could be compensated by an electron flow through the wire. This ion flow provoked the muscle contraction. Volta investigated various metal combinations and their potentials for current generation. Nowadays his setup, a stack of e.g. separated zinc and silver plates is called voltaic pile. Such an arrangement of galvanic cells connected in series is called battery. Because fuel cells are galvanic cells as well often galvanic cells of batteries are called battery cells.

2.1.1. Li-ion cells

In principle a battery cell consists of two electrodes, an electrolyte, a housing and a separator, which prevents a short circuit between the electrodes. Contacting the electrodes with a wire to connect a consumer leads to the transformation of stored chemical energy into electrical energy. The chemical reactions in a cell causing current and ion flows can be described by two spatially separated but coupled partial reactions[49]. At one electrode an oxidation takes places, thus electrons and ions are generated, e.g. for Li-metal:

$$\mathrm{Li}(s) \xrightarrow{discharge} (1-x)\mathrm{Li}(s) + x\mathrm{Li}^+(aq) + xe^-$$

with $(0 \leq x \leq 1)$, denoting the fraction of oxidized material. The whole equation may be multiplied by the number of Li atoms to give integer numbers. Solid Li is dissolved and the resulting Li-ions move through an electrically insulating separator towards the counter electrode. This is schematically illustrated in Fig. 1 for a cell with one Li-metal and one graphite electrode. At the counter electrode, electrons are used for the reduction of the Li-ions, which passed the separator. Thereby chemical energy is transformed into electrical energy. In case of a graphite electrode the reduction and storage of the Li-ions becomes possible by the intercalation between graphite sheets. The reduction reaction and thereby the uptake of electrons can be described by

$$\mathrm{C}_6(s) + x\mathrm{Li}^+(aq) + xe^- \xrightarrow{discharge} \mathrm{Li}_x\mathrm{C}_6(s)$$

with $(0 \leq x \leq 1)$. This indicates that at most one Li atom per six C atoms can be inserted into the graphite lattice giving LiC_6.

The electrode at which electrons are generated due to oxidation during the discharge is the negative pole of the cell. By convention it is called anode. The other positive electrode at which the reduction takes places is called cathode. The negative electrode has a lower reduction/oxidation potential than the positive electrode. By charging a Li-ion battery cell, the reactions at the electrodes can be reversed (see Fig. 1). At the graphite electrode an oxidation instead of a reduction takes place. Taking the name convention into account it becomes the anode during charging. Likewise at the Li-metal counter electrode a reduction of Li-ions (deposition of Li) instead of an oxidation (dissolution) takes place. The overall charge/discharge reactions can be summarized in a redox reaction for Li-metal vs. graphite cells:

$$\mathrm{Li} + \mathrm{C_6} \underset{charge}{\overset{discharge}{\rightleftharpoons}} (1-x)\mathrm{Li} + \mathrm{Li}_x\mathrm{C_6}$$

Thereby a multiple bidirectional conversion of chemical energy and electric energy is described.
The potentials for different elements and compounds can be determined experimentally and are given in the so called electrochemical potential series. Because they are referred with respect to a reference electrode (the standard hydrogen electrode) they are named standard electrode potentials E^0. The

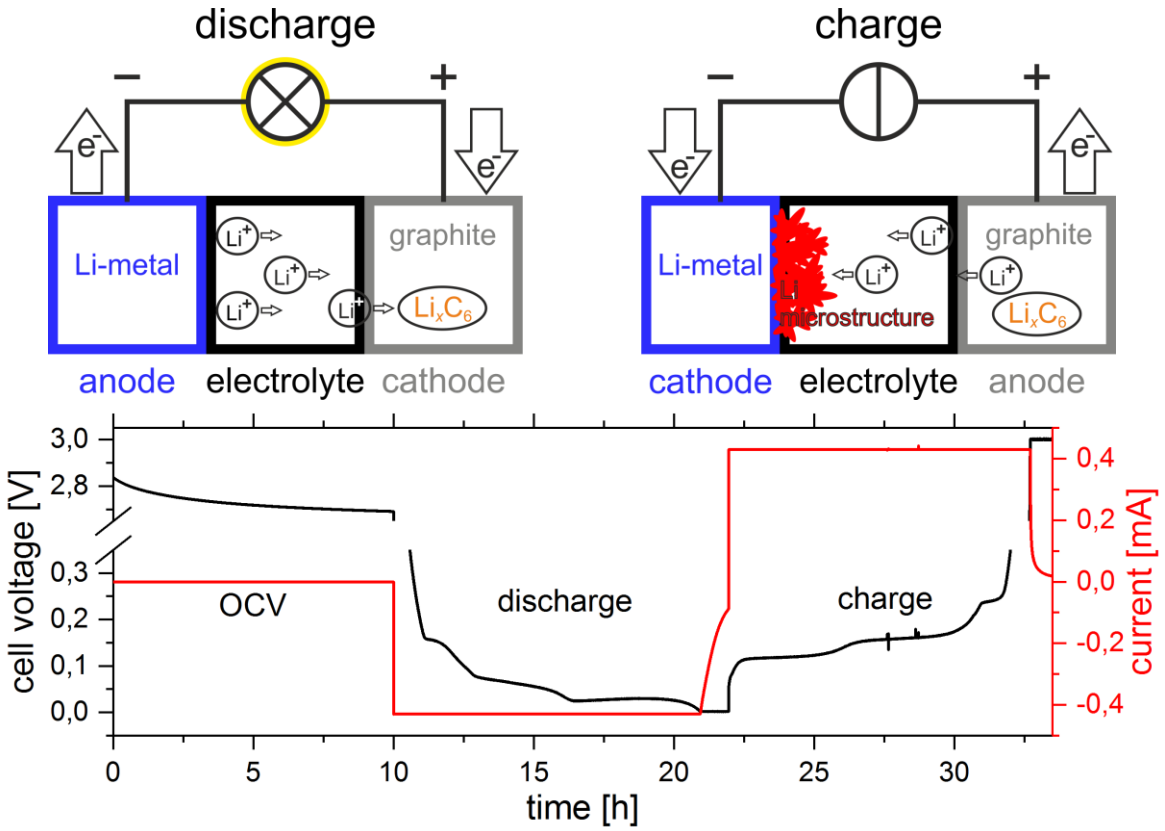

Fig. 1: Schematic drawing of transport and transformation processes in a Li-metal vs. graphite battery cell and corresponding current/voltage profiles. *<u>Top</u>: During discharging the Li-metal electrode is oxidized. Thereby positive Li-ions are released into the electrolyte and electrons are flowing through an electric cable. At the graphite electrode the Li-ions are reduced and form carbon compounds. During charging a current is applied in the opposite direction and the oxidation takes places at the graphite electrode. Thereby Li is deintercaleted out of the graphite and Li-ions are transported back to the Li-metal electrode. On metallic Li the ions are reduced and thereby deposited. This leads to a Li microstructure formation. <u>At the bottom</u>: After cell assembly the OCV without current flow starts at approximately 2.8 V. During discharging and charging voltage plateaus corresponding to the intercalation stages LiC_{18}, LiC_{12} and LiC_6 are visible (black line). The current of ± 0.43 mA corresponds to a C-rate of C/10 (see text for details). For a full delithiation or lithiation of the graphite electrode the voltage was held for 1 h at 3 V and at 1 mV, respectively.*

combination of two electrodes with different electrode potentials determines the cell voltage. Examples for E^0 of a few half reactions are[50]:

$E^0_{\mathrm{Li}} \approx$ -3.04 V for $\mathrm{Li^+} + e^- \rightleftharpoons \mathrm{Li}$

$E^0_{\mathrm{LiC_6}} \approx$ -2.84 V for $\mathrm{Li^+} + \mathrm{C_6} + e^- \rightleftharpoons \mathrm{LiC_6}$

$E^0_{\mathrm{Na}} \approx$ -2.71 V for $\mathrm{Na^+} + e^- \rightleftharpoons \mathrm{Na}$

$E^0_{\mathrm{Si}} \approx$ -1.7 V for $\mathrm{SiO_3^{2-}} + 3\mathrm{H_2O} + 4e^- \rightleftharpoons \mathrm{Si} + 6\mathrm{OH^-}$

$E^0_{\mathrm{C}} \approx$ +0.13 V for $\mathrm{C} + 4\mathrm{H^+} + e^- \rightleftharpoons \mathrm{CH_4}$

$E^0_{\mathrm{O_2}} \approx$ +0.4 V for $\mathrm{O_2} + 2\mathrm{H_2O} + 4e^- \rightleftharpoons 4\mathrm{OH^-}$

$E^0_{\mathrm{CoO_2}} \approx$ +1.42 V for $\mathrm{CoO_2} + 4\mathrm{H^+} + e^- \rightleftharpoons \mathrm{Co^{3+}} + 2\mathrm{H_2O}$

The open circuit voltage (OCV) and the voltage during discharging and charging of a Li-metal vs. graphite cell are shown in Fig. 1. Within the first 10 h OCV without any current flow a cell voltage of approximately 2.8 V is measured. Using the standard electrode potentials E^0_{Li} and $E^0_{\mathrm{LiC_6}}$ gives a theoretical Li-metal vs. graphite cell potential of approximately 0.2 V. Different effects like contact resistances, the formation of passivating layers on the electrodes and the reduction of the electrolyte components lead to deviations from the theoretical cell potential[51]. For the discharge the current is set to a constant value (red curve in Fig. 1). First, the potential drops rapidly and then voltage plateaus between 150 mV and 25 mV are observed (black curve). These plateaus can be assigned to Li intercalation stages in graphite, *i.e.* $\mathrm{LiC_{18}}$, $\mathrm{LiC_{12}}$ and $\mathrm{LiC_6}$[52–54].

The lower cut off cell voltage, at which discharging is stopped can be chosen very low, for example 10 mV. Thus, a single Li-metal vs. graphite cell has a relatively low operating voltage, which may be increased by a cell stack like the voltaic pile. For charging a constant current is applied in the opposite direction against the internal potential of the cell. The upper cut off voltage is 3.0 V.

The current generated by discharging and applied for charging is quantified by the C-rate. The C-rate is referred to the theoretical capacity of a battery cell given in mA h. A current of 1C implies a discharge duration of 1 h. For example for a theoretical cell capacity of 5 mA h a C-rate of C/10 is equal to a current of 0.5 mA. The cell capacity is determined by the amount and type of active electrode material. For example Li-metal has a molar mass of approximately 6.94 g mol^{-1} and provides one electron per nucleus. Dividing the Faraday constant F = 96485 A s mol^{-1} by this molar mass gives a specific capacity for Li-metal of 3862 A h kg^{-1}. Because the specific capacity depends on the Li density, it is lower for Li composite electrodes compared to pure Li. In addition to the specific capacity given in [mA h g^{-1}], electrode materials are specified by a volumetric capacity given in [mA h cm^{-3}], a specific and a volumetric energy density given in [W h kg^{-1}] and [W h m^{-3}], respectively, as well as a specific and a volumetric power density given in [W kg^{-1}] and [W m^{-3}], respectively.

Many electrode material properties like density, thickness and porosity influence the power density as well as the energy density.[55–57] In general, cells which exhibit a high energy density have a relatively small power density and vice versa. For a high power density many redox reactions must get past within a short time. Limiting are for example finite electron- and ion velocities in the electrodes and at phase boundaries between electrode and electrolyte. Thus, the capacity as well as the power- and energy density of a cell are always limited by the electrode with the smaller capability. It is also possible to describe an electrode material with the area capacity given in [mA h cm^{-2}]. This value varies with the

density and the thickness of the active material but can be useful for a comparison of electrodes with different sizes. Relating to this the applied current is given as current density in units of [mA cm^{-2}].

Even though metallic Li has the highest specific capacity of all Li based electrodes, its usage in Li-metal vs. graphite cells presents a striking safety risk. This is because the deposition of Li-ions on Li-metal during delithiation of the graphite electrode leads to the growth of Li microstructures[58]. These microstructures can cause a short circuit and are in the focus of chapter 5. By using battery cells without metallic Li but Li composites, this safety risk can be reduced or even avoided.

One well established Li composite battery system is graphite vs. lithium cobalt oxide ($LiCoO_2$ (LCO))[55,59,60]. This is because the standard potential of lithiated graphite (LiC_6) is only approximately 200 mV above Li-metal. LCO can be used with a graphite counter electrode (chapter 6.2), but also with a Li-metal counter electrode (chapter 6.1). For a LCO vs. graphite battery cell the electrochemical reactions are illustrated in Fig. 2. For this type of battery a formation of Li microstructure and metallic Li is found only at temperatures below 0 °C in combination with high current densities (chapter 6.3). In case of temperatures well below -20 °C, Li plating also occurs at low current densities[61].

After cell assembly a LCO cell is in the discharged stage. In other words it is at a state of charge (SOC) of 0 % and needs to be charged. The redox reaction at the LCO electrode can be describe by:

$$LiCoO_2 \underset{discharge}{\overset{charge}{\rightleftharpoons}} Li_{1-x}CoO_2 + xLi^+ + xe^-$$

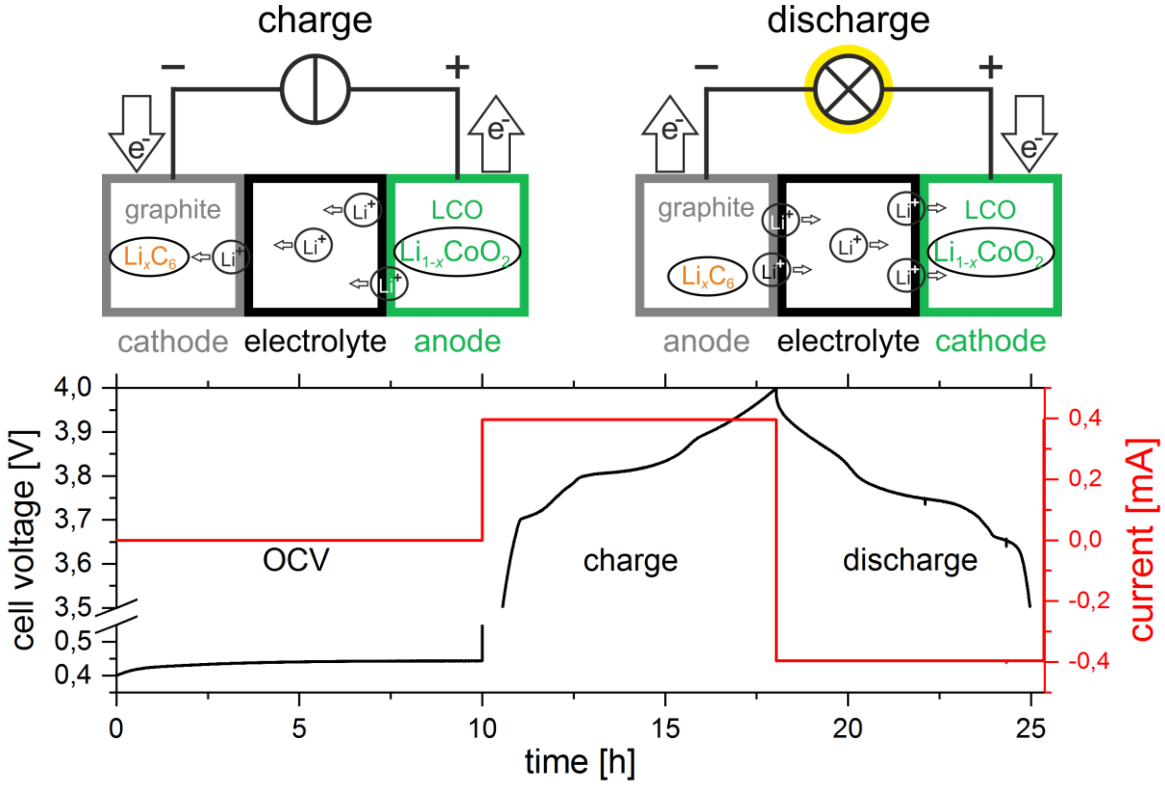

Fig. 2: Schematic drawing of transport and transformation processes in a LCO/graphite battery cell and corresponding current/voltage profiles. *Top: During the charging Li atoms of the LCO electrode are oxidized and thereby Li-ions are released into the electrolyte. At the counter electrode Li-ions are reduced and thus intercalated into graphite. During the discharging Li is deintercaleted out of the graphite by oxidation and transported back to the LCO electrode. There Li-ions are reduced to form LCO again. At the bottom: After cell assembly the OCV starts at approximately 0.4 V (black line). For cycling a voltage range of 3.0 V to 4.0 V is used and the charge/current of ±0.396 mA corresponds to a C-rate of C/10 (red line). During charging and discharging voltage plateaus corresponding to the graphite intercalation stages and staging phase transitions in Li_xCoO_2 are visible.*

By charging, LCO is oxidized and the resulting Li-ions are intercalated into graphite. The reaction at the graphite electrode is the same as for the Li-metal vs. graphite cell but the reduction takes place during the charging:

$$C_6 + xLi^+ + xe^- \underset{discharge}{\overset{charge}{\rightleftarrows}} Li_xC_6$$

The overall redox cell chemistry can be described by:

$$LiCoO_2 + C_6 \underset{discharge}{\overset{charge}{\rightleftarrows}} Li_{1-x}CoO_2 + Li_xC_6$$

The voltage profile is shown in Fig. 2. The OCV after cell assembly is approximately 0.4 V. The average cell voltage of a LCO vs. graphite cell is approximately 3.8 V[55,62].Voltage plateaus, which can be attributed to the graphite intercalation stages and staging phase transitions[63] in Li_xCoO_2, are visible during cycling. For charging, a constant current can be applied until the cell voltage has increased to 4.0 V or higher if desired. Thereby the Li content of the LCO material is decreased to around 50 %. Extracting more than 50 % of the Li leads to a capacity degradation due to non-reversible phase changes of LCO[64]. This is called overcharging and discussed in chapter 4.4 and 6.2. During discharging $Li_{1-x}CoO_2$ is electrochemically reduced back to LCO[65]. In general a lower cut off cell voltage of 3.0 V is chosen. Typical specific capacities are 350 mA h g^{-1} for graphite and 155 mA h g^{-1} for LCO[55].

To summarize, the benefits of Li-ion cells are high cell potentials, high specific energy and power densities, discharge voltage profiles with hard edges, wide temperature capabilities (especially for low temperatures) and a long storage stability (>10 years)[49,57].

2.1.2. Metal-air cells

Metal-air battery cells consist of a housing with electrolyte, a metal electrode and an air electrode, which is accessible and permeable to gas.[66,67] Charging is possible for a few times for Li-oxygen cells[68], but not for Si-air[48,69,70] or Zn-air[71]. The oxidation during the discharge takes place at the metal electrode, thus called anode. The reduction occurs at the air cathode. This is schematically shown in Fig. 3. For Li-air cells, similar as for Li-ion cells, Li can be released into the electrolyte by oxidation. In the air cathode Li-ions can react with oxygen to form LiO_2 and Li_2O_2. These reduction reactions are described by:

$$Li^+(aq) + O_2(g) + e^- \xrightarrow{discharge} LiO_2(s)$$

$$Li^+(aq) + LiO_2(s) + e^- \xrightarrow{discharge} Li_2O_2(s)$$

They take place at the so called triple phase boundary inside the air cathode[72]. In this three-phase reaction zone the liquid electrolyte, the gas and the solid cathode material, which can contain a catalyst like MgO_2, are in contact with each other such that the reduction reactions become possible. To avoid flooding or drying of the air cathode and in the same manner to generate a properly aligned triple phase boundary inside the cathode, cell parameters like e.g. electrolyte viscosity, gas pressure and electrode materials need to be adjusted.

In metal-air cells with a Si or a Zn electrode and an aqueous electrolyte the reduction reaction of oxygen and water at the triple phase boundary in the air cathode leads to a release of OH^--ions into the electrolyte:

$$O_2(g) + 2H_2O(aq) + 4e^- \xrightarrow{discharge} 4OH^-(aq)$$

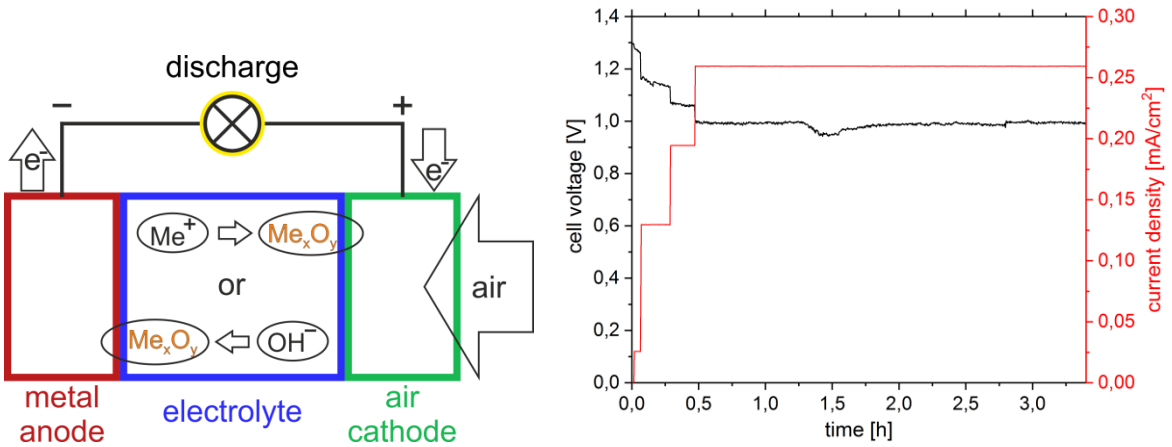

Fig. 3: Schematic drawing of two possible transport reactions in metal-air cells and discharge current/voltage profile for a Si-air cell. *Left: In metal-air cells like Li-oxygen cells the metal anode is oxidized and positive metal-ions are released into the electrolyte during the discharge. Inside the air cathode the metal-ions, electrons and oxygen form metal oxides. Charging is possible for a few times only. In metal-air cells like Si-air (and Zn-air) cells the reduction of oxygen, water and electrons takes place at the air cathode. Thereby OH^--ions are released into the aqueous electrolyte. These hydroxide ions react with the metal anode and form e.g. silicic acid, which subsequently leads to mixtures of condensed and partially protonated silicate clusters. These structures cannot be converted back to bulk metal by charging. Right: Discharge of a Si-air cell with stepwise increase of the discharge current. As usual for almost every battery, the cell voltage decreased with increasing current. In principle, discharging is possible with a constant cell voltage and until the complete metal anode is dissolved.*

The hydroxide ions can react with e.g. a Si-electrode. The corresponding oxidation at the anode is described by

$$\mathrm{Si}(s) + 4\mathrm{OH}^-(aq) \xrightarrow{discharge} \mathrm{Si(OH)_4}(aq) + 4e^-$$

For one Si atom four electrons can be generated. Using a molar weight for Si of 28.09 g mol^{-1} and the Faraday constant gives in theory a specific capacity of 3816 mA h g^{-1}. But in addition to the oxidation other reactions without electron donation occur. For example a Si corrosion reaction, which can be described by:

$$\mathrm{Si}(s) + 2\mathrm{OH}^-(aq) + 2\mathrm{H_2O}(aq) \xrightarrow{OCV\ \&\ discharge} \mathrm{SiO_2(OH)_2^{2-}}(aq) + 2\mathrm{H_2}(g)$$

The product silicic acid further reacts and mixtures of condensed and partially protonated silicate clusters are formed in the electrolyte[73]. The corrosion process starts as soon as Si comes into contact with an aqueous electrolyte[74–76]. Thereby active Si material is lost and cannot be used for the electrochemical discharge[48]. The structure and growth of the corrosion products can be determined by ^{29}Si NMR measurements. This is the topic of chapter 7. In addition to the formation of silicates the corrosion leads to an evolution of hydrogen gas. This has to be taken into account for the construction of cell housings to avoid overpressure and insulating gas accumulations at the electrodes (see chapter 3.2.3 for details).

The discharge cell voltage of a Si-air cell is shown in Fig. 3. By increasing the current density the cell voltage decreases. Above a maximum discharge current, which depends e.g. on the cell geometry and the electrolyte, the cell voltage breaks down (not shown). To avoid a gelation of the electrolyte the Si concentration should not exceed 4 mol l^{-1}[48]. To ensure this it is possible to refresh the electrolyte with a pump.

In principle a discharge is possible until the whole Si anode is consumed[48,69,77]. For example, using an aqueous 5 M KOH electrolyte and an As doped Si-wafer a mass conversion efficiency of 3 % was reported[48], resulting in a specific discharge capacity of 115 mA h g^{-1}. This indicates that after a complete dissolution of the silicon anode 97 % of the silicon material was lost by corrosion. Because a discharge current density of 0.05 mA cm^{-2} and thereby a cell voltage of approximately 1.2 V were used (for 1100 h), a specific energy of 140 W h kg^{-1} was obtained. Garamoun et al. reported a specific energy of 229 W h kg^{-1} by the use of amorphous Si and silicon carbide as fuel[77]. For comparison, commercial Zn-air cells made by e.g. Duracell exhibit energy densities of around 280 W h kg^{-1}. By incorporating electrolyte additives like polyethylene glycol (PEG) di-acid the corrosion of many metal anodes, in this work Si, can be mitigated[78–84]. This can be verified by time-resolved NMR measurements, as shown in chapter 7.2. In case of no corrosion the theoretical specific energy would be approximately 4646 W h kg^{-1}.

2.2. Nuclear magnetic resonance (NMR)

In NMR applications microscopic nuclear magnetic moments are manipulated by magnetic fields to generate measurable macroscopic effects like a current induction in a wire. The underlying microscopic effects of magnetic fields on nuclear spins can be described with the mathematics of the quantum theory in an elegant way[85]. This is briefly shown in chapter 2.2.1. Mathematics is the most powerful tool in science and this chapter shall complete the description of the physical principles this work is based on. For a basic understanding it is sufficient to skip chapter 2.2.1 and continue reading with chapter 2.2.2. In this chapter the steps from a measurement of the nuclear magnetic resonance of a macroscopic sample to a spectrum in which different chemical species and environments in the sample can be distinguished are described. Possibilities, challenges and limitations of *in-operando* NMR experiments on batteries are discussed in chapter 2.2.3.

2.2.1. Quantum mechanical theory

Elementary particles like quarks and electrons exhibit a quantum physical feature called 'spin', as they possess a feature called charge[85,86]. This spin can be interpreted as an intrinsic angular momentum of a particle but is not produced by its rotation like a rotational angular momentum. As in classical physics but quantized, a magnitude of this spin angular momentum can be indicated by assigning the particle a spin quantum number I. The SI unit of I is [kg m^2 s^{-1}] and dividing I by the reduced Planck constant $\hbar \approx 1.05 \cdot 10^{-34}$ J s gives a dimensionless number. Often the spin quantum number is simply called spin. The combination of three quarks, each with spin $I = 1/2$ forms protons and neutrons. In terms of quantum physics the alignment of the three quark spins with respect to each other can be parallel or antiparallel. Thereby two of the three quark spin angular momenta cancel out each other and the third spin results in a 'net' spin (quantum number) $I = 1/2$ for protons and neutrons. Similar to this quark quantum combination, the parallel or antiparallel combination of proton and neutron spins in a nucleus leads to a net nuclear spin I, which is equal to zero if number of protons and number of neutrons are both even. The simplest example is ^{2}H with one proton and one neutron. A parallel configuration of the two spins leads to a nuclear spin quantum number $I = 1$ and antiparallel spins result in $I = 0$.

In terms of quantum physics the spin is described by quantized energy levels. Mathematically the state of a spin of a nucleus with spin quantum number I can be described using the so called Zeeman basis with $M = (2I + 1)$ different Zeeman eigenstates. M is called the azimuthal quantum number and takes one of the values $-I, -I + 1, -I + 2, \ldots, +I$. Hence, for a spin-1/2 particle like e.g. a proton (or a ^{13}C, ^{15}N or ^{19}F nucleus) two spin eigenstates are defined using the notation $|I, M\rangle$:

$$|\alpha\rangle = \left|\tfrac{1}{2}, +\tfrac{1}{2}\right\rangle = \begin{pmatrix}1\\0\end{pmatrix} \quad \text{and} \quad |\beta\rangle = \left|\tfrac{1}{2}, -\tfrac{1}{2}\right\rangle = \begin{pmatrix}0\\1\end{pmatrix}$$

In the absence of any magnetic and electric fields the energies of the $|M|$ spin eigenstates are equal. Such energetically equal states are called degenerated. In a magnetic field with field strength B_0 a difference in energy of the spin eigenstates occurs, which is called Zeeman splitting and given by

$$\Delta E = -\hbar\gamma B_0 = \hbar\omega_L = h\nu_L$$

with the gyromagnetic ratio γ and the so called Larmor frequency ν_L. The gyromagnetic ratio γ is given by

$$\gamma = g\frac{q}{2m}$$

with the so called spin g-factor, the charge q and the mass m. The equation describing the Zeeman splitting can be derived by applying the quantum theory of spins: The spin Hamiltonian $\widehat{\mathcal{H}}_0$ for a spin-1/2 nucleus in a magnetic field in z-direction, denoted B_0, is given by

$$\widehat{\mathcal{H}}_0 = -\gamma B_0 \hat{I}_z = \omega_L \hat{I}_z$$

where $\hat{I}_z$ is the (quantum) spin operator, which can give the eigenvalue of a eigenstate. In other words, by performing the mathematical operation of $\hat{I}_z$ on a spin state, the eigenvalue of this spin (angular momentum) state is calculated. $\hat{I}_z$ and two more spin operators, $\hat{I}_x$ and $\hat{I}_y$, are used to describe the spin-1/2 angular momentum. They obey the cyclic commutation relationship for quantum operators and are given by:

$$\hat{I}_z = \frac{1}{2}\begin{pmatrix}1 & 0\\ 0 & -1\end{pmatrix} \qquad \hat{I}_x = \frac{1}{2}\begin{pmatrix}0 & 1\\ 1 & 0\end{pmatrix} \qquad \hat{I}_y = \frac{1}{2i}\begin{pmatrix}0 & 1\\ -1 & 0\end{pmatrix}$$

Thereby the corresponding eigenequations can be written as

$$\hat{I}_z|\alpha\rangle = \tfrac{1}{2}\begin{pmatrix}1 & 0\\ 0 & -1\end{pmatrix}\begin{pmatrix}1\\0\end{pmatrix} = +\tfrac{1}{2}|\alpha\rangle \qquad \text{and} \qquad \hat{I}_z|\beta\rangle = \tfrac{1}{2}\begin{pmatrix}1 & 0\\ 0 & -1\end{pmatrix}\begin{pmatrix}0\\1\end{pmatrix} = -\tfrac{1}{2}|\beta\rangle$$

with the eigenvalues +1/2 and -1/2 for the operator $\hat{I}_z$. This can be interpreted as a polarization along the axis of the magnetic field B_0, either along the positive z-axis for the spin states $|\alpha\rangle$, or along the negative z-axis for the spin states $|\beta\rangle$. Using the operators $\hat{I}_x$ and $\hat{I}_y$ to calculate the x- and y-components of the spin angular momentum of $|\alpha\rangle$ or $|\beta\rangle$ gives a fundamentally unpredictable, randomly distributed result of either +1/2 or -1/2. In other words, the z-angular momentum of a spin eigenstate is well defined, but the x- and y-angular momenta are undefined. A pictorial representation with a spin vector cannot be complete and can only indicate the direction along which the spin angular momentum is well defined and polarized. Thereby spin states cannot be interpreted spatially as in the case of classical angular momentum. There is no possibility of representing a spin state with spatial coordinates (x, y, z). A conventional angular momentum can be visualized by using spherical harmonics, but spin states may just be interpreted as their mathematical properties.

The energy of a spin state can be calculated by operating with the spin Hamiltonian $\widehat{\mathcal{H}}_0$ on it:

$$\widehat{\mathcal{H}}_0|\alpha\rangle = -\gamma B_0 \tfrac{1}{2}\begin{pmatrix}1 & 0\\ 0 & -1\end{pmatrix}\begin{pmatrix}1\\0\end{pmatrix} = -\tfrac{1}{2}\gamma B_0|\alpha\rangle \quad \text{and} \quad \widehat{\mathcal{H}}_0|\beta\rangle = -\gamma B_0 \tfrac{1}{2}\begin{pmatrix}1 & 0\\ 0 & -1\end{pmatrix}\begin{pmatrix}0\\1\end{pmatrix} = +\tfrac{1}{2}\gamma B_0|\beta\rangle$$

The eigenvalues $-\frac{1}{2}\gamma B_0 = +\frac{\omega_L}{2}$ and $+\frac{1}{2}\gamma B_0 = -\frac{\omega_L}{2}$ are the energies in units of $\hbar$ of $|\alpha\rangle$ and $|\beta\rangle$, respectively, and thereby give the Zeeman splitting $\Delta E = \hbar\omega_L$.

The evolution of a spin state $|\psi\rangle$ in a static magnetic B_0 can be described by the time-dependent Schrödinger equation

$$\frac{d}{dt}|\psi\rangle(t) = -i\widehat{\mathcal{H}}_0|\psi\rangle(t) = -i\omega_L\hat{I}_z|\psi\rangle(t)$$

which is a first-order differential equation with the solution:

$$|\psi\rangle(t_2) = e^{-i\omega_L\hat{I}_z(t_2-t_1)}|\psi\rangle(t_1) = \hat{R}_z|\psi\rangle(t_1)$$

The time τ, which elapses between the two points in time t_1 and t_2 is given by $\tau = t_2 - t_1$. By using the substitution $\omega_L(t_2 - t_1) = \omega_L\tau = \phi$ the so called rotation operator $\hat{R}_z$ can be written as:

$$\hat{R}_z(\phi) = e^{-i\phi\hat{I}_z} = \begin{pmatrix}e^{-i\frac{1}{2}\phi} & 0\\ 0 & e^{+i\frac{1}{2}\phi}\end{pmatrix}$$

ϕ can be interpreted as an angle describing the spin state 'motion'. For an elapsed time $\tau = \frac{-\pi}{2\omega_L}$ a value of $\phi = \frac{-\pi}{2}$ can be used for a simple calculation of the spin evolution. Using the eigenstate $|\alpha\rangle$ at time t_1 as a starting point, the state of this spin after the time τ is given by:

$$|\psi\rangle(t_2) = \hat{R}_z\left(\frac{-\pi}{2}\right)|\alpha\rangle(t_1) = \begin{pmatrix} e^{i\frac{\pi}{4}} & 0 \\ 0 & e^{-i\frac{\pi}{4}} \end{pmatrix}\begin{pmatrix}1\\0\end{pmatrix} = \frac{1}{\sqrt{2}}\begin{pmatrix} 1+i & 0 \\ 0 & 1-i \end{pmatrix}\begin{pmatrix}1\\0\end{pmatrix} = \frac{1}{\sqrt{2}}(1+i)\begin{pmatrix}1\\0\end{pmatrix} = e^{i\frac{\pi}{4}}|\alpha\rangle$$

The spin eigenstate after the time τ remains an eigenstate with the same eigenvalue, but is multiplied by a complex coefficient, in this example $e^{i\frac{\pi}{4}}$, which can be interpreted as a complex phase change of the spin state. Thus, the energy of a spin eigenstate in a static magnetic field is constant over time and the spin is accumulating a complex phase, as if it would perfectly spin without a polarization movement.

A spin-1/2 particle can be in a superposition of the two energy eigenstates $|\alpha\rangle$ and $|\beta\rangle$. These superposition states can be written as

$$|\psi\rangle = c_\alpha|\alpha\rangle + c_\beta|\beta\rangle = \begin{pmatrix} c_\alpha \\ c_\beta \end{pmatrix}$$

with c_β and c_β being complex superposition coefficients normalized to $|c_\alpha|^2 + \left|c_\beta\right|^2 = 1$. For an exemplary calculation of the time evolution over the interval τ the spin states $|+x\rangle, |-x\rangle, |+y\rangle$ and $|-y\rangle$ are used. They are given by the following superpositions of $|\alpha\rangle$ and $|\beta\rangle$:

$$|+x\rangle = \frac{1}{\sqrt{2}}|\alpha\rangle + \frac{1}{\sqrt{2}}|\beta\rangle = \frac{1}{\sqrt{2}}\begin{pmatrix}1\\1\end{pmatrix} \qquad |-x\rangle = \frac{-i}{\sqrt{2}}|\alpha\rangle + \frac{i}{\sqrt{2}}|\beta\rangle = \frac{1}{\sqrt{2}}\begin{pmatrix}-i\\+i\end{pmatrix}$$

$$|+y\rangle = \frac{1}{2}(1+i)|\alpha\rangle + \frac{1}{2}(1-i)|\beta\rangle = \frac{1}{2}\begin{pmatrix}1-i\\1+1\end{pmatrix} \qquad |-y\rangle = \frac{1}{2}(1+i)|\alpha\rangle + \frac{1}{2}(1-i)|\beta\rangle = \frac{1}{2}\begin{pmatrix}1+i\\1-1\end{pmatrix}$$

As for the z-component of the spin the spin operator $\hat{I}_z$ gives a well-defined eigenvalue of the states $|\alpha\rangle$ and $|\beta\rangle$, the operators $\hat{I}_x$ and $\hat{I}_y$ give well-defined eigenvalues for their eigenstates $|+x\rangle, |-x\rangle$ and $|+y\rangle, |-y\rangle$, respectively. These states may be attributed to spin states for which the x- or y-component of the spin angular momentum is well-defined. The eigenequations are given by:

$$\hat{I}_x|+x\rangle = \tfrac{1}{2}|+x\rangle \qquad \hat{I}_x|-x\rangle = -\tfrac{1}{2}|+x\rangle \qquad \hat{I}_y|+y\rangle = \tfrac{1}{2}|+y\rangle \qquad \hat{I}_y|-y\rangle = -\tfrac{1}{2}|-y\rangle$$

Superposition states do not have sharp energies. For a spin state $|+x\rangle$ the result of operator $\hat{I}_z$ as well as the result of $\hat{I}_y$ acting on $|+x\rangle$ is unpredictable.

The rotation operator $\hat{R}_z$ can be used to calculate the time evolution of a spin in a magnetic field B_0 in z-direction. Thereby, the new spin state $|\psi\rangle(t_2)$ after the time $\tau = \frac{-\pi}{2\omega_L}$ and an initial spin state $|+x\rangle$ is given by:

$$|\psi\rangle(t_2) = \hat{R}_z\left(\frac{-\pi}{2}\right)|+x\rangle(t_1) = \frac{1}{\sqrt{2}}\begin{pmatrix} 1+i & 0 \\ 0 & 1-i \end{pmatrix}\frac{1}{\sqrt{2}}\begin{pmatrix}1\\1\end{pmatrix} = \frac{1}{2}\begin{pmatrix}1+i\\1-i\end{pmatrix} = |-y\rangle$$

Thus, the state $|+x\rangle$ transforms into the state $|-y\rangle$ within the elapsed time $\tau = \frac{-\pi}{2\omega_L}$. Because ω_L was defined proportional to the magnetic field strength of B_0 the time interval between $|+x\rangle$ and $|-y\rangle$ is shorter the stronger the magnetic field is. After another time interval τ the state $|-y\rangle$ is transformed into the state $|-x\rangle$ and further on this state evolves into $|+y\rangle$. Last but not least the initial state $|+x\rangle$ is occupied again. These cyclic transformations of the spin state can be interpreted as a precession of the spin polarization in the x-y-plane around the z-axis. Within one period a time of $\left|4\frac{-\pi}{2\omega_L}\right| = \frac{1}{\nu_L}$ elapses. Thereby these calculations indicate that a spin in a superposition state is rotating with the Larmor frequency ν_L in a magnetic field. In contrast to the 'stable' Zeeman states $|\alpha\rangle$ and $|\beta\rangle$, which acquire

just a phase, the superposition spin states are dynamic. The spin angular momentum results in a nuclear magnetic moment and both are linked by:

$$\hat{\vec{\mu}}_S = \gamma\hbar\left(\hat{I}_x\vec{e}_x + \hat{I}_y\vec{e}_y + \hat{I}_z\vec{e}_z\right)$$

Taking this equation into account, the precession of the defined component of the spin angular momentum results in a similar precession of the magnetic moment generated by the spin. Thus, nuclei with a net spin unequal to zero exhibit an intrinsic magnetism.

To use these spin dynamics for NMR applications, many spins are excited into states, in which they in sum generate a measureable macroscopic magnetization, which is oscillating with a characteristic frequency ω_L. For this purpose a second oscillating magnetic field, denoted B_1, is applied via an rf pulse. The spin Hamiltonian for a spin-1/2 nucleus in a static magnetic field B_0 in combination with an oscillating magnetic field B_1 can be written as

$$\widehat{\mathcal{H}}(t) = \widehat{\mathcal{H}}_1(t) + \widehat{\mathcal{H}}_0 = \widehat{\mathcal{H}}_1(t) - \gamma B_0\hat{I}_z = \widehat{\mathcal{H}}_1(t) + \omega_L\hat{I}_z$$

where the Hamiltonian operator $\widehat{\mathcal{H}}_0$ is time-independent. The spin Hamiltonian $\widehat{\mathcal{H}}_1(t)$ for a spin interacting with an rf pulse can be approximated by

$$\begin{aligned}\widehat{\mathcal{H}}_1(t) &\cong -\tfrac{1}{2}\gamma B_1\sin(\xi_{B_0,B_1})\left(\cos\left(\omega_{rf}t + \phi_{rf}\right)\hat{I}_x + \sin\left(\omega_{rf}t + \phi_{rf}\right)\hat{I}_y\right)\\ &= -\tfrac{1}{2}\gamma B_1\,\hat{R}_z\left(\Phi_{rf}\right)\hat{I}_x\,\hat{R}_z\left(-\Phi_{rf}\right)\end{aligned}$$

with the three rf pulse parameters the peak amplitude B_1 (in units of tesla), the angular frequency ω_{rf} and the phase ϕ_{rf} as well as the substitution $\Phi_{rf} = \omega_{rf}t + \phi_{rf}$ and the angle ξ_{B_0,B_1} between the direction of B_0 and B_1. For a B_1 field vector perpendicular to B_0 the factor $\sin(\xi_{B_0,B_1})$ becomes $\sin\left(\frac{\pi}{2}\right) = 1$. Such a magnetic field can be generated by guiding the rf pulse signal through a coil. This is illustrated in Fig. 4 on the right hand side. Referring to a (stationary) fixed coordinate system the value of Φ_{rf} can be interpreted as an angle of a rotating B_1 field vector (in the x-y-plane in case of $\xi_{B_0,B_1} = 90°$). The underlying approximation assumes one resonant and one non-resonant component of the pulse, which are rotating contrariwise in the same plane, in which the magnetic field vector of B_1 is oscillating. Because the non-resonant component is neglected, the factor ½ appears in the spin Hamiltonian $\widehat{\mathcal{H}}_1(t)$.

In the so called rotating reference frame, which rotates with the rf pulse angular frequency ω_{rf} around the z-axis, $\widehat{\mathcal{H}}_0$ and $\widehat{\mathcal{H}}_1(t)$ can be rewritten as

$$\begin{aligned}\widehat{\widetilde{\mathcal{H}}}_0 &= \hat{R}_z(-\Phi)\,\widehat{\mathcal{H}}_0\,\hat{R}_z(\Phi) - \omega_{rf}\hat{I}_z = \omega_L\,\hat{R}_z(-\Phi)\,\hat{I}_z\,\hat{R}_z(\Phi) - \omega_{rf}\hat{I}_z = (\omega_L - \omega_{rf})\hat{I}_z\\ \widehat{\widetilde{\mathcal{H}}}_1 &= \hat{R}_z(-\Phi)\,\widehat{\mathcal{H}}_1(t)\,\hat{R}_z(\Phi) = -\tfrac{1}{2}\gamma B_1\,\hat{R}_z(-\Phi)\,\hat{R}_z\left(\Phi_{rf}\right)\hat{I}_x\,\hat{R}_z\left(-\Phi_{rf}\right)\hat{R}_z(\Phi)\end{aligned}$$

with the angle $\Phi(t) = \omega_{rf}t + \phi_{ref}$ between a rotating and a stationary reference frame axis. Thereby the spin Hamiltonian using the rotating frame becomes:

$$\widehat{\widetilde{\mathcal{H}}} = \widehat{\widetilde{\mathcal{H}}}_1 + \widehat{\widetilde{\mathcal{H}}}_0 = -\tfrac{1}{2}\gamma B_1\,\hat{R}_z\left(-\Phi + \Phi_{rf}\right)\hat{I}_x\,\hat{R}_z\left(\Phi - \Phi_{rf}\right) + (\omega_L - \omega_{rf})\hat{I}_z$$

Because the (resonant component of the) B_1 field is rotating with the same frequency like the reference frame, by using

$$-\Phi(\mathrm{t}) + \Phi_{rf}(t) = -\omega_{rf}t - \phi_{ref} + \omega_{rf}t + \phi_{rf} = -\phi_{ref} + \phi_{rf}$$

the spin Hamiltonian becomes time-independent:

$$\widehat{\widetilde{\mathcal{H}}} = -\tfrac{1}{2}\gamma B_1\,\hat{R}_z\left(-\phi_{ref} + \phi_{rf}\right)\hat{I}_x\,\hat{R}_z\left(\phi_{ref} - \phi_{rf}\right) + \Omega_0\hat{I}_z$$

with the frequency offset $\Omega_0 = (\omega_L - \omega_{rf})$ between Larmor frequency and rf pulse frequency. The factor

$$\left|-\tfrac{1}{2}\gamma B_1 \sin\left(\xi_{B_0,B_1}\right)\right| = \left|-\tfrac{1}{2}\gamma B_1 \sin\left(\tfrac{\pi}{2}\right)\right| = \left|-\tfrac{1}{2}\gamma B_1\right| = \omega_{nut}$$

is called nutation frequency ω_{nut} and can be interpreted as a measure for the rf field amplitude. The absolute value indicates that ω_{nut} is positive for $\gamma < 0$ as well as for $\gamma > 0$. Using a rotating frame phase of $\phi_{ref} = 0$, a nucleus with negative γ and the equations mentioned before, the final form of the time-independent rotating frame spin Hamiltonian can be written as:

$$\hat{\tilde{\mathcal{H}}} = \omega_{nut}\left(\hat{I}_x \cos(\phi_{rf}) + \hat{I}_y \sin(\phi_{rf})\right) + \Omega_0 \hat{I}_z$$

For an on-resonant pulse with $\omega_{rf} = \omega_L$ and a pulse phase of $\phi_{rf} = 0$ this spin Hamiltonian becomes:

$$\hat{\tilde{\mathcal{H}}} = \omega_{nut}\hat{I}_x$$

To calculate the time evolution of a spin state in a static magnetic field B_0 in combination with an rf pulse of the length $\tau_{rf} = t_2 - t_1$ generating the peak magnetic field amplitude B_1, the rotating frame Schrödinger equation

$$\frac{d}{dt}\left|\tilde{\psi}\right\rangle = -i\hat{\tilde{\mathcal{H}}}\left|\tilde{\psi}\right\rangle$$

can be used. The solution by direct integration is

$$\left|\tilde{\psi}\right\rangle_{t_2} = e^{-i\omega_{nut}\tau_{rf}\hat{I}_x}\left|\tilde{\psi}\right\rangle_{t_1} = \hat{R}_x(\eta_{rf})\left|\tilde{\psi}\right\rangle_{t_1}$$

with the so called pulse propagator $\hat{R}_x$ given by:

$$\hat{R}_x(\eta_{rf}) = e^{-i\omega_{nut}\tau_{rf}\hat{I}_x} = e^{-i\eta_{rf}\hat{I}_x} = \begin{pmatrix} \cos\left(\frac{\eta_{rf}}{2}\right) & -i\sin\left(\frac{\eta_{rf}}{2}\right) \\ -i\sin\left(\frac{\eta_{rf}}{2}\right) & \cos\left(\frac{\eta_{rf}}{2}\right) \end{pmatrix}$$

The substitution $\eta_{rf} = \omega_{nut}\tau_{rf}$ defines the so called flip angle η_{rf}, which is proportional to B_1 of the applied rf pulse. By using the pulse propagator $\hat{R}_x$ the effect of the B_1 field on different initial spin states $\left|\tilde{\psi}\right\rangle_{t_1}$ can be calculated. An rf pulse with the phase $\phi_{rf} = 0$ applied for a duration τ_{rf} with a peak

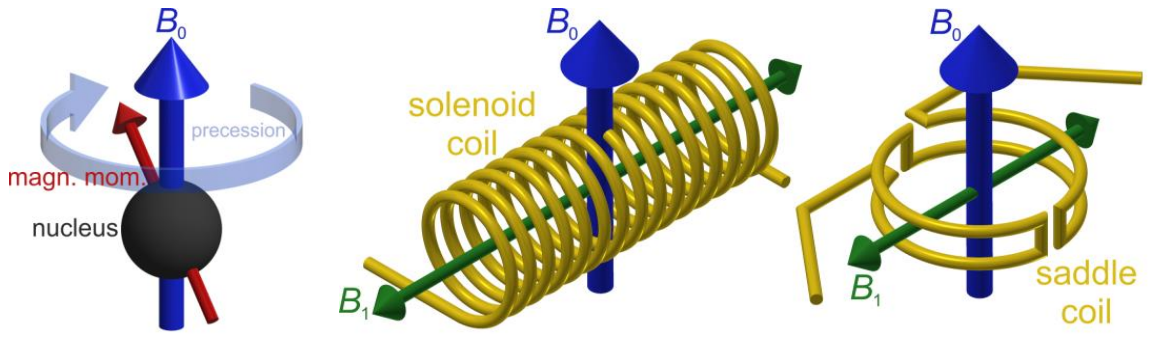

Fig. 4: Schematic drawing of a spin's magnetic moment rotating around the axis of a magnetic field B_0 and CAD drawing of two rf coils for generating an oscillating magnetic field B_1 perpendicular to B_0. *Left: The precession of a nuclear magnetic moment around the axis of an external static magnetic field B_0 (blue arrow) results from the dynamics of the spin states. The higher the magnetic field strength B_0 the fast the precession with the Larmor frequency $\omega_L = -\gamma B_0$. Center and right: By applying an oscillating magnetic field B_1 perpendicular to B_0 the spins are excited and thereby the spin's magnetic moment is rotated into the direction of the B_1 field (green arrow). This B_1 field can be realized by applying an electronic pulse on a coil. Different coil geometries are possible enabling various sample shapes and orientations.*

amplitude B_1 such that the flip angle becomes 90° (η_{rf} = π/2) excites a spin-1/2 nucleus in the initial state $|\alpha\rangle$ or $|\beta\rangle$ to a new spin state:

$$\hat{R}_x\left(\frac{\pi}{2}\right)|\alpha\rangle = \frac{1}{\sqrt{2}}\begin{pmatrix}1 & -i\\ -i & 1\end{pmatrix}\begin{pmatrix}1\\0\end{pmatrix} = \frac{1}{\sqrt{2}}\begin{pmatrix}1\\-i\end{pmatrix} = e^{-i\frac{\pi}{4}}\frac{1}{2}\begin{pmatrix}1+i\\1-i\end{pmatrix} = e^{-i\frac{\pi}{4}}|-y\rangle$$

$$\hat{R}_x\left(\frac{\pi}{2}\right)|\beta\rangle = \frac{1}{\sqrt{2}}\begin{pmatrix}1 & -i\\ -i & 1\end{pmatrix}\begin{pmatrix}0\\1\end{pmatrix} = \frac{1}{\sqrt{2}}\begin{pmatrix}-i\\1\end{pmatrix} = e^{-i\frac{\pi}{4}}\frac{1}{2}\begin{pmatrix}1-i\\1+i\end{pmatrix} = e^{-i\frac{\pi}{4}}|+y\rangle$$

Such an rf pulse is called $(\pi/2)_x$ pulse, because it rotates the polarization of the spin by π/2 around the x-axis by transforming the state $|\alpha\rangle$ into the state $|-y\rangle$ and the state $|\beta\rangle$ into the state $|+y\rangle$. The coefficient $e^{-i\frac{\pi}{4}}$ is just a phase factor. For example, the necessary peak amplitude of the B_1 field for a $(\pi/2)_x$ pulse with a pulse length of 6 µs applied on a ^{7}Li nucleus with $\gamma/2\pi \approx 16.546$ MHz T^{-1} ($\approx 10.396\cdot10^7$ rad s^{-1} T^{-1}) is given by $B_1 = \omega_{nut}/\left|-\frac{1}{2}\gamma\right|$ = (π/2)/(6 µs) / ($0.5\cdot10.396\cdot10^7$ rad s^{-1} T^{-1}) = $1/(0.25\cdot6\cdot10^{-6}\cdot10.396\cdot10^7$ T^{-1}) = 6.41 mT. This is orders of magnitude smaller than for example a B_0 field strength of 9.4 T for a ^{1}H Larmor frequency of ν_L = -42.576 MHz T^{-1} · 9.4 T ≈ 400 MHz.

Applying an rf pulse with ϕ_{rf} = 0 and a flip angle η_{rf} = π on a spin in state $|\alpha\rangle$ or $|\beta\rangle$ gives a new state:

$$\hat{R}_x(\pi)|\alpha\rangle = \begin{pmatrix}0 & -i\\ -i & 0\end{pmatrix}\begin{pmatrix}1\\0\end{pmatrix} = -i\begin{pmatrix}0\\1\end{pmatrix} = -i|\beta\rangle$$

$$\hat{R}_x(\pi)|\beta\rangle = \begin{pmatrix}0 & -i\\ -i & 0\end{pmatrix}\begin{pmatrix}0\\1\end{pmatrix} = -i\begin{pmatrix}1\\0\end{pmatrix} = -i|\alpha\rangle$$

Because the spin polarization is rotated by 180° by transforming the state $|\alpha\rangle$ into the state $|\beta\rangle$ and likewise $|\beta\rangle$ into $|\alpha\rangle$, such an rf pulse is called π_x pulse. When a π_x pulse is applied on a spin in state $|x\rangle$ the new state is given by:

$$\hat{R}_x(\pi)|+x\rangle = \begin{pmatrix}0 & -i\\ -i & 0\end{pmatrix}\frac{1}{\sqrt{2}}\begin{pmatrix}1\\1\end{pmatrix} = -i\frac{1}{\sqrt{2}}\begin{pmatrix}1\\1\end{pmatrix} = -i|+x\rangle$$

Thus, apart from a phase factor, the spin state $|+x\rangle$ is not affected by a π_x pulse.

Transforming back to the fixed frame the motion of the spin states can be described by

$$|\psi\rangle_{t_2} = \hat{R}_z(\Phi_{t_2})\,\hat{R}_x(\eta_{rf})\,\hat{R}_z(-\Phi_{t_1})\,|\psi\rangle_{t_1}$$

$$\Leftrightarrow\ |\psi\rangle_{t_2} = \hat{R}_z(\omega_{rf}t_2 + \phi_{ref})\ \hat{R}_x(\omega_{nut}\tau_{rf})\ \hat{R}_z(-\omega_{rf}t_1 - \phi_{ref})\ |\psi\rangle_{t_1}$$

with $\omega_{rf} = \omega_L = -\gamma B_0$ (in case of exact resonance) and $\omega_{nut} = \left|-\frac{1}{2}\gamma B_1\right|$. This equation describes two simultaneous spin state rotations. Because due to technical reasons the B_1 rf field strength is much smaller than the static field strength B_0, the rotation around the x-axis with ω_{nut} is much slower than the rotation around the z-axis with ω_L. Calculating the dynamics for a $(\pi/2)_x$ pulse exciting an initial state $|\alpha\rangle$ gives a sort of spiral motion on a sphere for the spin polarization vector. This is illustrated in Fig. 4 on the left hand side. For one revolution around the x-axis, the polarization vector and thereby the nuclear magnetic moment perform thousands of revolutions around the z-axis. Bit by bit the rf field excites the spins with each oscillation. A classical analog could be a child's swing, which gains momentum by pushing it on resonant. Nevertheless, in terms of quantum theory the spin polarization vector may indicate the direction in which the spin angular momentum is well defined, the momenta in the other two directions are unpredictable.

For nuclei with spin quantum numbers higher than 1/2, like ^{7}Li with I = 3/2, the quantum theory follows a similar line of argumentation to describe the spin dynamics. The corresponding equations and calculations become longer and can be found for example in ref. [85].

2.2.2. Classical description, spectroscopy and basic data processing

The distribution of occupied states of a spin-1/2 ensemble depends on the gyromagnetic ratio γ, the magnetic field strength B_0 as well as the temperature T and is described by the Boltzmann distribution

$$\frac{p_{|\alpha\rangle}}{p_{|\beta\rangle}} = e^{-\gamma\hbar\frac{B_0}{k_B T}} \approx 1 - \frac{\gamma\hbar B_0}{k_B T} \approx 1 - 6 \cdot 10^{-5}$$

with the occupation probability $p_{|\psi\rangle}$ of a spin state, the Boltzmann constant $k_B = 1.38 \cdot 10^{-23}$ J/K, a temperature of 300 K, a gyromagnetic ratio for ^{1}H of $\gamma \approx 26.75 \cdot 10^7$ rad s^{-1} T^{-1} and a B_0 field strength of 9.4 T. Thereby, in a sample with around 10^{22} nuclei per cm^3 only approximately $n = 10^{22} - 10^{22} \cdot (1 - 6 \cdot 10^{-5}) = 6 \cdot 10^{17}$ spins do not cancel each outer out and thus contribute to a macroscopic magnetization M, which is described by the Curie law:

$$M = n\frac{\gamma^2\hbar^2 B_0}{4k_B T}$$

In terms of classical physics the magnetization can be described by an angular momentum $\vec{L}$ such that the magnetization vector is given by $\vec{M} = \gamma\vec{L}$. The interaction with an rf field B_1 leads to a change of the angular momentum $\vec{L}$ according to the equation of motion:

$$\vec{M} \times \vec{B}_1 = \frac{d\vec{L}}{dt} = \frac{1}{\gamma}\frac{d\vec{M}}{dt}$$

After an excitation of spins to a new state and the corresponding change of their magnetization into the direction of the B_1 field, their initial magnetization parallel or antiparallel to the z-direction of the permanent magnetic field B_0 returns. The reason for this recovery is a time dependent change of the spin state populations due to a reestablishment of their thermal equilibrium. Moreover, the magnetization in the x-y-plane, in which the B_1 field vector oscillates, decays because the initial phase coherence of the spins is not stable in time. This is due to fluctuations of the magnetic field B_0, which leads to a loss of the spin ensemble x-y-polarization synchronization. The longitudinal z-magnetization recovery and the transversal spin-spin decoherence are described by the Bloch equations

$$\frac{d\vec{M}}{dt} = \gamma\left(\vec{M}(t) \times \vec{B}(t)\right) - \frac{M_x(t)}{T_2}\vec{e}_x - \frac{M_y(t)}{T_2}\vec{e}_y - \frac{M_z(t) - M_0}{T_1}\vec{e}_z$$

with the equilibrium nuclear z-magnetization M_0, the z-magnetization recovery (spin-lattice) relaxation time constant T_1 and the transverse (spin-spin) relaxation time constant T_2. Thereby the motion of the magnetization vector $\vec{M}$ after an rf pulse is given in the rotating frame by

$$M_x(\tau) = M_0\, sin(\Omega_0\tau)\, e^{\frac{-\tau}{T_2}}$$

$$M_y(\tau) = -M_0\, cos(\Omega_0\tau)\, e^{\frac{-\tau}{T_2}}$$

$$M_z(\tau) = M_0 - [M_0 - M_z(0)]\, e^{\frac{-\tau}{T_1}}$$

with the time τ after the rf pulse and the frequency offset $\Omega_0 = (\omega_L - \omega_{rf})$. These equations describe an exponential recovery of the z-magnetization in combination with an exponential decay of the x-y-magnetization. In the rotating frame picture the coordinate system is rotating with the Larmor frequency around the axis of B_0. This transformation simplifies the equations of motion.

The delay between two π/2-pulses should be greater than one to five times the longitudinal relaxation time constant T_1. In case of a recycle delay of $5 \cdot T_1$ between two NMR acquisitions the z-magnetization

recovery is $M_z(t_0)/M_0 > 0.99$, where t_0 is the time immediately before the subsequent pulse[87]. For Li-metal a so called saturation recovery NMR experiment gives a T_1 value of around 5 s.

As illustrated in Fig. 4, the B_1 field for excitation is generated by an rf coil. After a pulse the resulting rotation of the sample magnetization induces a current in the same rf coil used for the excitation. This oscillating current can be measured by a receiver. Assuming a strong magnetic field of a few tesla this current oscillates with a Larmor frequency ω_L in the MHz (radio)-frequency range and the measured NMR signal has the form

$$S_{FID}(t) \propto \cos(\omega_L t)\, e^{\frac{-t}{T_2}}$$

To convert such high frequency signals from analog to digital, a down-conversion of the frequency of the NMR signal can be performed by comparing it with a reference frequency signal. The hardware, which accomplishes this is called quadrature receiver and the reference frequency is the frequency of the rf pulse. The down-converted output signal S_{QR} of the quadrature receiver oscillates with a frequency, which is equal to the frequency offset Ω_0 between the reference frequency ω_{rf} and the Larmor frequency ω_L of the excited nuclei:

$$S_{QR}(t) \propto \cos(\Omega_0 t)\, e^{\frac{-t}{T_2}}$$

In practice, frequency offsets are in the kHz range, which can be handled by analog-digital converters. Using only the output signal S_{QR} it is not possible to distinguish between spins whose NMR frequencies ω_L are larger than ω_{rf} from those whose frequencies are smaller than ω_{rf} (cos(-1) = cos(+1)). Therefore, a quadrature receiver supplies two output signals of the form

$$S_A(t) \propto \cos(\Omega_0 t)\, e^{\frac{-t}{T_2}} \quad \text{and} \quad S_B(t) \propto \sin(\Omega_0 t)\, e^{\frac{-t}{T_2}}$$

which can be interpreted as a single complex signal $S_{out}(t)$ with real and imaginary components:

$$S_{out}(t) = S_A(t) + iS_B(t) \propto e^{(i\Omega_0 - T_2^{-1})t}$$

This complex representation of a NMR signal is mathematically convenient, as it enables to distinguish between positive and negative values of Ω_0. In Fig. 5 real and imaginary part of a measured NMR signal

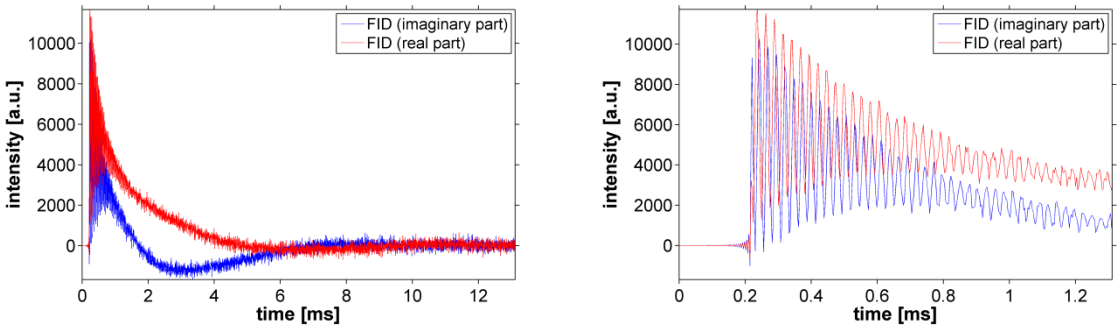

Fig. 5: Free induction decay (FID) of a measured NMR signal after a π/2-pulse. *<u>Left</u>: Full FID acquired for 13 ms. <u>Right</u>: Magnification of the left hand side. The rotation of the sample magnetization after NMR excitation induces an oscillating current in the rf coil. To enable an analog digital conversion, the frequency of the oscillation is down-converted by a quadrature receiver. Therefore the recorded NMR signal oscillates with the frequency offset Ω_0 between the pulse frequency ω_{rf} and the Larmor frequency ω_L of the excited nuclei. As described by the Bloch equation the induced signals exponentially decay. This is called the FID. Positive and negative values of Ω_0 can be distinguished by using two output signals of the quadrature receiver, which can be interpreted as a single complex NMR signal. The dead time without a signal in the first 0.2 ms is a group delay of the digital receiver and can be removed by post-processing of the data. The number of acquired data points N_{aq} in this measurement was $2^{12} = 4096$.*

are shown. The measurement shows an exponentially decaying oscillating signal as described by the Bloch equations. This is called the free induction decay (FID) of the NMR signal. Real and imaginary part of the FID in Fig. 5 are each composed of two overlapping signals with different frequency offsets Ω_0 (see right hand side): One signal is oscillating on-resonant, thus Ω_0 is close to zero and the signal decays with $e^{-\tau/T_{2,species\,1}}$. The second signal is off-resonant and thus oscillates with $\cos(\Omega_0\tau)$ in addition to its decay with $e^{-\tau/T_{2,species\,2}}$.

The frequency offset Ω_0 of a nucleus depends on its chemical environment. For example the nuclear spin of ^{7}Li in a graphite compound (LiC_6) has a different resonance frequency than the nuclear spin of ^{7}Li in Li-metal. This is because the molecular environment changes the effective B_0 field strength, which determines the Larmor frequency of a nucleus. This characteristic change of the resonance frequency is called chemical shift δ of a compound and is given in [ppm] related to a reference compound like LiCl by:

$$\delta = \frac{\nu_L^{sample} - \nu_L^{ref}}{\nu_L^{ref}}$$

The frequency shift δ of a compound given in ppm is independent of the B_0 magnetic field strength. This simplifies a comparison of NMR measurements in different magnetic fields.

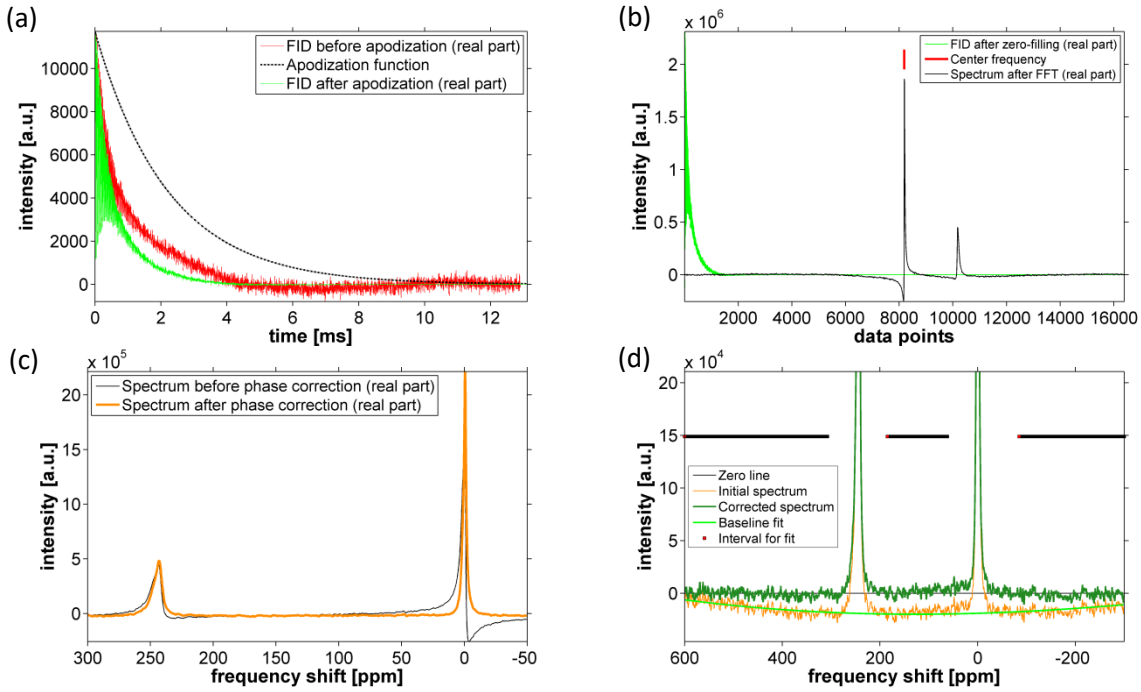

Fig. 6: Apodization, zero-filling and Fourier transformation of a FID and processing of the resulting spectrum with phase- and baseline correction. *(a) The FID (red) is multiplied by an apodization function (black dotted line) to reduce noise and to generate a vanishing intensity at the end of the processed FID (green). (b) Applying a Fourier transformation on the FID gives the intensity of signals in the FID as a function of the frequency offset. Because the number of FID data points equals the number of spectral points, the FID is enlarged by adding zeros at its end (green). This increases the digital resolution and thereby enables a smooth spectrum with for example 16384 frequency points (black). (c) By multiplication with a complex phase factors (see text) the real and imaginary part of the spectrum can be aligned such that for example the real part shows a spectrum with symmetric peaks (orange). Giving the frequency axis in units of ppm, by convention the frequency shift increases from right to left. (d) The baseline of the spectrum (orange) can be fitted with a polynomial function (light green line). By subtraction of this baseline fit the spectrum is corrected. This can be important for a further analysis of the peak integrals.*

To resolve also weak signals a FID measurement can be repeated many times. Adding the FIDs leads to an increase of the signal-to-noise ratio, ideally in proportion to the square root of the number of averaged measurements[87]. Using post-processing the noise in a measured FID can be reduced by multiplying the FID with a so called apodization function. This is shown in Fig. 6a. In this example an exponential function (black line) was multiplied with the measured FID (red line) and thereby the signal and the noise decay to zero at the end of the FID (green line).

The frequencies which a FID is composed of can be calculated by applying a Fourier transformation on the complex FID signal. This results in a complex spectrum, which gives the signal intensity as a function of the NMR frequency shift. The peaks in a spectrum have a peak width equal to $(\pi T_2)^{-1}$ in units of Hz. Because a FID apodization with an exponential function as shown in Fig. 6a shortens T_2 it broadens the peak widths. Using other apodization functions, like e.g. a growing double exponential, T_2 can be increased but the signal-to-noise ratio (SNR) is decreased. The discrete Fourier transformation (DFT) of a FID consisting of N_{aq} data points gives a spectrum with N_{aq} data points. Because usually a FID, which is measured for e.g. an acquisition time τ_{aq} of 13 ms (as shown in Fig. 6a), consists of only a few thousand data points, the FID length is extended by adding zeros at the end of the measured data to increase the digital resolution. This is called zero-filling and shown in Fig. 6b.

The frequency domain is linked to the time domain by the equation

$$SW = \frac{N_{aq}}{2 \cdot \tau_{aq}}$$

with the spectral width SW in units of Hz. (The factor 1/2 is necessary because DFT leads to a so called two-sided power spectrum. Half the energy is given at the positive frequency, and half the energy is given at the negative frequency. Therefore, the negative frequency information generated by using the DFT is redundant.) For example, using N_{aq} = 4096 points for a FID acquisition time of τ_{aq} = 13 ms the width of the spectrum after Fourier transformation becomes SW [Hz] = 157.54 kHz. In units of ppm referred to the ^{7}Li frequency of 155.53°MHz this gives a spectral width of SW [ppm] = 157.54 kHz / 155.53°MHz $\approx 1013 \cdot 10^{-6}$ = 1013 ppm. Using this value the frequency shift axis can be transformed from Hz to ppm and as a convention the direction of the axis is turned such that the ppm values increase to the left. This is shown in Fig. 6c. The zero-point of the ppm scale is set with respect to the frequency of a reference solution like 1 M LiCl in water. Thereby it becomes possible to identify the chemical compounds shown in a spectrum. The two peaks in the spectra of Fig. 6c,d at approximately 0 ppm and 246 ppm correspond to Li^+-ions in a liquid LP30 electrolyte and solid Li-metal, respectively.

Because the FID has a real and an imaginary part, the spectrum is complex as well. In general a plotted spectrum shows only the Fourier transformation of the real part of the FID signal. To show a spectrum real part with symmetric peaks, the complex spectrum is multiplied with a phase correction factor $\phi_{PC} = \cos(\varsigma) - i \cdot \sin(\varsigma)$ with $\varsigma = P_0 \cdot \pi/180° + P_1 \cdot (\delta - P_{pe})$. This phase correction does not change the absolute value of the spectrum and is shown in Fig. 6c. For a well-phased real part the zero-order phase correction value P_0 is set between 0° and 360°. The first-order phase correction value P_1 can be positive or negative and often is necessary for a sufficient phase correction of a spectrum, which shows two or more chemical species with different nutation frequencies ω_{nut}. The reason for a smaller nutation frequency of a metal compared to a liquid can be for example the skin depth of the metal. This leads to an excitation of material below the bulk surface with a weaker rf field strength (for details see chapter 2.2.1). The value P_{pe} is called pivot element and used to adjust the zero point of the first-order

phase correction. In most cases P_{pe} is chosen such that this zero point is equal to the frequency of the highest intensity peak.

Low frequency modulations and baseline distortions in the spectrum can be caused by artifacts in the first few data points of the FID[88]. Then it is justified for quantitative NMR to correct the baseline of the spectrum. Therefore, after phase correction a baseline fit is subtracted from the spectrum. An example is shown in Fig. 6d. The baseline fit can be a polynomial function of e.g. third-order given by $A{\cdot}\delta^3 + B{\cdot}\delta^2 + C{\cdot}\delta + D$. The frequency ranges with resonance signals are excluded from the baseline fit. Finally, the intensity axis of a spectrum can be rescaled e.g. for a value equal to 1 of the highest peak or by multiplication of the spectrum with a normalization factor, which refers to the intensity of an NMR intensity reference (see appendix 12.2 and 12.3). This is discussed in more detail in the next chapter 2.2.3.

In summary, after apodization, zero-filling and Fourier transformation of an FID the resulting spectrum is further processed with phase- and baseline correction as well as referencing of the frequency shift axis and intensity normalization.

2.2.3. Data analysis of *in-operando* experiments on battery cells*

To follow transport and transformation processes in battery cells, NMR spectra are acquired continuously over time during cycling of a cell. Such a measurement during battery operation is called *in-operando*. To increase the signal-to-noise ratio of the spectra it is possible to add spectra and thereby generate an average over time. This is shown in Fig. 7 for a Li-metal vs. graphite cell, which is schematically depicted in Fig. 1. In case of a 5 s delay between pulses 720 spectra per hour can be acquired. One possibility is to plot several 2D spectra on top of each other, as shown on the left hand side in Fig. 7. Another one is to use a 3D surface plot, as shown on the right hand side. The frequency dependent intensities of the time points between two spectra are interpolated to generate a 3D surface. The color encoding of the intensity enables a better visibility of small signals and a clearly visible time evolution even for a very high number of plotted spectra.

In-operando NMR measurements of Li-metal vs. graphite cells reveal the formation of Li microstructures. This is the main topic of chapter 5. To follow the signal integral evolution and to distinguish between overlapping signal, peak fitting is applied. This is shown in Fig. 8 for dendritic, mossy and metallic Li. For this work fitting was performed with Matlab. To determine the intensity integrals of the individual peaks mixed Gaussian - Lorentzian line shapes Λ given by

$$\Lambda = \frac{m}{100}\,\mathfrak{G} + \left(1 - \frac{m}{100}\right)\mathfrak{L}$$

were used. The value of m is the mixing ratio and is varied between 0 and 100. The Gaussian function $\mathfrak{G}$ and the Lorentzian function $\mathfrak{L}$ are given by

$$\mathfrak{G}(\delta) = G_{hgt}\, e^{-\left(\frac{\delta - G_{pos}}{0.6 \cdot G_{wid}}\right)^2} \qquad \text{and} \qquad \mathfrak{L}(\delta) = \frac{L_{hgt}}{1+\left(\frac{\delta - G_{pos}}{0.5 \cdot L_{wid}}\right)^2}$$

with the frequency shift δ, the peak heights G_{hgt} and L_{hgt}, the peak frequency positions G_{pos} and L_{pos} as well as the peaks' FWHM G_{wid} and L_{wid}. In the example shown in Fig. 8 the frequency shift of the Li-metal peak at approximately 246 ppm was allowed to be varied by the fitting algorithm by 5 ppm, whereas peak width and height were free to take any value. For the frequency shift of mossy and dendritic Li signals at 261 ppm and 270 ppm, respectively, a variation of 10 ppm was allowed. In case of narrow confined positions it is assumed that the peak center frequencies are fixed, corresponding to

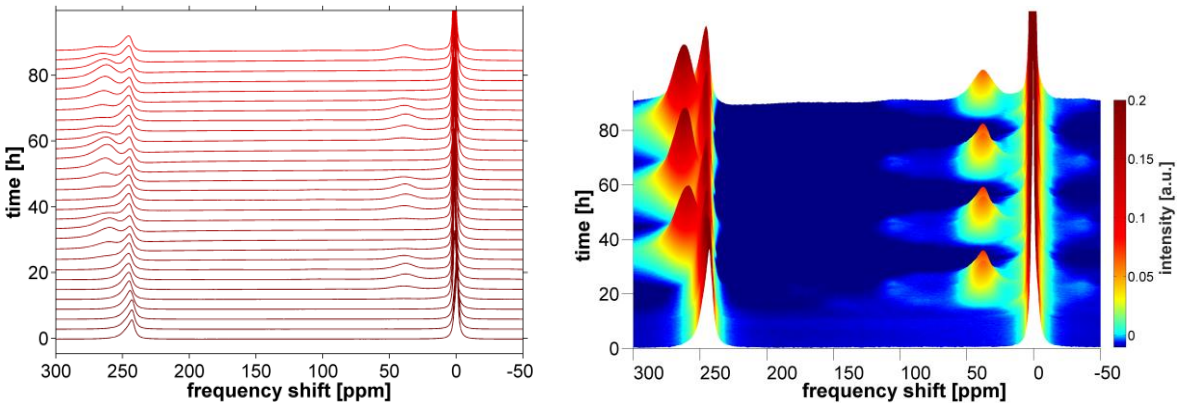

Fig. 7: In-operando NMR spectra in a 2D and a 3D representation. *<u>Left</u>: The NMR excitation can be repeated continuously with a delay of a few seconds between two rf pulses. By averaging the acquired spectra of a Li-metal vs. graphite cell a reduced number of single spectra can be plotted with a y-axis offset on top of each other. <u>Right</u>: For an illustration with a high temporal resolution a 3D plot with color encoded intensity can be used. Both, the right and the left plot show the same NMR measurement of a Li-metal vs graphite cell, which is further discussed in chapter 5.1.*

**Adapted from Kayser et al.*[1,2]

a ‘two-phase model’[89,90]. Instead, a ‘solid-solution model’ could apply, where the position of the peaks continuously changes. Both situations have been observed, for example for Li-metal, between bulk Li and microstructured Li a two-phase situation is observed, while between mossy and dendritic Li, more like a continuous transition is found. The peak position confinement accounts for this.

A similar fitting approach is used to reveal the signal evolutions of other cell compounds, like Li_xC_6, LCO and the electrolyte. The distinction between LiC_{18} and LiC_{12} seems to be of two phase type, while between LiC_{12} and LiC_6 a continuous distribution seems to be prevalent. For Li_xC_6 signals the peak positions are confined within 5 ppm while for LCO signals a center frequency shifting of several hundred ppm is allowed. Even so Li_xC_6 and LCO signals overlap at high SOCs, the difference of the peak widths enables satisfying fits to distinguish between both compounds. The electrolyte signal, which is composed of at least two overlapping peaks within -1 ppm and 2 ppm, is fitted with two peaks and a position confinement within 3 ppm. The integrals of the two peaks are added to show the electrolyte signal evolution. To analyze the complicated electrolyte spectrum in detail, a more extensive fitting with more peaks and an identification of the electrolyte compounds would be nesecarry. Such investigations are outside the scope of this work.

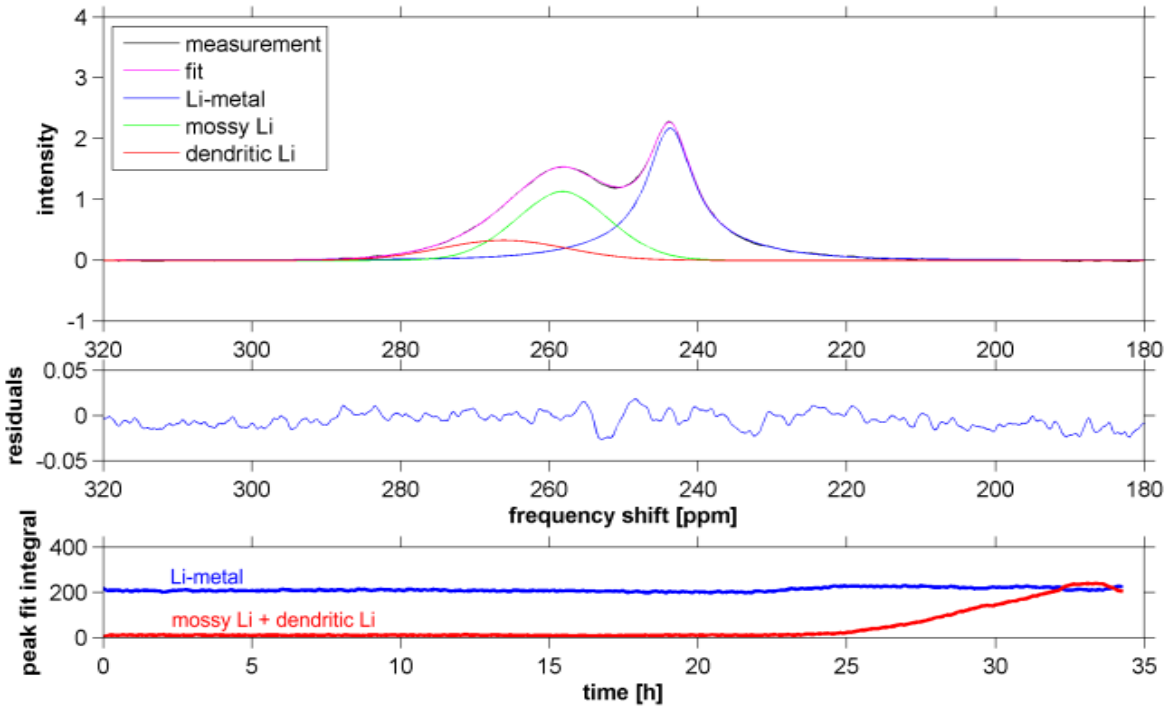

Fig. 8: Peak fitting of overlapping ^{7}Li NMR signals to reveal the intensity integral evolutions of different compounds. *Top panel: Spectrum of a Li-metal vs. graphite cell measured after around 34 h at the beginning of the second discharge. The frequency range, in which Li-metal and Li microstructure signal occur is shown. To distinguish between metallic (blue), mossy (green) and dendritic (red) Li structures, three peaks with mixed Gaussian/Lorentzian line shapes are used for fitting the measured spectrum (black). The center positions of the peaks are confined while the peak widths and heights are free to take any values. The fitted spectrum (magenta) is the sum of the three peaks (blue, green, red). Center panel: The residuals are the differences between the fitted spectrum and the measured spectrum. The random fluctuations of the residuals are due to the noise of the measured spectrum. Their visibility indicates a satisfying agreement of fit and measurement, notwithstanding that for some parts of the spectrum, e.g. between 250 ppm and 255 ppm, the residuals indicate systematic deviations. Bottom panel: Fitting the acquired in-operando spectra one after another and calculating the integrals of the individual peaks gives the evolution of the signal integrals. The contributions of mossy Li and dendritic Li are added to distinguish between Li-metal (blue) and Li microstructure (red). A discussion of the signal evolutions can be found in chapter 5.1.*

Quantifying the evolution of Li in the different Li containing components in the cell is not straightforward. For one, electrically conducting metallic components shield electromagnetic radiation (skin effect). Only if the skin depth is much larger than the thickness of a metallic component, then the corresponding NMR signal is proportional to the number of nuclear spins in the sample. Furthermore, certain parts of a sample may be shielded by other parts, depending on the sample geometry and the direction of the B_1 field. Also, the B_1 field generated by a particular coil may be spatially dependent. Eventually, if Li ions are transported between different environments, such as a metallic electrode and an intercalation compound, the rf impedance of the sample can change. This affects tuning and matching of the NMR resonant circuit and hence its quality factor, leading to a changing signal scaling. While an in-depth discussion is outside the scope of this work, a simple and robust approach for a qualitative discussion is represented by the use of the Li-metal signal integral $I_{\mathrm{LM},0}$ of the pristine cell as reference. Since there is a large surplus of Li in the Li-metal electrode compared to the capacity of the graphite electrode, the thickness d_{LM} of the Li-metal electrode is always larger than the skin depth δ_{LM}. Therefore the variation of $I_{\mathrm{LM}}(t)$ represents a rough estimate for the accuracy of this referencing method. To quantify signal changes, $\mathrm{d}I/\mathrm{d}t$, an arbitrary scaling factor for the slope of $\Delta I_{\mathrm{LM},0} = I_{\mathrm{LM},0} / 1\mathrm{h}$ was chosen, *i.e.* how much a particular signal changes in one hour compared to the amplitude of the metallic Li signal of the pristine cell.

3. Experimental setup

An overview of the *in-operando* NMR setup is given in chapter 3.1. *In-operando* NMR investigations require gas-tight and non-metallic cell housings. The developed lithium-ion and metal-air battery cell containers, described in chapter 3.2, are attached and connected to a customized NMR probe with numerically optimized rf coil (chapter 3.3). Experimental parameters and battery cell materials for measurements of Li-ion and metal-air cells are described in detail in chapter 3.4.
The CAD constructions of the probe frame and resonant circuit parts shown in Fig. 15 were developed in cooperation with Christian Hellenbrandt (FZJ IEK-9).

3.1. Overview of the *in-operando* NMR setup

The NMR probe with battery is placed in a 9.4 T (400 MHz ^{1}H NMR frequency) permanent magnet with 89 mm (3.5 inch) bore (Bruker Ascend 400WB). This experimental setup is schematically illustrated in Fig. 9. The permanent magnet is a superconducting coil in a vessel (blue lines) with liquid helium (approximately 4.2 K). The magnetic field B_0 in the middle of this coil points upwards. The probe (green lines) is inserted from below into an isolated bore at room temperature. For charging, discharging and other testing operations the battery cell under investigation was connected to a potentiostat (Bio-Logic SP-200) with built-in frequency response analyzer for EIS measurements. Red lines indicate the battery cables, which are equipped with low-pass filters. The rf saddle-coil (black line) of the probe for NMR excitation and detection surrounds the battery container and is part of a resonant circuit for the rf pulse generation. The resonant circuit consists of one tunable capacitor, one exchangeable capacitor as well as one tunable coil and is indicated by a black box. It enables the resonance frequency to match the rf pulse frequency to excite the spins. The rf signal connections to a NMR console, which includes the whole spectrometer system like frequency generator, pulse amplifier, quadrature receiver, analog-digital-converter as well as magnet, shim coil and temperature control, are indicated by black lines. Two dashed green lines shall emphasize several more connections of the probe: Three cable for probe identification, temperature sensor and heater control as well as two gas tubes for nitrogen gas tempering and frame cooling. Additional support tubes for electrolyte and cell gas flow in case of experiments on metal-air batteries are not shown.

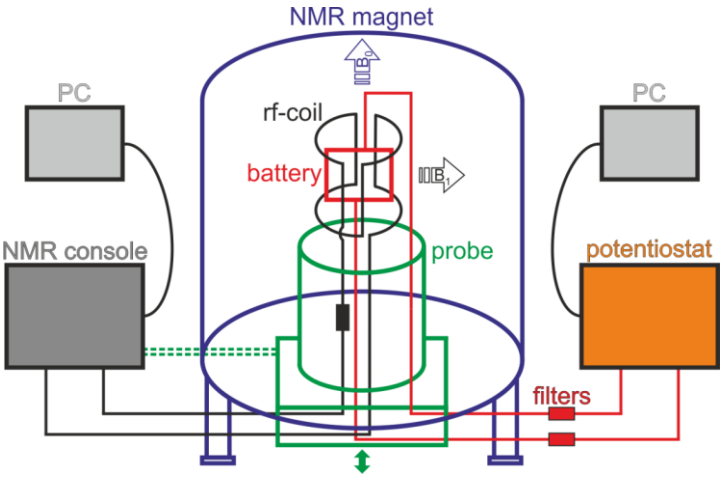

Fig. 9: Schematic drawing of the experimental in-operando NMR setup. *The battery (red) is placed on a customized NMR probe (green) with numerically optimized rf coil (black) and is controlled by a potentiostat (orange). The probe with battery is inserted into a 400 MHz NMR magnet (blue) and connected to a spectrometer system in a NMR console (gray). For graphic user interfaces and data acquisition two computers are used. Dashed green lines indicate several more connections of the probe.*

3.2. *In-operando* NMR battery cell container development

A historical summary of the container design development in given in chapter 3.2.1. The gas-tight Li-ion container for the *in-operando* NMR measurements is described in chapter 3.2.2 and the container for metal-air cells with supply tubes and thin film contacting layers is described in chapter 3.2.3.

3.2.1. History of cell container design

In the first battery container design, which was developed and tested for this work, circular electrodes with a diameter of 7 mm were used. Conceptually, this *in-operando* container (iOC) was a cylindrical body with a drilled hole (see for example v.1.3 in Fig. 10). The battery cell was positioned at the bottom of this hole and closed with a shaft. In the first approach the shaft was turned like a screw into the body to close the container and maintain pressure on the electrodes. Its sealing was done with an O-ring. Wires for the electrode connections were sealed with epoxy. Due to its length of only 30 mm a horizontal orientation of this container in the probe was possible (photograph in Fig. 10).

The lifetime of version 1 cells was very limited. After a few cycles the battery operation stopped. In general, a dry separator and damaged electrodes were found after the disassembly. Hence, it was assumed that insufficient sealing, which can lead to a loss and contamination of electrolyte, and the turning motion during closing of the container, have to be avoided. Therefore version 2.2 exhibited two O-rings, screws for the electrode connections and a spring, which was fixed by two pins (v2.2 in Fig. 10). This design could enable strong breathing of the electrode materials during cycling and turning of the electrodes could be prevented, but sealing would still be problematic. Therefore this design was not put into practice.

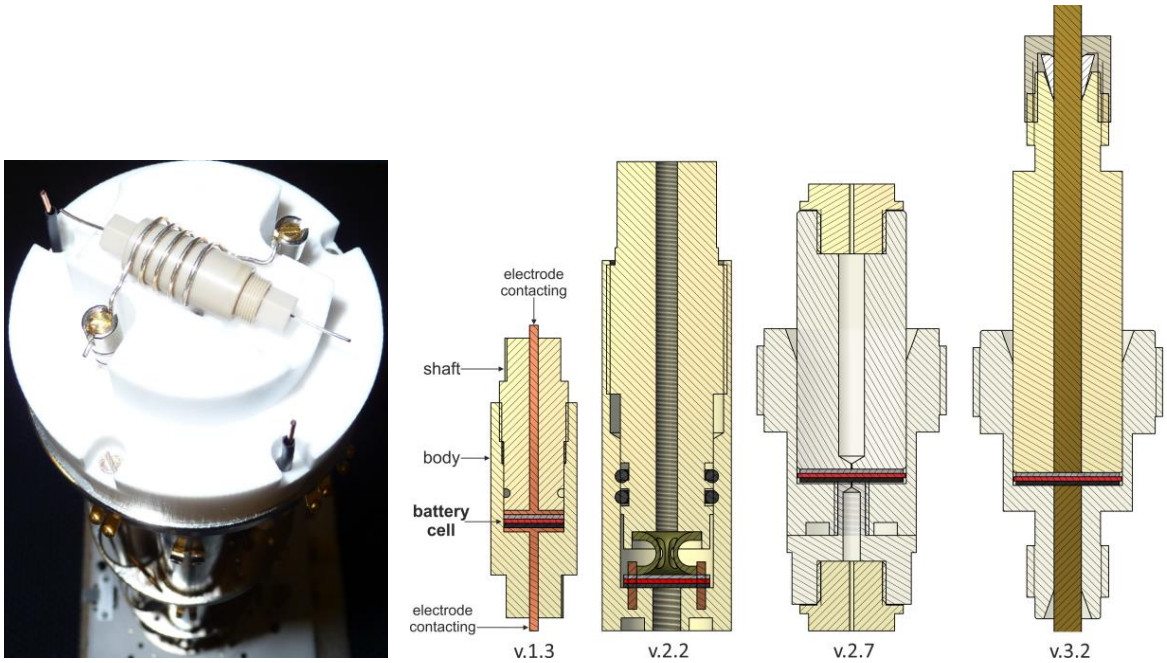

Fig. 10: History of Li-ion in-operando container appearance. *<u>Left</u>: Photograph of an in-operando container version 1.3 with 10 mm outer diameter in an rf solenoid-coil. <u>Right</u>: Four of several considered container designs for in-operando NMR. In the sectional drawings the cell electrodes are shown in gray and black while the separator is highlighted in red. Cycling of version 1 cells was possible for a few hours only. Hence, within the development of a second version (v.2.x) the cell sealing was improved. Using only cutting rings for sealing enabled a long-time gas-tight container design like version 3.2 with an outer diameter of 15 mm. This design was further modified, to simplify and optimize the cell assembly process. The latest iOC version 3.6 for Li-ion batteries is described in detail in chapter 3.2.2.*

Without a spring or other inserts, the screwing to fix the shaft in the body can be avoided by fixing the shaft with a cutting ring (for details see chapter 3.2.2). This sealing principle was used in version 2.7 only for the shaft-body sealing. The electrodes were connected by 100 µm wires, which were embedded into a plastic screw and the shaft. In a new container (version 3) cutting rings were used to seal both shaft and electrode connections (cutting ring is shown only at the top of v.3.2 in white). Instead of wires, contacting sticks were used. To simplify and optimize the cell assembly process the third design was improved until version 3.6. Its details are described in chapter 3.2.2. The 15 mm outer diameter of this container enables 12.5 mm circular electrodes and a reasonable compromise between magnetic field strength and homogeneity of the NMR rf coil, as described in chapter 3.3.2.

To minimize disturbances and shielding of the magnetic field, plastic sticks with thin-film conductive coating for the electrode connection were developed. The principle is shown in Fig. 11. Applying metal-deposition techniques for the fabrication of contact pattern and conductive paths is well established in the field of semiconductor devices[91]. By using sputter deposition for the fabrication of electrode connections inside a NMR cell container, the thickness of current collectors and thereby rf absorption can be reduced. The skin depth (penetration length) l of an rf field into metal can be approximated by:

$$l = \sqrt{\frac{\rho}{\pi \mu f}}$$

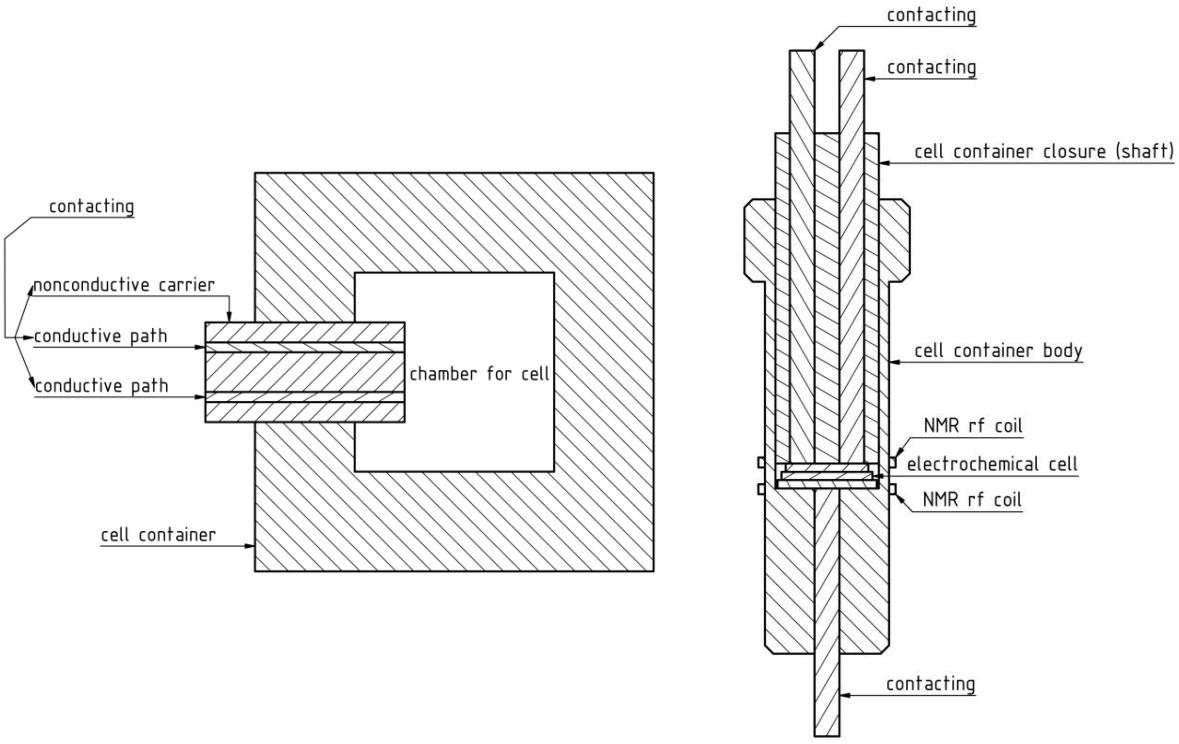

Fig. 11: Schematic drawings of electrode contacting with thin-film conductive layers attached on plastic carriers. *Adapted and translated from DPMA patent no. 102016005170 (ref.* [3]*). Left: Schematic drawing of the thin-film contacting principle in a simple rectangular cell container. For the connection of a cell in the container, a few hundred nanometer thin conductive paths are attached on nonconductive plastic carriers by e.g. sputter deposition. Thereby disturbances in NMR measurements due to susceptibility and shielding effects can be reduced. Right: Sectional drawing of a cell with three contacting sticks for the connection of an electrochemical cell. On each plastic stick several conductive paths can be attached. The patent describes the procedure and manufacturing method of thin-film contacting of an electrochemical system.*

Using for copper the resistivity $\rho \approx 0.01721\ \Omega\ \mathrm{mm^2\ m^{-1}}$, the permeability $\mu = \mu_0\mu_r \approx 1.257 \cdot 10^{-6}\ \mathrm{V\ s\ A^{-1}\ m^{-1}}$ and the ^{7}Li NMR frequency $f = 155.51737\ \mathrm{MHz}$ gives a skin depth $l \approx 5.29\ \mu\mathrm{m}$. For gold with $\rho \approx 0.02214\ \Omega\ \mathrm{mm^2\ m^{-1}}$ and $\mu \approx 1.256 \cdot 10^{-6}\ \mathrm{V\ s\ A^{-1}\ m^{-1}}$ this approximation gives $l \approx 6.007\ \mu\mathrm{m}$.

For the presented experiments, gold and copper contacting layers were applied by cold-plasma sputtering (Bal-Tec SCD 050). A layer thickness of 500 nm is sufficient for low direct current (DC) resistance and adequate layer stability. Sheet resistance measurements as well as laser scanning microscopy (LSM) and scanning electron microscope (SEM) pictures are shown in chapter 4.1. Gold sputter coatings can be made under low vacuum conditions (10^{-2} mbar), but are destroyed by metallic Li after a few days[92]. For copper sputtering high vacuum ($<10^{-5}$ mbar) is favorable. An alternative is copper electroplating, which was successfully tested as well. These ways of connecting an electrochemical cell and the procedure of manufacturing these current collectors were patent-registered[3]. In a container design for metal-air batteries, such thin-film conductive layers enabled the connection of the air cathode from the backside (chapter 3.2.3). Moreover, this contacting method was used for the development of an *in-operando* NMR electrolysis cell (appendix 12.1) and can enable the integration of the NMR rf coil into the cell container.

3.2.2. Gas-tight Li-ion cell container*

The latest *in-operando* container (iOC version 3.6) is shown in Fig. 12. In total it is 93 mm long and has an outer diameter of 15 mm at the position of the electrochemical cell components. The battery cell is positioned at the bottom of a 12.5 mm inner diameter bore and closed with a shaft. The shaft is pushed into the body and then fixed by a screw nut, which presses a cutting ring. The cutting ring (inset in Fig. 12), which is a kind of surface seal O-ring, has a triangular cross section and seals the container reliably. For applications with overpressure the sealing was tested up to 15 bar with N_2 gas. The pressure loss was below 1 bar within one day starting at 15 bar. For overpressure up to 3 bar the loss was below 0.2 bar within one week. The force for compressing cell components can be applied reproducibly without any turning motion between body and shaft. Thereby reproducibility of the container assembly is simplified. The spacing between the electrodes can be adjusted with a tolerance below 0.1 mm. In appendix 12.3 a modified container design, which enables a predefined immovable spacing between the electrodes, is presented.

For electrical contacting of the cell, contacting sticks are pushed through holes in the body and the shaft. A diameter reduction of these sticks supports a correct alignment at end stops inside body and shaft. They cannot be pressed deeper than 0.1 mm into the cell chamber to protect the cell components as well as for a reliable electrical contact. The contacting sticks are sealed by cutting rings as well. By completely avoiding epoxy or glue, a contamination or absorption of the electrolyte is prevented. Moreover the container can be opened and reassembled many times. For example one of the first containers of version 3.6 has been reassembled more than 20 times and is currently still in operation.

Contacting sticks can be easily substituted, as they are not permanently incorporated into the cell housing. For long-run experiments on LIBs with metallic Li electrodes, solid copper contacting sticks were used that did not show a contact loss due to slow chemical reactions of the copper with Li-metal

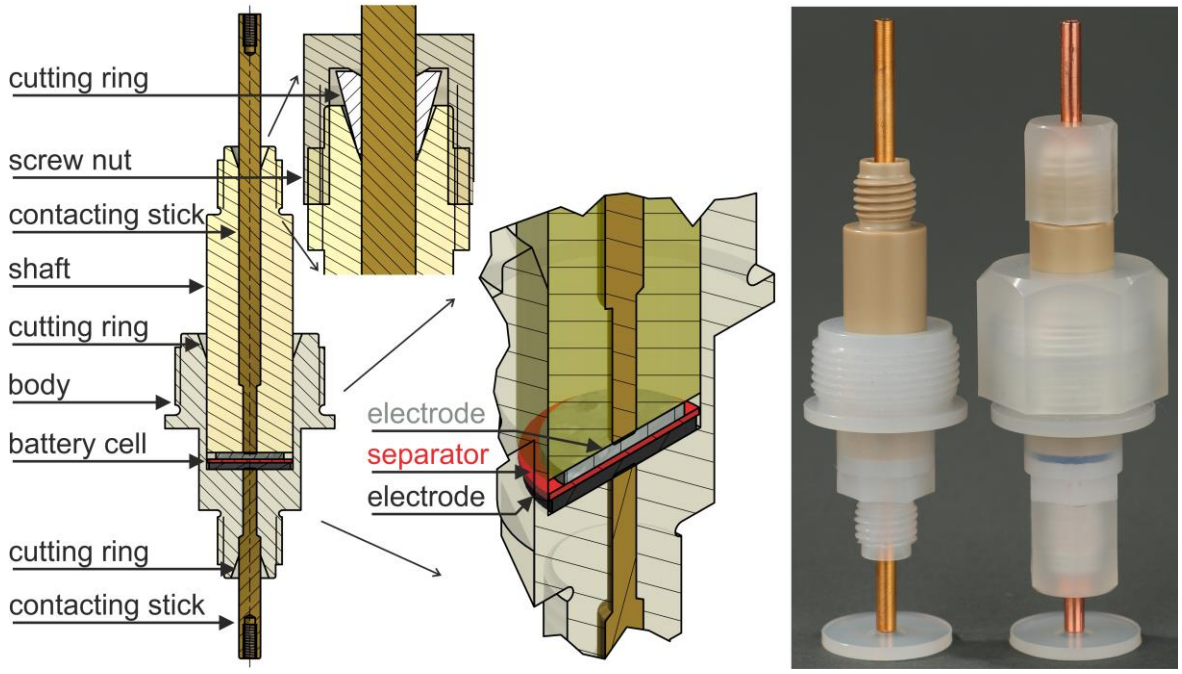

Fig. 12: Design of in-operando NMR container. *Left: Sectional drawing of cell container version 3.6. Electrodes are placed in a cylindrical body, which is closed with a shaft and sealed by a cutting ring. To connect the electrodes, plastic contacting sticks with conductive coating are pushed through holes in body and shaft. The sticks are sealed by cutting rings as well. For better visibility an upper electrode (grey) with a reduced diameter was used. Right: Photograph of cell container version 3.6 with and without screw nuts and cutting rings.*

**Adapted from Kayser et al.*[1,2]

to form Li-Cu alloys[92]. In addition to full-metallic sticks, plastic sticks with thin conductive coatings have been used[3]. Thereby less metal is loaded into the sensitive region of the rf coil, leading to a reduction of damping, distortions and shielding of the rf magnetic field, B_1.

The container was produced of PFA (Perfluoralkoxy, operation temp. up to 260 °C) and PEEK (Polyetheretherketone, operation temp. up to 280 °C). PFA is transparent, thus assembled components inside the body can be visually inspected (Fig. 12b). PEEK has a higher durability under mechanical stress[93–95] and is the material of choice for the contacting sticks. Most importantly, both materials have a high chemical resistance[96] not only against nearly all kinds of chemical substances commonly contained in battery electrolytes, but also against bases and acids as well as metallic lithium. The chemical resistance was tested by storing and weighting PFA, PEEK and PCTFE (Polychlorotrifluoroethylene, operation temp. up to 175 °C) disks in LP30 electrolyte for two years. PEEK lost its brownish color and became white, PFA and PCTFE were stable. By pressing Li-metal on PTFE and PCTFE, both became black. PFA and PEEK showed no changes after cleaning. Thus PFA for the body, shaft and cutting rings and PEEK for the contact sticks were used. For better visibility a PEEK shaft and PCTFE screw nuts were used for the photographs shown in Fig. 12.

3.2.3. Metal-air cell container with gas and electrolyte supply

For *in-operando* NMR measurements on metal-air batteries, the *in-operando* container is equipped with four additional gas and liquid electrolyte supply lines (Fig. 13). Therefore 1 mm channels are integrated into the container shaft, whereas the body of the Li-ion iOC version 3.6 is used. At the bottom of the body the metal electrode is placed (red in Fig. 13). In this work a silicon wafer was used. It is pressed by a separator ring (blue), which has two holes for electrolyte flow through the cell chamber. This ring also presses the air cathode (green) against the shaft and thereby seals the electrolyte off from the gas on top. It defines a spacing of 4 mm between the electrodes. In case of a leakage, the air cathode can be rinsed by a gas flow, which can blow away leaked electrolyte. Due to the separator ring with an inner diameter of 7 mm, the active surface area of air cathode and metal anode is approximately 0.385 cm^2.
At the top of the metal-air shaft, four PEEK capillary tubes are connected (0.75 mm inner diameter, see photograph in Fig. 13). One tubing connects the electrolyte inlet to a peristaltic pump (Ismatec Reglo Analog MS-2/12, flow rate 0.003 – 38 ml/min), which pumps the electrolyte from a reservoir. The flow rate at a given speed setting of the pump depends on the viscosity of the electrolyte. A second tubing is used for the electrolyte outlet and ends at the reservoir. Thus, the electrolyte flows in a loop and the flow speed can be adjusted at the pump. Using a silicon anode and an aqueous KOH electrolyte the corrosion reaction, described in chapter 2.1.2, leads to an evolution of hydrogen gas inside the cell chamber. To avoid overpressure and insulating gas accumulations at the electrodes, especially at the upper air cathode, the electrolyte flow can be adjusted such that gas bubbles are pushed towards the electrolyte outlet. Because the PFA shaft is transparent the bubbles rising through the outlet channel of the shaft can be observed by eye. To separate gas and electrolyte the electrolyte reservoir has a hole such that gas is released at its cover while fresh electrolyte is taken from the reservoir bottom.

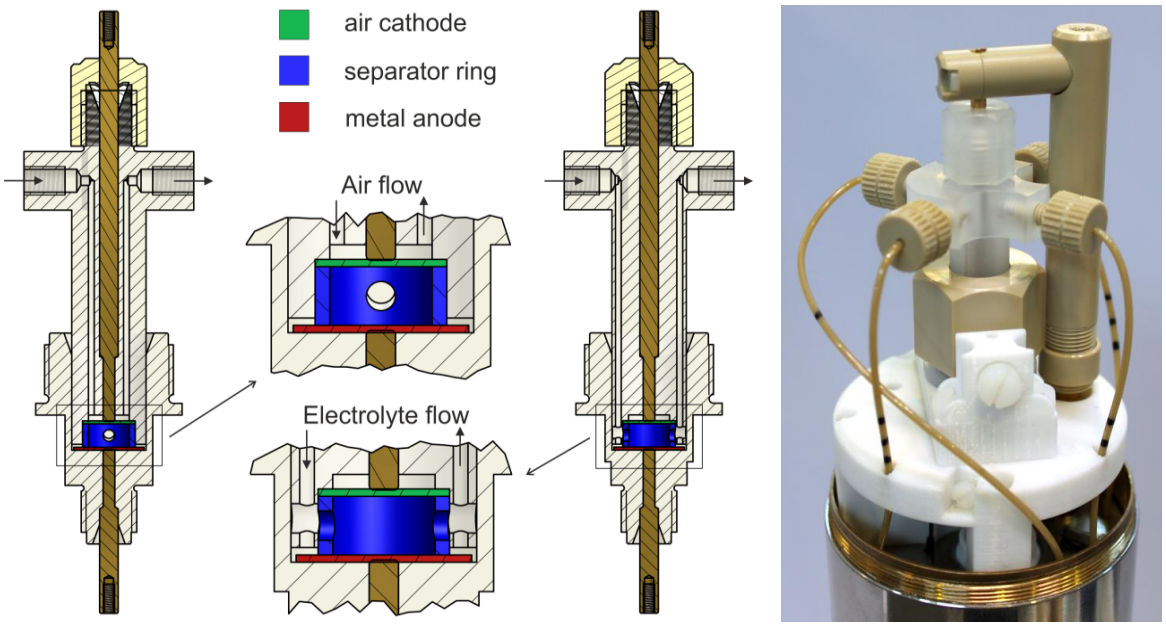

Fig. 13: In-operando NMR container with gas and electrolyte supply for metal-air battery cells. *Left: Sectional drawings of the metal-air container version 1.2. The electrodes (green and red) are separated by a PFA ring (blue). Two support channels in the shaft are used for a gas flow on top of the air cathode and the other two channels are used for an electrolyte flow through the cell chamber. Right: Photograph of the metal-air iOC mounted on the NMR probe. The probe was equipped with four capillary tubes for the electrolyte and gas support. A vertical cell orientation is necessary with respect to the bore diameter of the superconducting NMR magnet.*

The third tubing connects a synthetic air gas bottle with the cell's gas inlet and the fourth tubing is used for the gas outlet. The gas flow can be adjusted at a pressure valve and the outlet ends in a tank to neutralize electrolyte ingredients in case of a leakage. To enable an optimal triple phase boundary inside the air cathode and in the same manner to control electrolyte and gas permeations, the gas and the electrolyte pressures can be balanced. For extensive testing, like air cathode flooding or drying, the pressures can be increased asymmetrically.

Most air cathodes are equipped with a gas permeable PTFE foil at the air side to prevent electrolyte leakage. These foils are electrically insulating, hence a direct contacting of the air cathode with a contacting stick from above, as for electrode materials on conductive foils, is not possible. A solution based on the thin-film contacting approach[3] (presented in chapter 3.2) is illustrated in Fig. 14. Gold layers (orange lines, 1 µm thickness) are attached on parts of the shaft and the separator ring such that the air cathode is contacted from below. To define the gold layer shapes, Kapton tape (poly-oxydiphenylene-pyromellitimide) is used. For mechanical stability and high conductivity the porous air cathode material is supported by a stainless steel mesh. This mesh is pressed against a gold layer on the upper part of the separator ring, which is in contact with a gold layer on the shaft. In this way the inside of the air cathode is connected to a contacting stick without the need of a direct contact between stick and cathode.

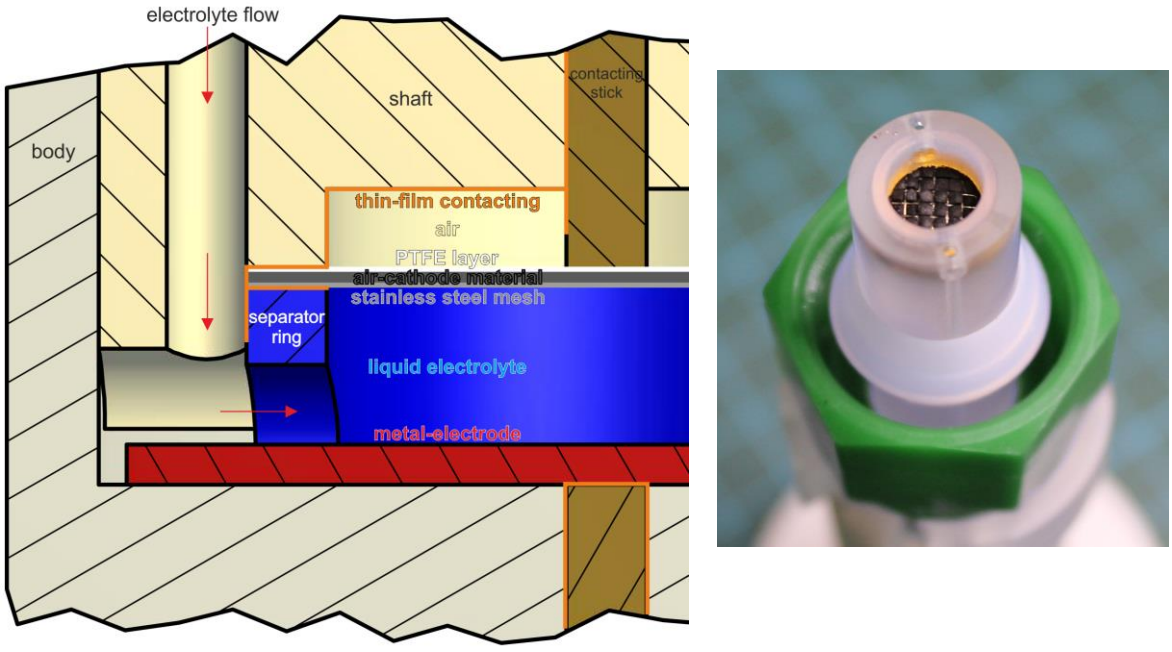

Fig. 14: Thin-film contacting layers for the connection of the air cathode on the inside of the cell chamber. *Left: Sectional drawing of a metal-air iOC with highlighted thin-film contacting layers (orange lines). A PTFE foil (white) on the air cathode mitigates a leakage of electrolyte into the air chamber but prohibits a direct connection to a contacting stick. Using the thin-film contacting approach[3], it is possible to contact the air cathode from below at its integrated stainless steel mesh. Right: Photograph of a metal-air iOC shaft with 1 µm gold layers, air cathode, separator ring, cutting ring sealing and screw nut. The shaft is placed upside down. The stainless steel mesh of the air cathode at the inside of the cell chamber is in contact with the gold layer on one side of the separator ring. The gold layer on the shaft is in contact with the separator ring gold layer and the contacting stick gold layer.*

3.3. *In-operando* NMR probes*

The *in-operando* cell container is placed in a Bruker high-power broad-band high-temperature (HPBBHT) probe (photographs in Fig. 16). The top of the probe was modified by attaching 3D-printed parts for the container mounting (chapter 3.3.1) and the rf saddle coil (chapter 3.3.2). The middle of this coil is placed in the sweet-spot of a 400 MHz Bruker wide-bore NMR magnet. By shimming the B_0 field of the magnet with an *in-operando* cell container on the probe a minimum ^{7}Li FWHM of approximately 5 Hz (≈ 0.03 ppm) was reached. This was achieved both for contacting sticks completely made of copper and for plastic sticks with thin-film contacting layers. For this experiment and for spin nutation curves (chapter 4.2) three glass fiber separators on top of each other, with a total height of 1 mm in the 12.5 mm inner diameter cell chamber, were filled with 100 µl of 1 M LiCl in water. Using higher container mounting parts, the same probe was also tested in a 600 MHz Bruker wide-bore magnet.

The cell temperature can be controlled by placing a 3D-printed hood on top of the container mount and using a tempered nitrogen gas flow. Because polycarbonate 3D-printing was employed, the upper temperature limit is 120°C. The lower temperature limit depends on the cooling power of the gas flow and –30°C can be easily reached. In general, the probe temperature was stabilized with 800 l/h nitrogen gas flow at 25 °C. Varied conditions are specified in the descriptions of the different NMR experiments.

A broad-band frequency range of the HPBBHT probe of 55 MHz – 225 MHz becomes possible by a set of exchangeable resonant circuit capacitors. At the resonance frequency the impedance of the circuit is much smaller than for off-resonant frequencies. This leads to a voltage enhancement of the applied rf signal for NMR excitation. In Fig. 15 an *in-operando* NMR probe is shown, which was constructed

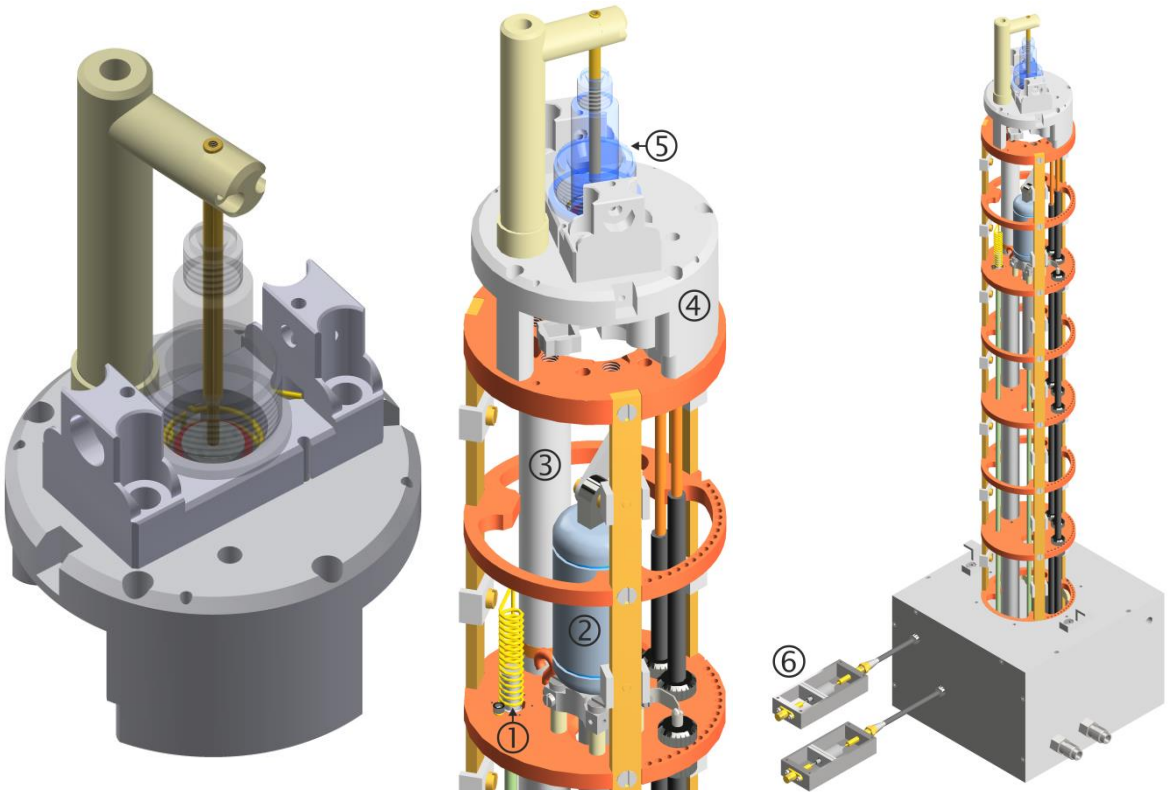

Fig. 15: CAD drawing of an in-house developed in-operando NMR probe. *Left: Mount for saddle coil and cell container, constructed for 3D-printing. Center: Upper part of NMR probe with ① tunable coil, ② tunable capacitor, ③ exchangeable capacitor, ④ mount and ⑤ iOC. Right: Complete NMR probe with low-pass frequency filters (label ⑥) connected to the battery lines. The CAD constructions of the probe frame and resonant circuit parts were developed in cooperation with Christian Hellenbrandt.*

**Adapted from Kayser et al.*[1,2]

during this work and equipped with the same resonant circuit as the HPBBHT probe. The exchangeable capacitor is labeled with ③. To fine tune the resonant circuit frequency center and width, a tunable capacitor (label ②) and a tunable coil (label ①) are used.
For the rf pulse generation the probe is connected to a 1000 W pulse amplifier. The maximum pulse length is limited by arcing at the rf coil. For a pulse power of 500 W a maximum pulse length of approximately 300 µs is possible. Using 200 W power, pulse length of 1 ms and longer are possible. In case of arcing, the control electronics stop the pulsing and thereby prevent a damage.

3.3.1. Cell container mounting and connections*

For mounting of the cell container and the rf coil two 3D-printed polycarbonate parts (Stratasys 3D-printer Fortus 400mc) are used. One part (label ⑥ in Fig. 16c), called throne, fixes the container with two screws and covers the saddle coil. Thereby the throne sets the vertical cell positioning inside the coil. The second part (label ⑤ in Fig. 16c) is called mount and fixed on the top plate of the NMR probe. It exhibits channels for the rf signal connections (label ②), the connection of the upper cell contacting stick (label ③ and ⑦), the tempered gas (label ⑧ in Fig. 16d), the temperature sensor and for the gas/electrolyte support capillary tubes.

The electrical connections to the container contacting sticks consist of 50 µm copper wire (GVL Cryoengineering). Thereby metallic parts close to the rf coil and distortions of the B_0 field homogeneity are minimized. To avoid vibrations, the wire for the upper connection is embedded in a stable PEEK gallows (label ⑦ in Fig. 16c) with a SMB/SMA adapter plug at the bottom (label ③). A small 3D-printed cable guide with attached SMB board connector is used for the 50 µm wire, which is pushed against the lower contacting stick (label ④ in Fig. 16c and label ③ in Fig. 17a,b). To ensure low contact resistances the 50 µm wires are embedded into a small amount of silver epoxy (EPO-TEK EJ2189 LV) at the end of the two cable guides, which are pushed against the contacting sticks (inset in Fig. 16). The

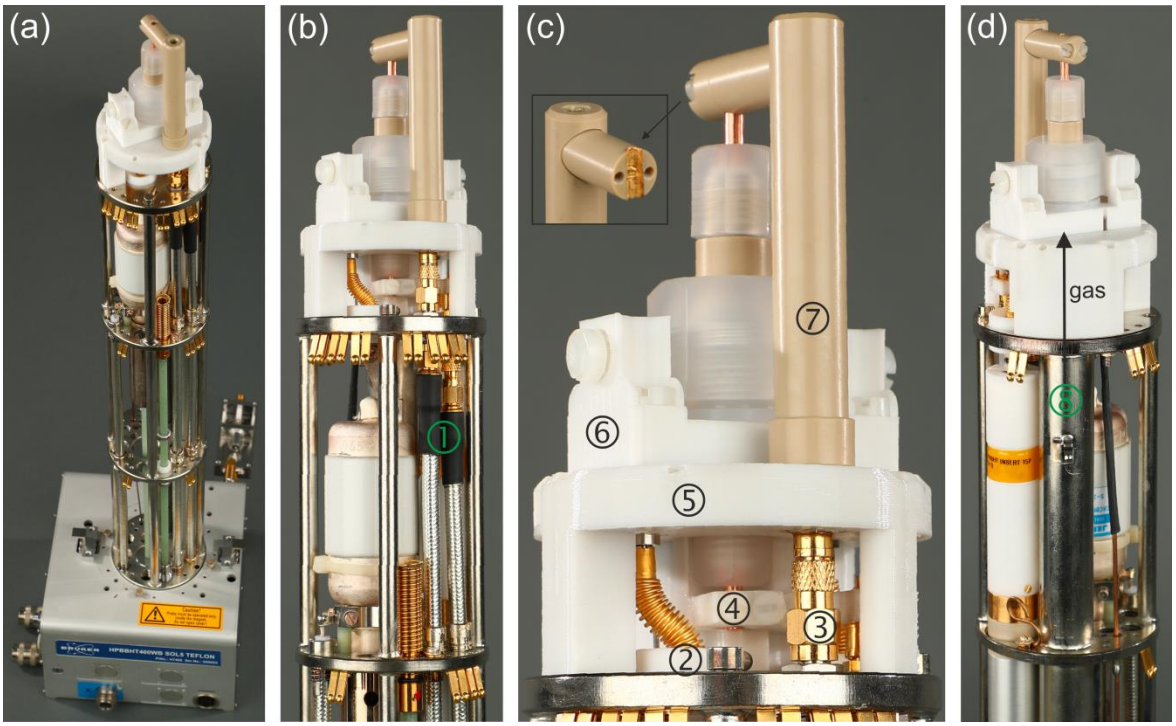

Fig. 16: Modified HPBBHT in-operando NMR probe with connected battery cell container. *(a) In total the probe with mounted container has a height of 63 cm. For the photographs the frame cover and the container hood were removed. (b) The semi-rigid battery lines inside the probe frame are labeled with ①. The resonant circuit components are the same as described for the in-house developed probe (Fig. 15). (c) One of the two rf signal connections of the saddle coil is labeled with ②. The adapter labeled with ③ connects a semi-rigid cable with the PEEK gallows (label ⑦) for the upper cell contacting stick. For contacting the lower stick a 3D-printed cable guide (label ④) is fixed with two screws at the mount (label ⑤). On top the container is placed on a throne (label ⑥). The inset shows the contact surface, which is pushed against the upper contacting stick. The gold layer covers a 50 µm wire embedded in silver epoxy. (d) In a glass tube inside a stainless steel tube of the probe frame (label ⑧) the tempered nitrogen gas is guided to a channel in the mount. Using a 3D-printed hood on top of the mount the cell temperature can be stabilized, even at -30°C.*

*****Adapted from Kayser et al.*[1,2]*

silver epoxy is protected by a 1 µm gold layer attached by sputter deposition. For the battery lines inside the probe frame, the inner conductors of two semi-rigid cables are used (label ① in Fig. 16b).
At the bottom plate of the probe these semi-rigid cables are connected to low pass frequency filters (API Technologies Spectrum Control 51-311-316) in two shielded boxes (label ⑥ in Fig. 15). Thereby a transmission of signals in the MHz frequency range via the battery cables towards the battery control device is reduced (filter specification: 70 dB @ 1 MHz to 1 GHz). Without low pass filters the rf pulses induce changes in the voltage measured by the potentiostat with peak heights up to 0.1 V. A CAD drawing and the measured attenuation curve of one of the self-made filter boxes are shown in the appendix 12.4. Because signals below 150 kHz are not strongly attenuated (<20 dB), electrochemical impedance spectroscopy (EIS) inside the NMR magnet can be performed as well. Battery testing and EIS experiments are performed using a Biologic SP-200 potentiostat/galvanostat.

3.3.2. B_1 magnetic field rf coil*

The cylindrical cell container is placed vertically inside the NMR magnet, thus oriented with its axis parallel to the B_0 field, and with the cell electrode plates horizontal, parallel to the B_1 field (Fig. 17a). A saddle coil design is used for rf excitation, which was optimized numerically regarding its impedance, B_1 field strength and B_1 homogeneity. The simulations are based on a wire model of the coil design and performed using NEC4 ("Numerical Electromagnetics Code", Lawrence Livermore National Laboratory, Livermore, CA). The NEC software uses the method of moments, thus calculates the electromagnetic field for a setup that consists of a network of wire segments. As demonstrated by Dietrich and Sebak[38] the software was controlled by a self-developed Matlab interface to adjust rf coil parameters and to plot the 3D simulation results (chapter 4.2). By specifying the wire material and wire radius, these simulations estimate the coil impedance. With this impedance value, we ensure that the coil can be tuned and matched in the resonance circuit of the probe. The 15 mm inner diameter of the modeled saddle coil is given by the cell container diameter. A height of 4 mm is chosen with respect to the size of battery cells. The wire diameter is 0.75 mm and its conductivity is set to that of copper. To account for disturbances from the contacting sticks of the in-operando NMR container, these cell connections are included in the model by adding passive vertical wires with a diameter of 2 mm along the center of the coil. These wires have a gap of 1.0 mm in the center of the coil where the electrodes are placed. The electrode plates itself are not included in the model.

With these simulations, the coil inductance and hence the impedance of the rf circuit could be adjusted close enough to a target value that tuning and matching could be performed using a set of variable capacitors built into the probe. For winding a 0.75 mm silver-coated copper wire to the numerically calculated saddle coil shape, a 3D-printed cylinder template was used.

To verify the accuracy of the simulation results, the spin nutation curve is estimated by using the simulated B_1 field and a B_0 field homogeneity of $\Delta B_0 = 6 \times 10^{-7}$ T. This value of ΔB_0 is chosen with respect to a measured ^{7}Li full width at half maximum (FWHM) of around 5 Hz at 9.39 T for 1 M LiCl

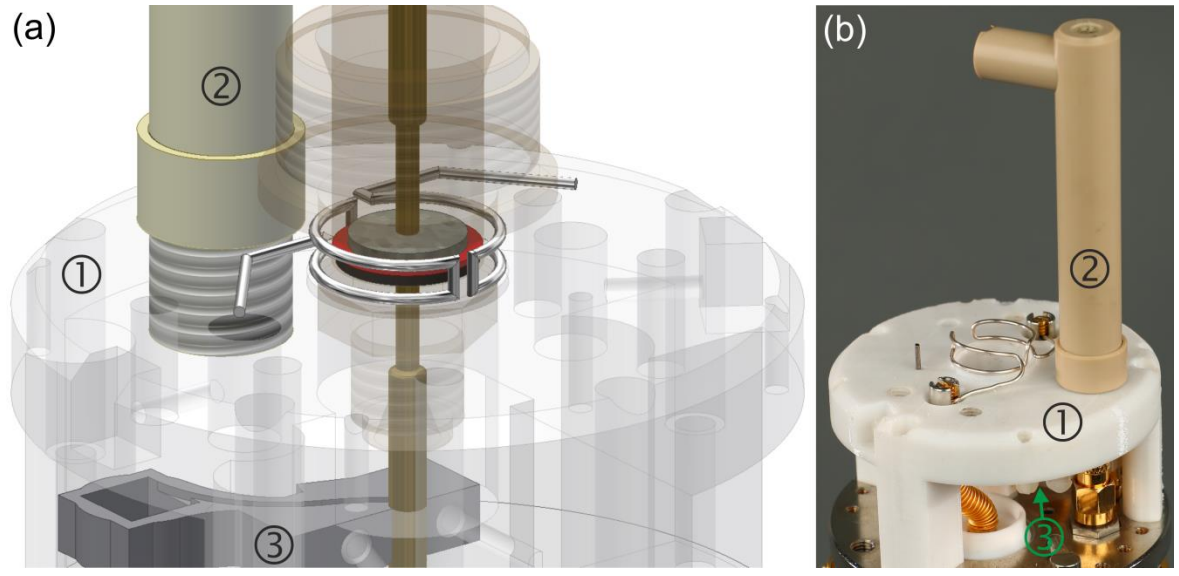

Fig. 17: Numerically optimized rf saddle coil. *(a) CAD drawing of the 3D-printed mount (label ①) and the saddle coil around the cell container with electrodes and contacting sticks. For the connection of the cell a stable PEEK gallows (label ②) and a 3D-printed cable guide (label ③) are used. (b) Photograph of the top of the probe with disassembled container throne. The coil geometry was optimized by numerical B_1 field simulations.*

*****Adapted from Kayser et al.*[1,2]

solution, soaked into three layers of glass fiber separator (1 mm height) inside the cell chamber of the *in-operando* container. The calculated results are compared to measured nutation curves from the described setup. To investigate the effects of cell connections, simulations are compared with measurements performed with solid copper contacting sticks, pure PEEK sticks and PEEK sticks with a 500 nm gold coating. Gold was used instead of copper to ensure a high surface conductance in an aqueous solution of LiCl.

3.4. Battery cell materials and experimental parameters*

Experiments on eleven different Li-ion cells are presented in this work. Their materials, differences in the cell assembly and performed measurements are summarized in chapter 3.4.1. In the same manner materials and experimental parameters of NMR measurements of the Si corrosion and two Si-air cells are given in chapter 3.4.2. The cycling parameters are described for each cell in chapter and also in detail in the result section together with the current/voltage profiles.

3.4.1. Li-ion cells

Li-ion electrode materials (LCO and graphite) were purchased from Custom Cells Itzehoe GmbH. Sheets with 100 µm LCO on 20 µm Al foil exhibiting 3.5 mAh/cm^2 area capacity (155 mAh/g specific capacity) and 112 µm graphite on 18 µm copper foil exhibiting 3.8 mAh/cm^2 (350 mAh/g) were stamped to get 12 mm circular electrodes. Battery grade metallic Li with a thickness of 250 µm was purchased from Rockwood Lithium GmbH (now Albemarle). In all experiments on Li-ion cells Whatman GF/D glass microfiber separators (approx. 0.1 mm to 0.3 mm thickness after compression), a 12 mm diameter of electrodes and separators and LP30 electrolyte (1 M $LiPF_6$ in 1:1 ethylene carbonate:dimethyl carbonate) from BASF were used.

For *in-operando* ^{7}Li NMR measurements of Li-ion cells a pulse power of 500 W and a pulse length of 6 µs were used. The pulse delay and the number of averaged FIDs, which determine the temporal resolution of a 3D-spectrum, are given in the figure captions. With respect to the B_0 field strength of 9.39 T a ^{7}Li NMR frequency of 155.51737 MHz was used.

The LCO vs. Li-metal **cell 1** for the current rate capability comparisons (chapter 4.3) was assembled in an *in-operando* container with a LCO electrode, a Li-metal electrode, one separator and thin-film copper contacting sticks. As a benchmark, the LCO vs. Li-metal **cell 2** was assembled in a standard housing[57] (Swagelok PFA container) with a LCO electrode, a Li-metal electrode, one separator, stainless steel current collectors, a spring and a 12 mm nickel disk on top of the Li-metal.

LCO vs. graphite **cell 3** and **cell 4** for long-time cycling experiments (chapter 4.4) were assembled each in an *in-operando* NMR container with thin-film copper contacting sticks, a LCO electrode, a graphite electrode and one separator. For comparison LCO vs. graphite **cell 5** was assembled like cell 3 and 4, but with two separators.

When assembling the Li-metal vs. graphite **cell 6** for long-run *in-operando* NMR measurements (chapter 4.4 and 5.2) in an *in-operando* container with solid copper contacting sticks, a Li-metal electrode, a graphite electrode and three separators were compressed until a cell thickness of 0.5 mm was obtained. The charge/discharge profiles of cell 3, 4, 5 and 6 are given in chapter 4.4

Li-metal vs. graphite **cell 7** for *in-operando* NMR and *in-situ* EIS experiments was assembled like cell 6, but the electrodes and the separators were compressed less strongly until a cell thickness of 0.3 mm was obtained. For *in-situ* EIS measurements (chapter 4.5), performed after *in-operando* NMR measurements (chapter 5.1), the impedance was measured with a potentiostat with built-in frequency response analyzer (Bio-Logic SP-200). Measurements were conducted from $f = 2 \cdot 10^5$ Hz to $f = 1 \cdot 10^{-1}$ Hz with an excitation amplitude of $U = 1 \cdot 10^{-2}$ V and 15 points per decade. The temperature was kept constant at 30 °C in a climate chamber (Binder KB115).

LCO vs. Li-metal **cell 8** for *in-operando* NMR measurements (chapter 6.1) was assembled with solid copper contacting sticks, a LCO electrode, a Li-metal electrode and three separators, which were compressed until a cell thickness of 0.5 mm was obtained.

**Adapted from Kayser et al.*[1,2]

LCO vs. graphite **cell 9** for *in-operando* NMR measurements (chapter 6.2) was assembled with thin-film copper contacting sticks, a LCO electrode, a graphite electrode, three separators and a cell thickness of 0.5 mm. LCO vs. graphite **cell 10** and **cell 11** were assembled like cell 9, but compressed until a cell thickness of 0.4 mm was obtained.

3.4.2. Si-air cells

For Si-air battery anodes, n-type single crystalline Si wafers with a thickness of 0.6 mm, <100> orientation and arsenic doping (0.001 – 0.007 Ω cm) were purchased from University Wafer. The exact dopant concentration was not specified and should be approximately 10^{19} cm^{-3} to enable a sufficient conductivity of semi-conducting Si. The wafers were cut into disks with 10 mm diameter and cleaned with oxygen plasma followed by sulfur hexafluoride plasma (Diener PICO) for removing oxides prior to the experiments. The porous carbon-based air electrode was purchased from Electric Fuel Ltd. The E4 type without MnO_2 catalysts was used to avoid disturbances of the NMR measurement by paramagnetic manganese. The alkaline electrolytes were prepared by dissolving different amounts of KOH (1 – 8 M, Fluka, ≥85 % KOH basis) in deionized water (conductivity < 10 µS cm^{-2}).

For ^{29}Si NMR measurements at 9.39 T B_0 field strength a ^{29}Si NMR center frequency of 79.500535 MHz was used. NMR measurements of different KOH solution end states with dissolved Si-wafers (chapter 7.1) were performed with 150 W pulse power, 19 µs pulse length and a scan delay of 20 s. The solutions were filled in 15 mm PFA tubes and placed in the *in-operando* HPBBHT probe stabilized to 25 °C.

For time-resolved ^{29}Si NMR measurements of the Si corrosion (chapter 7.2) the Si wafers were dissolved in 12 mm PFA tubes with approximately 4 M KOH aqueous solution inside the NMR for *in-situ* observations. After full dissolution of the wafers the electrolyte solutions contained approximately 3 M Si. These experiments were performed at an early stage of this work at which a probe frame tempering was not yet available. A pulse power of 75 W, a pulse length of 29 µs and a saddle coil with 12 mm diameter were used. The temperatures of the tubes in the HPBBHT probe were stabilized with a nitrogen gas flow of 600 l/h. All solutions were prepared by Dr. Yasin Emre Durmus (FZJ IEK-9).

The solution for the time-resolved ^{29}Si NMR measurement at 60 °C without corrosion inhibitor contained ~4.24 mol/l KOH and ~3.16 mol/l Si assuming 100 % KOH basis. Calculating the KOH concentration with the assumption of 85 % KOH basis gives a solution with ~3.61 mol/l KOH.

For the measurement at 40 °C the solution contained ~4.31 mol/l KOH and ~2.82 mol/l Si assuming 100 % KOH basis. Calculating the KOH concentration with the assumption of 85 % KOH basis gives a solution with ~3.67 mol/l KOH.

The solution for the measurement at 20 °C contained ~4.20 mol/l KOH and ~3.19 mol/l Si assuming 100 % KOH basis. Calculating the KOH concentration with the assumption of 85 % KOH basis gives a solution with ~3.57 mol/l KOH.

The solution for the 60 °C experiment with around 5000 ppm PEG di-acid (Sigma Aldrich) inhibitor contained ~4.23 mol/l KOH and ~3.18 mol/l Si assuming 100 % KOH basis. Calculating the KOH concentration with the assumption of 85 % KOH basis gives a solution with ~3.60 mol/l KOH.

Si-air **cell 12** and **cell 13** for ^{29}Si *in-operando* NMR measurements (chapter 7.3) were assembled each with a 10 mm diameter Si-wafer anode, an air cathode and aqueous 5 M KOH electrolyte. In total 3 ml electrolyte was filled in a reservoir (a simple PFA tube). After flooding of the cell container and the supply lines, 1 ml electrolyte remained in this reservoir. The different gas and electrolyte flow rates are specified in the descriptions of the experiments. The *in-operando* measurements were performed with an rf pulse power of 300 W, a pulse length of 9 µs, a pulse delay of 10 s and a probe temperature stabilized to 25 °C with a nitrogen gas flow of 800 l/h.

3.4.3. Cycling protocols

LCO vs. Li-metal **cell 1** and **cell 2** for current rate capability comparisons (chapter 4.3, Fig. 22) were allowed to equilibrate for 10 h after the assembly. Then the cells were cycled between 3.0 V and 4.3 V with current rates of C/10, C/5, C/2 and 1C (3.96 mA) each applied for five cycles. Hereon repetition cycles with C/10 and C/5 were performed.

LCO vs. graphite **cell 3** for long-time cycling experiments (chapter 4.4, Fig. 23 left) was cycled in a voltage range of 3 V to 4 V. After the assembly and 5 h open circuit voltage (OCV) two cycles with a current of C/10 (≈0.4 mA) followed by two cycles with C/5 were performed for formation. After these cycles a current of C/4 (1 mA) was applied until the capacity dropped to 1 mAh after around 1100 h. Then the charge/discharge current was reduced to 0.5 mA and cycling was continued until the cell capacity dropped to 0.5 mAh after approximately 2400 h. Hereon a current of 0.25 mA was used for the remaining time of this work. Thereby the duration of the charge/discharge cycles was kept above one hour. In total, cell 3 was operated for more than 3100 h and accomplished 1059 cycles.

LCO vs. graphite **cell 4** for long-time cycling experiments (chapter 4.4, Fig. 23 right) was allowed to equilibrate for 10 h after the assembly. For the first four cycles within 230 h a voltage range of 3.0 V to 4.3 V and low currents (C/80 (0.05 mA) and C/20 (0.2 mA)) were used. Then the cut-off voltage was set to 3.3 V and the current was increased to C/8 (0.5 mA) for one cycle. The next cycle was performed with C/4 (1 mA) for charging and C/8 for discharging. Then a current of C/4 was applied for cycling the cell until the discharge capacity dropped to zero. After approximately 1040 h and 340 cycles the remaining discharge capacity was just above 0.1 mAh. The cell was then refreshed by applying currents of C/40 (0.1 mA) for one cycle, followed by C/16 (0.25 mA) for two cycles. Hereon the cycling was continued with C/8 current in the voltage range from 3.3 V to 4.5 V for approximately another 750 h and 240 cycles. Finally the current was reduced to C/16 and 200 additional cycles were performed between 3.0 V and 4.5 V. Thereby an operation time of more than 2400 h in total with approximately 800 cycles was accomplished.

LCO vs. graphite **cell 5** for long-time cycling experiments (chapter 4.4, Fig. 24 left) was allowed to equilibrate for 10 h after the assembly. The first five cycles within 190 h were performed within a voltage range of 3.0 V to 4.3 V and with low currents of C/80 (0.05 mA), C/20 (0.2 mA), C/13 (0.3 mA) and C/8 (0.5 mA). Then a voltage range of 3.6 V to 4.3 V for the next cycles with C/4 (1 mA) current was applied. The discharge capacity dropped to 0.9 mAh after 400 h (82 cycles) and the current was reduced to C/8 to maintain a cycling duration above 1 h. After 663 h (166 cycles) and a remaining discharge capacity slightly above 0.5 mAh the current was reduced to C/16. Finally, when the discharge capacity deceased below 0.1 mAh after 1410 h (564 cycles), the current was reduced to C/40. No significant discharge capacity (<0.05 mAh) was found after 1535 h (621 cycles). Hereon cycling was continued in a voltage range of 3.0 V to 4.3 V and a voltage-hold time of 10 min without a remarkable gain in capacity.

Li-metal vs. graphite **cell 6** for long-run *in-operando* NMR measurements (chapter 4.4, Fig. 24 right and chapter 5.2, Fig. 29 and Fig. 30) was cycled in a voltage range of 3 V to 1 mV. After the assembly and 5 h OCV the first discharge was performed with a current rate of C/43 (0.1 mA) and a voltage-hold at 1 mV for 20 h. Hereon one cycle was performed with C/4.3 (1 mA) followed by 1.5 cycles with C/2.15 (2 mA). Then a current of C/8.6 (0.5 mA) was applied. Different voltage-hold times of 1 h to 4 h were tested. After 88 cycles within 1400 h dendrite growth led to a short circuit.

Li-metal vs. graphite **cell 7** for *in-operando* NMR (chapter 5, Fig. 27 and chapter 5.1, Fig. 28) and *in-situ* EIS experiments (chapter 4.5, Fig. 26) was cycled in a voltage range of 3 V to 1 mV. After an initial OCV period of 10 h three and a half cycles with a current of C/10 (0.43 mA) were performed during the NMR measurement. Then cell 7 was cycled with C/4.3 (1 mA) with stops (hold for 20 minutes) for EIS measurements at 150 mV during charge and 165 mV during discharge. Before the EIS measurement, the cell was allowed to equilibrate for 10 minutes.

LCO vs. Li-metal **cell 8** for *in-operando* NMR measurements (chapter 6.1, Fig. 32) was cycled between 3.0 V and 4.3 V with C/10 (≈0.4 mA) current after an initial OCV period of 10 h. During the seventh discharging a short circuit occurred. The short circuit was found by a post-mortem analysis and was caused by a microstructure growth at the edge of the separator.

LCO vs. graphite **cell 9** for *in-operando* NMR measurements (chapter 6.2, Fig. 33) was allowed to equilibrate for 10 h after the assembly. Then the cell was cycled in a voltage range between 3 V and 4 V with a current rate of C/10 (≈0.4 mA). In-operando NMR measurements were conducted for the first five cycles and hereon the cycling was stopped.

LCO vs. graphite **cell 10** for *in-operando* NMR measurements (chapter 6.2, Fig. 34) performed at an early stage of this work was cycled with a lower cutoff voltage of 3.0 V and different upper cutoff voltages after an initial OCV period of 10 h. For the first charging current rates of C/80 (0.05 mA) for 55 h and C/40 for another 10 h with an upper cutoff voltage of 4.3 V were used. Hereon the first discharge was performed with C/20. Then charging with an upper cutoff voltage of 4.8 V and discharging were performed with C/20 for one cycle. For the third charging current rates of C/20 for 6 h and C/13.3 (0.3 mA) for another 8 h with an upper cutoff voltage of 5.0 V were used. Then the third discharging was performed with C/13.3. At the end of the fourth charging with C/13.3 a chain of eight voltage holds at 4.8 V and OCV steps as well as a chain of eight voltage holds at 5.0 V and OCV steps were applied. Hereon the cell was discharged with C/13.3 for a last time.

LCO vs. graphite **cell 11** for *in-operando* NMR measurements during fast charging at -20 °C (chapter 6.3, Fig. 35) was allowed to equilibrate for 8 h after the assembly. To induce Li plating the cell was charged by applying 4.3 V. This led to an initial current of approximately 0.4 mA, which decreased to 0.1 mA within 1 h. A formation of metallic Li was not observed and thus the cell was discharged by applying 3 V. Hereon charging was performed with a current rate of C/2 (2 mA) but again no Li plating was found. Thus, again the cell was discharged with C/10. Then the cell was charged by applying 10 V for 8 h while the current was free to take any value. Therefore the charging current started with a peak value of 12 mA (3C-rate) and decreased to approximately 0.25 mA within 2.5 h. In this case the NMR measurement revealed the formation of metallic and microstructured Li on the graphite electrode. Hereon the cell was allowed to equilibrate for around 100 h, while the NMR measurement was continued for 32 h. Then the temperature was set to 20 °C and cycling was performed with a current rate of C/4 (1 mA) and a voltage range of 3.0 V to 4.3 V. Cycle by cycle the capacity decreased such that after 30 cycles within approximately 200 h a cell capacity below 1 mAh was found.

Si-air **cell 12** for testing the metal-air *in-operando* NMR container (chapter 7.3, Fig. 43 left) was allowed to equilibrate for 5 h after the electrolyte flow (approximately 1 ml/min) was started. Then the discharge was started with a current density of 0.026 mA/cm^2 (10 µA). An air supply was not used. After 15 h the pump rate of the electrolyte supply was reduced to around 0.01 ml/min and after 30 h discharging the electrolyte pump rate was increased again for a flow rate of 1 ml/min. Another 12 h later, after approximately 42 h discharging, the pump was switched off and a few hours later first cell voltage

disturbances occurred. These voltage breakdowns became more frequently and after 50 h the discharge was stopped.

Si-air **cell 13** for *in-operando* NMR measurements (chapter 7.3, Fig. 43 right) was allowed to equilibrate for 6 h after the electrolyte flow (2 ml/min) was started and a synthetic air supply (10 ml/min) was used. The discharge current was increased stepwise up to 0.26 mA/cm^2 (0.1 mA). Further increasing the current led to a voltage breakdown. A second discharge (Fig. 44 left) of Si-air cell 13 during *in-operando* NMR measurements (Fig. 45) was performed after full recovery of the OCV. About 2 h after a stepwise increase of the current up to 0.26 mA/cm^2 the electrolyte pump rate was reduced to approximately 0.01 ml/min. Therefore the cell voltage was not stable using this high current density and decreased. Even for smaller discharge currents of 0.23 mA/cm^2 and 0.13 mA/cm^2, which were tested after around 5 h of discharging, an ongoing voltage decrease was observed. Thus, after roughly 7 h the electrolyte pump rate was increased step-by-step. Thereby flow rates of approximately 0.03, 0.05, 0.1, 0.125, 0.15 and 0.3 ml/min were tested first. The voltage increased with each flow rate enhancement, but the continuous decrease of the voltage was not stopped with these low flow rates. Thus, the flow rate was increased to 0.5 ml/min and a cell voltage of around 1 V was obtained. This electrolyte flow and thereby the cell voltage were kept constant for around 8 h. Then, a second time the flow rate was decreased to approximately 0.01 ml/min and hence the voltage dropped. This voltage decrease was not stopped after 20 h of discharging by a flow rate increase to 0.5 ml/min and also not by an increase to 1 ml/min after 22 h. Not even without discharging did the voltage recover. After disassembling cell 13 its Si-wafer anode was found broken (photograph in Fig. 44).

4. Performance tests of the *in-operando* NMR setup

The developed *in-operando* cell container in combination with a numerically optimized saddle coil is suitable for NMR investigations of battery cells over hundreds of charge–discharge cycles. For the cell connections thin-film coated contacting sticks can be used (chapter 4.1). To investigate the effects of the contacting sticks on the B_1 magnetic field, calculated nutation curves are compared with measurements performed with 500 nm gold coated PEEK sticks, pure PEEK sticks and solid copper sticks (chapter 4.2).The reliability of the cell container is demonstrated by current rate capability tests with LCO vs. Li-metal electrodes (chapter 4.3) as well as a charge–discharge experiments of LCO vs. graphite cells, including one cell running for more than 3000 hours (chapter 4.4). The possibility for EIS measurements of cells inside the *in-operando* container mounted and connected on the modified NMR probe is demonstrated in chapter 4.5. For an increased resolution a 2D-DRT analysis[97] was applied.
SEM, LSM and sheet resistance measurements (Fig. 18 and Fig. 19) were performed in cooperation with Özgür Aslanbas (FZJ IEK-9) and Andreas Ohligschläger (FZJ IEK-9). Numerical simulations (Fig. 21) were conducted by Dr. Achim Mester (FZJ ZEA-2). The EIS data 2D-DRT analysis (Fig. 26) was performed by Dr. Andreas Mertens (FZJ IEK-9).

4.1. Thin-film connection sticks

Using electrode contacting with thin-film conductive layers[3] attached on PEEK sticks, as described in chapter 3.2, metallic parts inside the rf coil can be minimized. On the surface of these sticks thin-film metal layers are applied by cold-plasma sputtering. SEM pictures (FEI Quanta FEG 650) revealed a

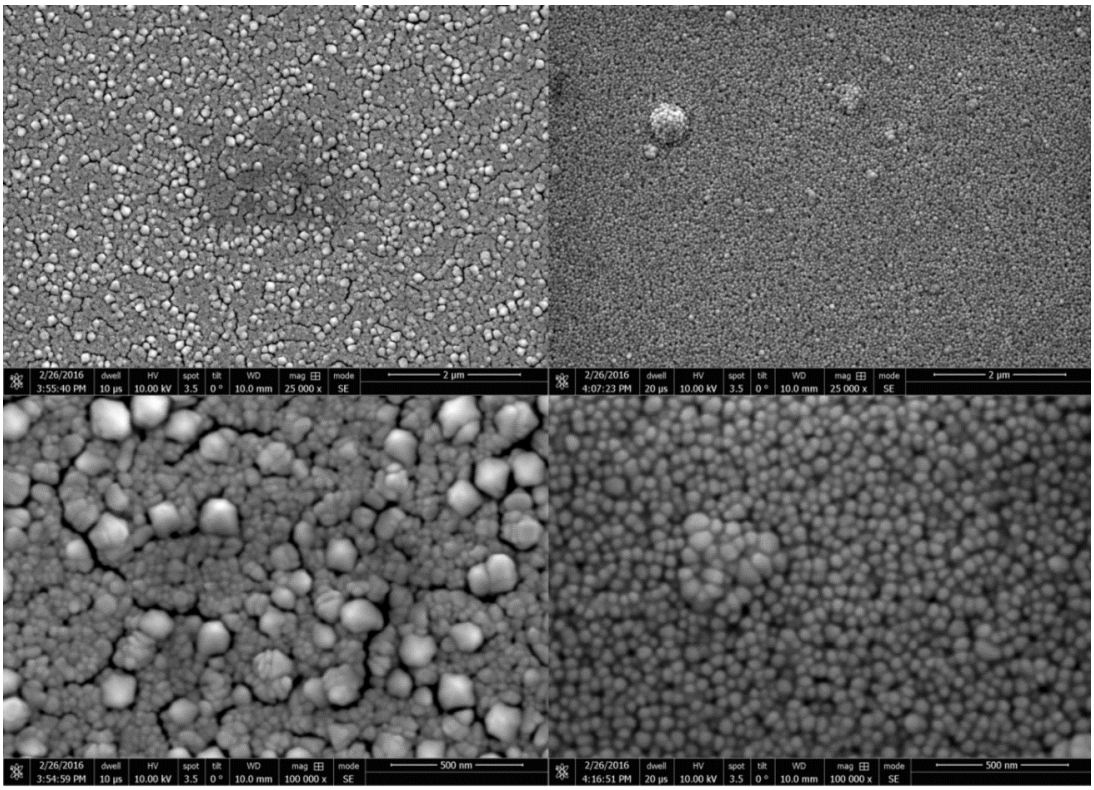

Fig. 18: Scanning electron microscope pictures of two 500 nm gold sputter coatings. *A magnification of 25000 (a,b) and 100000 (c,d) was used. (a) and (c) 30 mA sputter current. The grain size varies between 20 nm to 30 nm but the grains tend to sinter and thus homogeneously distributed particles with sizes of 100 nm to 145 nm surrounded by cracks can be seen. (b) and (d) 60 mA sputter current. The grain size varies between 30 nm to 45 nm. Sintered particles and cracks are found rarely. The SEM measurements were performed in cooperation with Özgür Aslanbas (FZJ IEK-9) and Andreas Ohligschläger (FZJ IEK-9).*

dependence of the homogeneity and the grain size of the conductive coating on the sputter current (Fig. 18). For a 500 nm gold layer deposition, particles with sizes between 20 nm and 30 nm were found using 30 mA sputter current (Fig. 18c). Applying 60 mA sputter current the particle sizes increased to 30 nm to 45 nm (Fig. 18d). Remarkably, the smaller particles sputtered with 30 mA tend to sinter and thereby form bigger grains with sizes of 100 nm to 145 nm. The SEM measurements indicated that this sintering process leads to cracks at their grain boundaries. In accordance to this for 200 nm and 1000 nm gold layer thickness a higher conductivity was found for 60 mA sputter current than for 30 mA (Fig. 19). In case of 500 nm gold layers, the conductivity difference between 60 mA and 30 mA sputter current was very small because both layers exhibited a low resistance close to the optimum. A significantly lower resistance was only found for a 1000 nm gold layer deposited using 60 mA sputter current.

The mechanical stability of very thin (<200 nm) coatings is weak and the electric resistance too high as well as not ohmic such that it increases with increasing current. Thus 1000 nm layers deposited with 60 mA sputter current are favorable.

To verify and characterize thickness and roughness of different conductive layers, PEEK disks and polished Si-wafers were partially covered with Kapton tape and then coated with gold. After sputtering the tape was removed to generate a sharp edge for laser scanning microscopy (LSM) measurements (Fig. 19). The LSM (Olympus Lext OLS4100) enabled an altitude resolution of approximately 10 nm. The characterization of the layers at several edge points revealed deviations from the desired layer thickness up to a few hundred nm (see Fig. 20). One reason could be the age (>20 years) of the sputter device. For the gold layers on PEEK disks the measured altitude profiles were varying much stronger than for gold layers on Si-wafers. The reason was a higher surface roughness of the PEEK disks compared to the Si-wafers such that the sharp altitude profiles were difficult to find. For the 100 nm

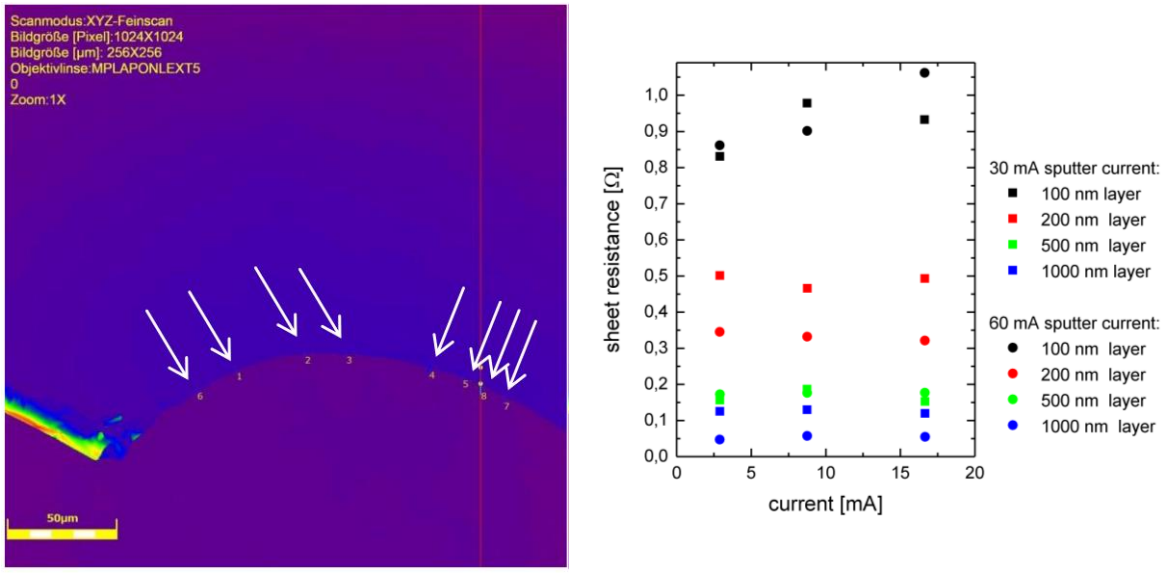

Fig. 19: Laser scanning microscope measurement of a 100 nm gold layer and sheet resistance of different gold coatings as a function of applied current in a four probe measurement. *Left: A tape was used during sputter deposition to generate a sharp layer edge on a polished Si-wafer. Eight points at which altitude profiles were measured to determine the layer thickness are marked with white arrows. Right: With increasing gold layer thickness the resistance decreased. In case of 100 nm layers the resistance was current dependent while for thicker layers the four probe measurements indicated an ohmic conductivity. For 200 nm and 1000 nm layers a significant difference between layers fabricated with 30 mA and 60 mA sputter current was found. The LSM measurements were performed in cooperation with Özgür Aslanbas (FZJ IEK-9) and Andreas Ohligschläger (FZJ IEK-9). The sheet resistance measurements were performed with a self-made four probe setup and in cooperation with Andreas Ohligschläger.*

gold layer on PEEK coated with 60 mA only one sharp edge was found such that no standard deviation is given. The measurements of the 500 nm layer on PEEK (30 mA) and the 1000 nm layer on a Si-wafer (30 mA) showed significant deviations from the desired thicknesses. Most likely the heights were determined at tilted edges. In accordance to an increasing standard deviation for increasing layer thickness, the determination of the roughness parameters indicated an increasing layer inhomogeneity with increasing layer thickness.

For *in-operando* NMR applications it is most important that high conductivity and mechanical stability is ensured while at the same time the layer thickness should be well below the skin depth l. For gold l is approximately 6 µm (see chapter 3.2). The produced thin-film conductive layers fulfill these requirements. The main benefit of these layer is that a variety of electrode connection designs become possible. In case of the metal-air cell design (chapter 3.2.3) the gold coating is indispensable for the air cathode contacting. For the Li-ion cell container, the plastic sticks with thin-film conductive coatings can be substituted by solid metal sticks. A significant effect of an increased metal content was not observed, which is in agreement with the numerical simulations presented in the next chapter.

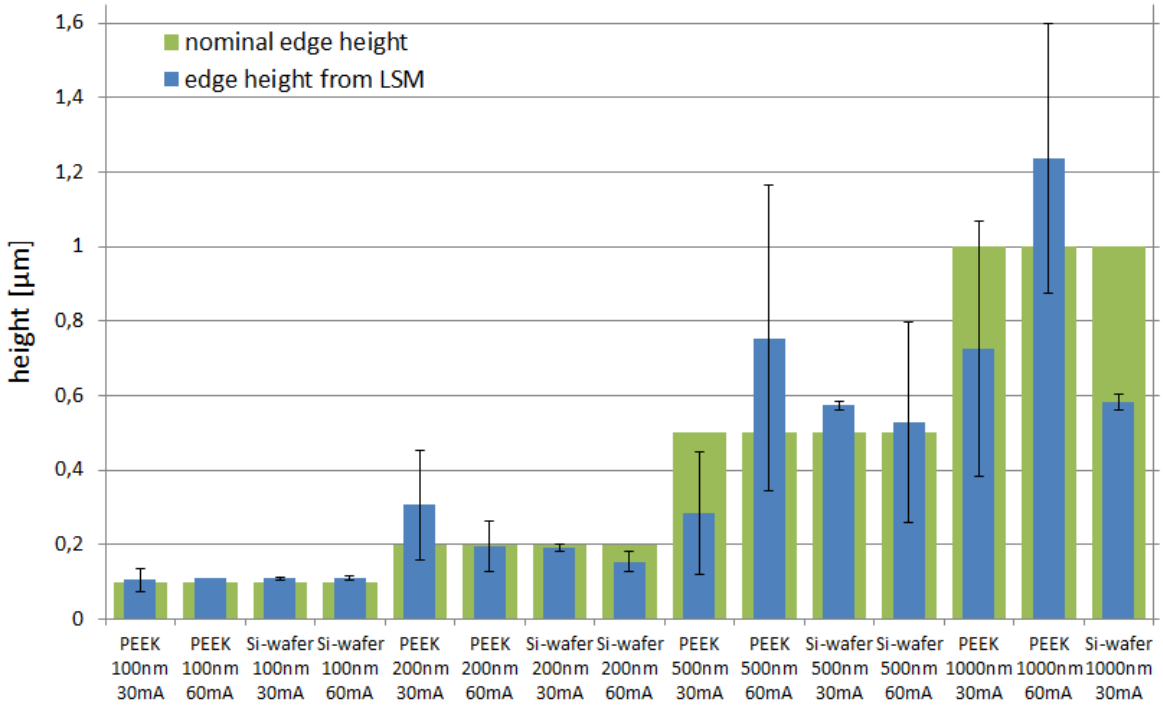

Fig. 20: Edge height of different gold layers measured with LSM. *Altitude profiles were measured at several edge points to determine the layer thickness, as described in Fig. 19. The blue bars show the mean edge heights and error bars give the standard deviation. The LSM measurements were performed in cooperation with Özgür Aslanbas (FZJ IEK-9) and Andreas Ohligschläger (FZJ IEK-9).*

4.2. Numerical simulations and nutation curves of the B_1-field rf coil*

To test the B_1 magnetic field strength and homogeneity of our custom 15 mm saddle coil with solid copper contacting sticks, PEEK sticks with 500 nm gold coating and non-conductive PEEK sticks, spin nutation curves, using the *in-operando* NMR container with LiCl solution, were acquired. On-resonant FIDs were measured with 200 W rf pulse power for pulse durations varied between 0 µs and 600 µs in 2.5 µs steps (Fig. 21d). A pulse power of 200 W instead of 500 W, as used for ^{7}Li *in-operando* measurements, was applied to prevent arcing.

These nutation experiments were compared with simulated nutation curves (Fig. 21c) based on the calculated B_1 field distribution of the rf coil (Fig. 21a,b). Similar ratios of the intensity of the N^{th} maximum divided by the intensity of the first maximum were observed. The differences of the nutation curves with and without conductive sticks were small. Thin-film contacting layer were not included in simulations so far. In experiments an influence of the contacting sticks was not observed for pulse lengths below the π-pulse length of 12.5 µs. Close to the first intensity minimum at around 80 µs, minor distortions of the nutation curve were measured reproducibly with solid copper sticks. For pulses longer than approximately 180 µs all three nutation curves differed slightly. The positions of the maxima were similar for pure PEEK and PEEK with 500 nm coating. For solid copper sticks a slightly faster oscillation was found.

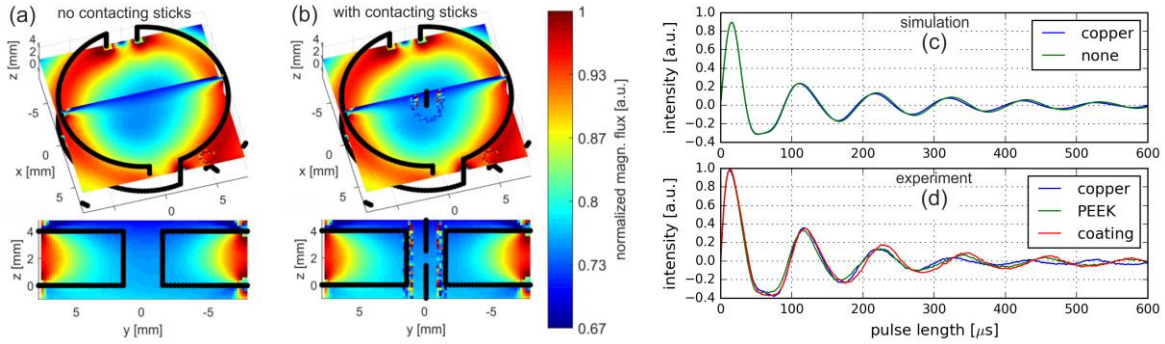

Fig. 21: Numerical simulations of the B_1 magnetic field strength and comparison of calculated and measured nutation curves for different contacting sticks. *(a, b) Black lines indicate the position of the rf saddle coil and the contacting sticks (only b) in the center. Two slices are shown for B_1 field simulations (a) without contacting sticks and (b) with solid copper contacting sticks. (c) From B_1 field simulations calculated nutation curves with and without copper contacting sticks. (d) Measured ^{7}Li signal intensity as a function of rf pulse length for solid copper, non-conductive PEEK as well as PEEK contacting sticks with 500 nm gold coating. The simulations were performed by Dr. Achim Mester (FZJ ZEA-2).*

*****Adapted from Kayser et al.*[1,2]

4.3. Current rate capability*

The charge–discharge capacities with current rates of C/10, C/5, C/2 and 1C (3.5 mA/cm^2) were measured for two LCO vs. Li-metal cells (Fig. 22). Cell 1 was assembled in an *in-operando* container with thin-film contacting sticks and, as a reference, cell 2 in a standard Swagelok PFA housing[57]. The utilized LCO electrodes enabled a maximum current of 1C. Differences of the cell capacities for both cells became more pronounced with increasing current rate. While the standard cell 2 was assembled with a spring, no spring was used for the *in-operando* container because this can disturb NMR measurements.

The correspondingly larger pressure applied on the standard cell 2 could be the reason for its higher rate capability. For the five repetition cycle with C/5 the *in-operando* cell 1 exhibited around 15 mAh/g higher capacities but smaller charge/discharge efficiencies. This efficiency is given by the ratio of discharge capacity divided by charge capacity. For both cells it was above 90 %, except for the first cycle with 1C current. The comparison of the current rate capabilities indicated a suitable cycling behavior of the *in-operando* cell container.

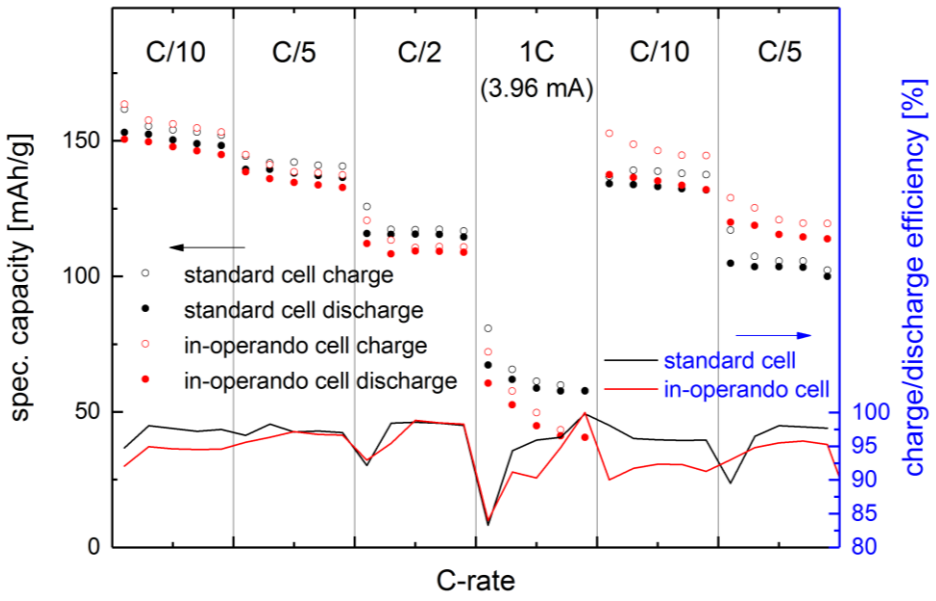

Fig. 22: Current rate capabilities of in-operando cell 1 and standard cell 2. *Comparison of the current rate capabilities of LCO vs. Li-metal cells in an in-operando container with 500 nm contacting layers (red) and in a standard Swagelok cell (black). The cells were cycled in a voltage range from 3.0 V to 4.3 V. Dots indicate the specific capacity for charging (open) and discharging (filled). Lines give the charge/discharge efficiency.*

**Adapted from Kayser et al.*[1,2]

4.4. Long-time battery operation*

To show the long-time reliability of the developed *in-operando* NMR container with thin-film contacting sticks, four cells (cell 3, 4, 5 and 6) were charged and discharged galvanostatically for 3100 h, 2400 h, 1600 h and 1400 h, respectively. The LCO vs. graphite cells 3 and 4 were assembled each with one glass fiber separator. The cell capacity degradations and current (voltage) profiles are shown in Fig. 23. After the first cycles for formation (see chapter 3.4.3) a current of C/4 (1 mA), calculated according to the theoretical capacity of the cells, was applied for cycling the cells.

Cell 3 was cycled in a voltage range of 3 V to 4 V with 1 mA current until the capacity dropped to 1 mAh after around 1100 h (Fig. 23 on the left). Then the charge/discharge current was reduced to 0.5 mA and cycling was continued until the cell capacity dropped to 0.5 mAh after approximately 2400 h. Hereon a current of 0.25 mA was used for the remaining time of this work. Thereby the duration of the charge/discharge cycles was kept above one hour. In total, cell 3 was operated for more than 3100 h and accomplished 1059 cycles. A reason for its capacity degradation could be the use of a relatively thick glass fiber separator instead of a thin polymer separator, as used in commercial cells[98,99]. The LP30 electrolyte was two years old, which could affect the long-time stability as well. Moreover, in daily life applications the cycling voltage range of batteries is controlled by a battery management system, which in general applies a smaller voltage range for fresh cells than for aged cells[100–103]. Thereby the battery capacity can be kept constant for some time and the voltage range increase over time is not noticed by the user. Taking these considerations into account, the developed *in-operando* container exhibits a good long-time cycling behavior.

The LCO vs. graphite cell 4 was cycled with increased upper and lower cutoff voltages of 4.3 V and 3.3 V, respectively (Fig. 23 on the right). As for cell 3, after the first cycles for formation a current of C/4 was applied but cell 4 was cycled until the discharge capacity dropped to zero. After approximately 1040 h and 340 cycles the remaining discharge capacity was just above 0.1 mAh. The cell was then refreshed by applying currents of C/40 (0.1 mA) for one cycle, followed by C/16 (0.25 mA) for two

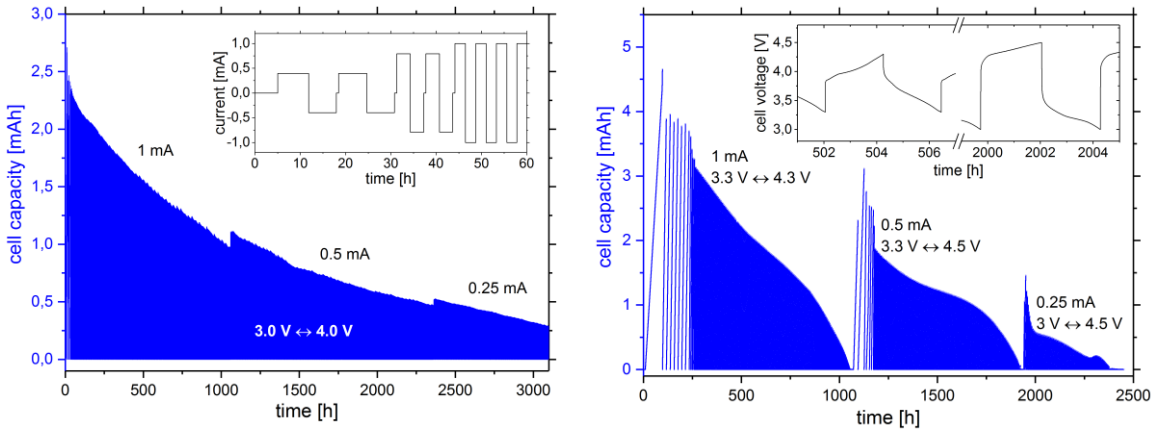

Fig. 23: Capacity degradations of the LCO vs. graphite in-operando cells 3 and 4. *<u>Left</u>: Cycling of LCO vs. graphite cell 3 with one separator during 3100 h. The voltage range was 3 V to 4 V. For the first four cycles within 44 h low currents (C/10 (0.4 mA) and C/5 (0.8 mA)) were used (insert, black). After the formation cycles a current of C/4 (1 mA) was applied. Then the current was reduced to C/8, C/16 and C/40 to maintain a cycling duration above 1 h. In total, 1059 cycles were accomplished within 3101 h. <u>Right</u>: Cycling of LCO vs. graphite cell 4 with one separator during 2400 h. After the first cycles for formation a current of C/4 (1 mA) was applied. The cell was refreshed with C/40 and C/16 current after a capacity drop to zero. Then the current was set to C/8 and later to C/16. The inset (black) shows the voltage profile after 500 h and 2000 h cycling. The cell lifetime even over long times seems to be limited by materials and protocols, not cell housing.*

**Adapted from Kayser et al.*[1,2]

cycles. Hereon the cycling was continued with C/8 current in the voltage range from 3.3 V to 4.5 V for approximately another 750 h and 240 cycles. Finally the current was reduced to C/16 and 200 additional cycles were performed between 3.0 V and 4.5 V. Thereby an operation time of more than 2400 h in total was accomplished in the *in-operando* container. The most obvious reason for the degradation of cell 4 is overcharging[22,55,104] caused by the high voltage limit of initially 4.3 V and later 4.5 V. After 2000 h the cell still exhibits a capacity of around 0.5 mAh. For comparison 12 mm electrodes with high power materials have an initial cell capacity of around 0.5 mAh as well[55].

This demonstrates that properties of the employed material in combination with the cycling program used in the experiment was limiting the cell lifetime, while the contribution of the *in-operando* container was not considerable.

For the LCO vs. graphite cell 5 with two glass fiber separators the capacity degradation and the applied currents are shown in Fig. 24 on the left. The first five cycles within 190 h were performed within a voltage range of 3.0 V to 4.3 V and with low currents of C/80 (0.05 mA), C/20 (0.2 mA), C/13 (0.3 mA) and C/8 (0.5 mA). Then a voltage range of 3.6 V to 4.3 V for the next cycles with C/4 (1 mA) current was applied. The discharge capacity dropped to 0.9 mAh after 400 h (82 cycles) and the current was reduced to C/8 to maintain a cycling duration above 1 h. After 663 h (166 cycles) and a remaining discharge capacity slightly above 0.5 mAh the current was reduced to C/16. Finally, when the discharge capacity deceased below 0.1 mAh after 1410 h (564 cycles), the current was reduced to C/40. No significant discharge capacity (<0.05 mAh) was found after 1535 h (621 cycles). Hereon cycling was continued in a voltage range of 3.0 V to 4.3 V and a voltage-hold time of 10 min without a remarkable gain in capacity. Comparing the capacity degradations of the three LCO vs. graphite cells 3, 4 and 5 indicates a dependence on the number of separators used for the battery assembly, although different voltage ranges were applied.

For the Li-metal vs. graphite cell 6 with three separators slower capacity degradation was found (Fig. 24 on the right). Even after 1390 h cycling with C/8.6 (0.5 mA) the cell still exhibited a capacity of almost 3 mAh (2.65 mAh/cm^2). The Li-metal electrode exhibited a theoretical capacity of approximately

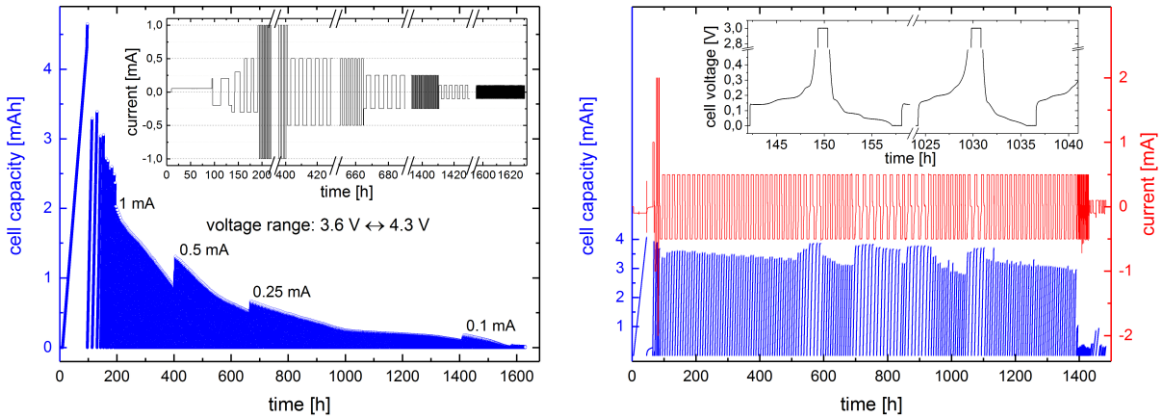

Fig. 24: Capacity degradations of the LCO vs. graphite in-operando cell 5 and the Li-metal vs. graphite in-operando cell 6. *<u>Left</u>: Cycling of LCO vs. graphite cell 5 with two glass fiber separators during 1600 h. After the first cycles for formation a current of C/4 (1 mA) was applied. Then the current was reduced to C/8, C/16 and C/40 (insert, black) to maintain a cycling duration above 1 h. Compared to cell 3 and 4 with one separator, cell 5 showed a faster degradation. <u>Right</u>: Cell capacity degradation (blue), charge/discharge current (red) and voltage profile (insert, black) of the Li-metal vs. graphite cell 6 with three separators assembled for long-run in-operando NMR measurements (chapter 5.2). The voltage range was 3 V to 1 mV. After the first cycles for formation a current of C/8.6 (0.5 mA) was applied and different voltage-hold times of 1 h to 4 h were tested.*

58 mAh due to its thickness of 250 µm. Thus, the cell capacity was limited by the graphite electrode and lost Li could be restocked from the Li-metal surplus. Three separators were chosen to enable a long lifetime despite dendrite growth, which led to a short circuit after 88 cycles within 1400 h (Fig. 25). Thereby long-run *in-operando* NMR measurements of this cell became possible. The NMR results are shown in chapter 5.2. After the short circuit cell 6 was disassembled and photographs were taken (Fig. 25). A porous Li-microstructure was found in all three separators. The separator, which was in contact to the Li-metal electrode, was affected most while the graphite electrode looked like new. Carbonate-based electrolytes have been shown to react with Li-metal and graphite to form a solid-electrolyte interphase (SEI) on the surfaces[105,106]. These SEIs manly consist of Li salts (such as LiF, Li_2CO_3 and Li_2O) from irreversible electrolyte decomposition[107]. A graphite decomposition is prevented by its SEI but the volume expansion of the microstructures during deposition causes the SEI on Li-metal to break and thereby uncovers fresh Li[108]. These sides get covered by a new SEI, which is thinner than on the rest of the Li-metal electrode. Therefore further Li is preferentially deposited at these spots leading to a non-uniform microstructure and thus non-uniform current densities[53,109–111].

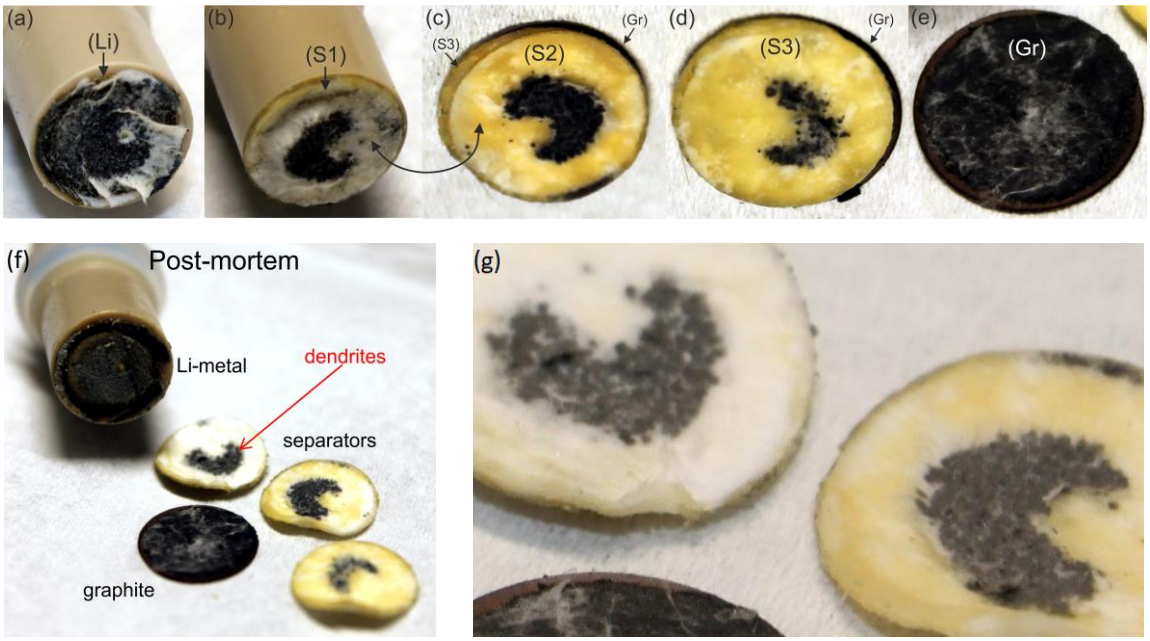

Fig. 25: Post-mortem photographs of the Li-metal vs. graphite cell 6 taken during disassembling. *Li microstructure formation through three separator layers led to a short circuit. (a) Li-metal electrode (Li) on shaft. (b) Separator 1 (S1) on Li-metal electrode. (c) Separator 2 (S2) on separator 3 (S3) on graphite electrode (Gr). Before lifting S2, S3 and Gr from separator 1 on the Li-metal electrode, the two visible faces of S1 and S2 have been in contact. (d) Separator 3 on graphite electrode. (e) Graphite electrode. Remaining glass fibers sticking to the surface are visible. (f) Electrodes and separators. (g) Magnification of the Li microstructure.*

4.5. *In-situ* electrochemical impedance spectroscopy (EIS)*

The Li-metal vs. graphite cell 7 was investigated with electrical impedance spectroscopy after three and a half cycles, in which *in-operando* NMR measurements (chapter 5.1) were performed. Therefore the cell voltage was kept constant on plateaus at 150 mV during charging (25 % state-of-charge (SOC)) and at 165 mV during discharging (85 % SOC). For a higher resolution, the impedance data measured during charge and discharge were analyzed separately by transformation into the relaxation time domain[112]. Using the kernel of a RC circuit element, a distribution of relaxation times (DRT) was calculated with a regularized inversion algorithm[97]. Since between individual EIS acquisitions at a particular SOC no abrupt changes of the DRT were observed, inversion was performed in a single calculation using the full two-dimensional (2D) data set, with regularization also along the non-inverted second dimension represented by the cycle number. Thereby the smoothing effect of the regularization benefits the achievable resolution for the DRT and outliers can be more easily spotted[113]. Since considerable

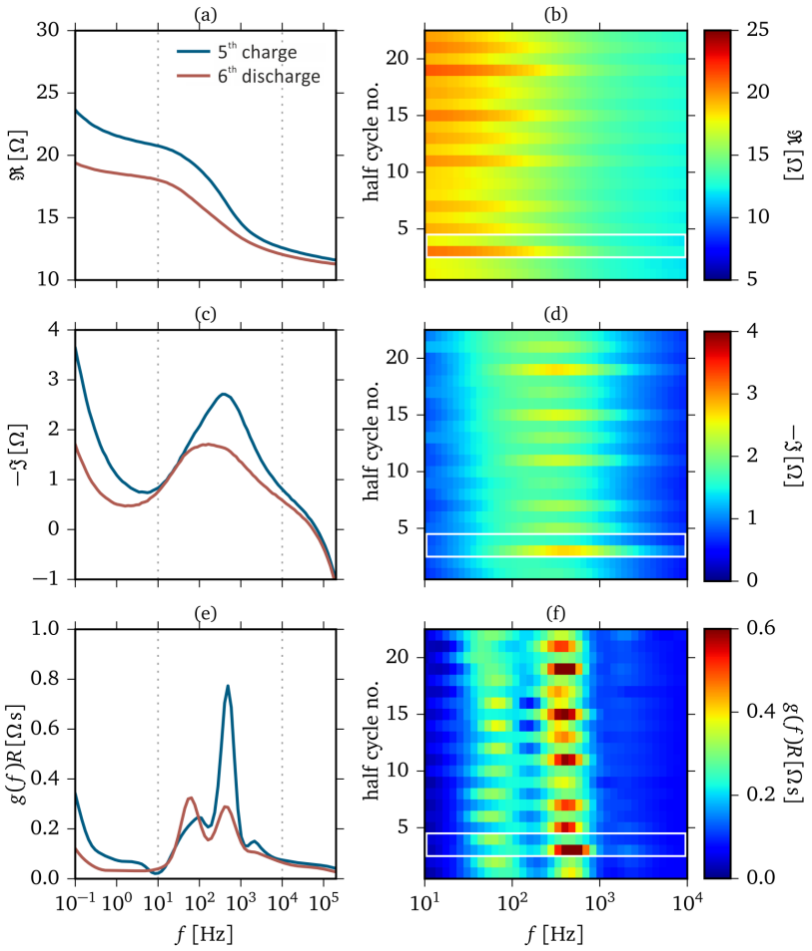

***Fig. 26: In-situ EIS of the Li-metal vs. graphite cell 7 during eleven charge/discharge cycles.**. The cell voltage was kept constant at a SOC of 25 % during charging (blue curves) and at 85 % SOC during discharging (red curves). (a, c and e) Second cycle recorded with EIS, corresponding to the fifth charge and the sixth discharge cycle overall, as a representative example. (b, d and f) Full data sets, showing the evolution of the impedance. The spectra corresponding to the second cycle are framed with a white box. The half-cycle numbering used for the ordinate was started with the eighth half-cycle of the battery, which followed the seven half-cycles measured by NMR (Fig. 28). (a–d) Bode plots, representing the real (a and b) and the imaginary (c and d) part of the EIS data. (e and f) Spectra of the same data in the relaxation time domain (depicted as frequency). The 2D-DRT analysis was performed by Dr. Andreas Mertens (FZJ IEK-9) independently on the charge and the discharge data sets and then merged in chronological order of the acquired spectra.*

**Adapted from Kayser et al.*[1,2]

differences could be observed between different SOCs, 2D-DRT inversion was performed separately for the spectra at 25% SOC and at 85% SOC, and the DRT spectra were reassembled into chronological order after the inversion. The DRT inversion was calculated using a home-written Python module.

EIS data of cell 4 during eleven charge/discharge cycles, recorded immediately after in operando NMR, are depicted in in Fig. 26, starting with a charging step. The fifth charge and the sixth discharge of the cell are shown as a representative example in in Fig. 26a, c and e. The data showed a considerable impedance change between 25 % SOC during charging and 85 % SOC during discharging in the frequency range between 10 Hz and 10 kHz that is commonly attributed to surface layer and charge transfer effects[114,115].

With the higher spectral resolution of the 2D-DRT analysis (Fig. 26e), three overlapping subprocesses become apparent. Their evolution is clearly resolved in Fig. 26f. The ordinate in Fig. 26e and the color in Fig. 26f depict the product of the distribution of relaxation times $g(f)$ and the polarization resistance R, thus the area under each peak represents the corresponding process resistance[97]. The dominant resistance contribution oscillated between the two peaks between 10 Hz and 1 kHz for subsequent half cycles. At 25% SOC during charging the central one of the three processes at about 500 Hz was dominant, while at 85% SOC during discharging the amplitude of the slower one at about 60 Hz increased and the two faster ones decreased.

For the identification of the peak processes, the impedance results may be compared to the NMR results (chapter 5.1). At a SOC of 25 %, the dominant peak at a frequency f of approximately 500 Hz in the EIS spectrum coincides with the minimum of the porous Li-metal peak and the maximum of the signal from lithium intercalated into the graphite electrode in the NMR spectra (Fig. 28). This implies that the impedance process at f = 500 Hz could be caused by an increased diffusion resistance at a higher lithium loading of graphite, which has been shown to exhibit comparably significant changes upon Li intercalation into graphite.[116]

At 85% SOC, there is a strong NMR signal of microstructured lithium on the lithium metal electrode, which can lead to an increased impedance[117]. This increased NMR signal coincides with an increase of the lower frequency process at f = 60 Hz in the EIS data, which therefore could be assigned to an increased resistance at the Li-metal surface.

A correlative analysis by in operando NMR and high-resolution EIS can help to identify processes relevant for the electrochemical impedance response of a battery. Because EIS is much more sensitive to reactions on the surface of a material than NMR, processes which may not be observable by NMR, can be considered as well in a quantitative description of the transport and transformation in a battery cell.

5. NMR experiments on Li-metal vs. graphite cells*

In a Li-metal vs. graphite battery Li gets reversibly intercalated into the graphite electrode during discharge and deintercalated during charge[118]. Using ^{7}Li *in-operando* NMR the formation of different stages corresponding to LiC_{18}, LiC_{12} and LiC_6 leads to spectral lines at 13 ppm, 42 ppm and 37 ppm, respectively[21,22,25,119–121]. During charge the Li is deposited in a microstructured morphology on the Li-metal electrode[47,122,123]. The morphology of this Li microstructure depends on various parameters like temperature, charge/discharge rate and the electrolyte composition[124,125]. The growth of these microstructures can be measured by *in-operando* NMR as well (Fig. 27). Their signals overlap with the Li-metal signal and with each other, but the line centers differ. A fitting of the spectrum can be used to distinguish between mossy (261 ppm), dendritic (270 ppm) and metallic (246 ppm) structures (see chapter 2.2.3, Fig. 8). This was verified by simulations, scanning electron microscopy (SEM) and ^{6}Li/^{7}Li isotope NMR studies[19]. Bulk magnetic susceptibility effects lead to orientation dependent frequency shifts[27,32]. It is assumed that mossy Li grows parallel to the electrode surface and more densely then dendritic Li, which is assumed to grow more or less perpendicularly to the surface, thus parallel to the direction of the applied electric field[126].

The Li-metal vs. graphite cell 6 was used for long-run cycling (chapter 4.4) in combination with NMR investigations, which are the topic of chapter 5.2. Cell 7 was used to investigate the onset of the Li microstructure formation with *in-operando* NMR (Fig. 27 and chapter 5.1). Hereon cell 7 was used for *in-situ* EIS measurements, which are discussed in chapter 4.5.

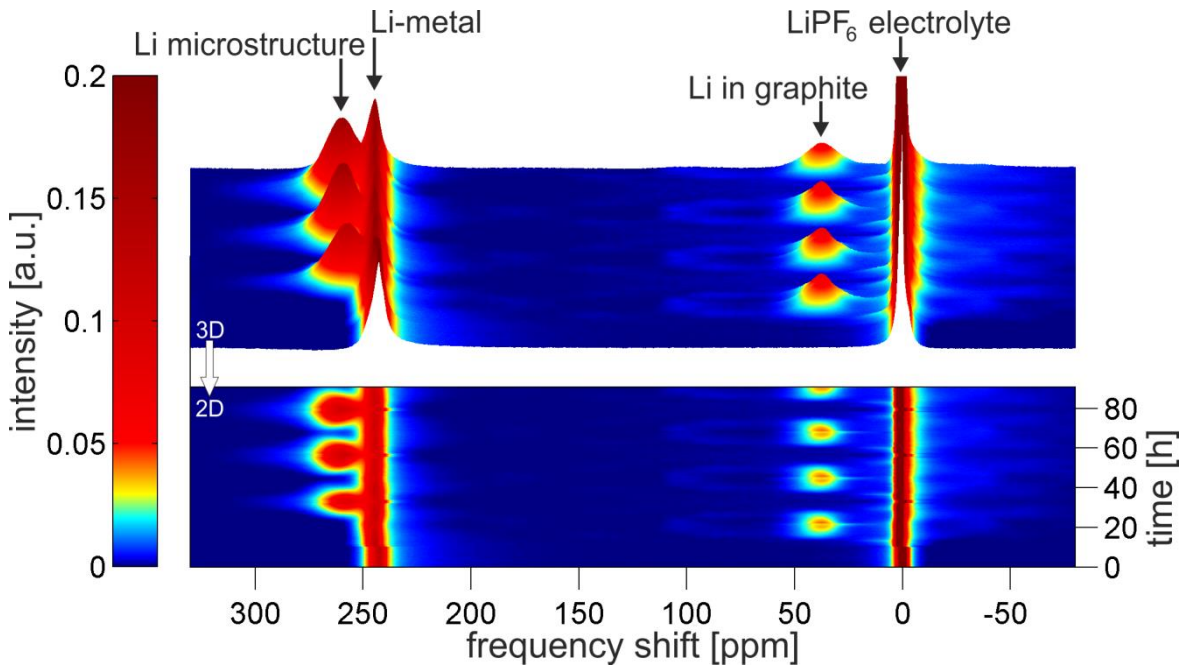

Fig. 27: ^{7}Li in-operando NMR spectra of the Li-metal vs. graphite battery cell 7. *During discharging the intercalation of Li in graphite was visible. By charging this process was reversed and a decrease of the Li_xC_6 signals as well as the initial formation of a Li microstructure was observed. This Li microstructure on the Li-metal electrode was not completely removed by discharging such that cycle by cycle stronger signals were found. The spectra were normalized to the pristine electrolyte peak intensity to indicate the small signal amplitude of Li-metal and Li in graphite. Below the 3D graph a pseudocolor plot was projected on a flat surface for better visibility. The same measurement is shown in Fig. 28 as a pure pseudocolor plot together with the current/voltage profile and further discussed in chapter 5.1.*

**Adapted from Kayser et al.*[1,2]

5.1. Li microstructure formation on Li-metal electrodes*

The Li-metal vs. graphite cell 7 with three glass fiber separators and a cell thickness of 0.3 mm was investigated by ^{7}Li *in-operando* NMR. Fig. 28a shows the charge/discharge profile of the first three cycles with a current of C/10 (0.43 mA) after an initial OCV period of 10 h, and Fig. 28b,c show the time-resolved NMR spectra. Their signal integrals shown in Fig. 28d were obtained by peak fitting as described in chapter 2.2.3.

Signals of the $LiPF_6$ and its products in the electrolyte were composed of at least two overlapping resonances between –1 ppm and 2 ppm[21,127]. For the most intensive signal of mobile Li^+ ions at –0.5 ppm a FWHM of about 150 Hz (less than 1 ppm) was observed. The Li^+ peak intensity divided by the noise standard deviation of the processed spectra gave a signal-to-noise ratio of approximately 2500. The evolution of the electrolyte Li^+ signal integral is shown in Fig. 28d (black line). Most likely the Li distribution in the electrolyte was dependent on the applied current and changed during cycling[44]. An increase of the Li^+ concentration in regions with high B_1 field strength could lead to an enhanced signal. In addition to the electrolyte peaks, the initial NMR spectra showed a single signal of the Li-metal

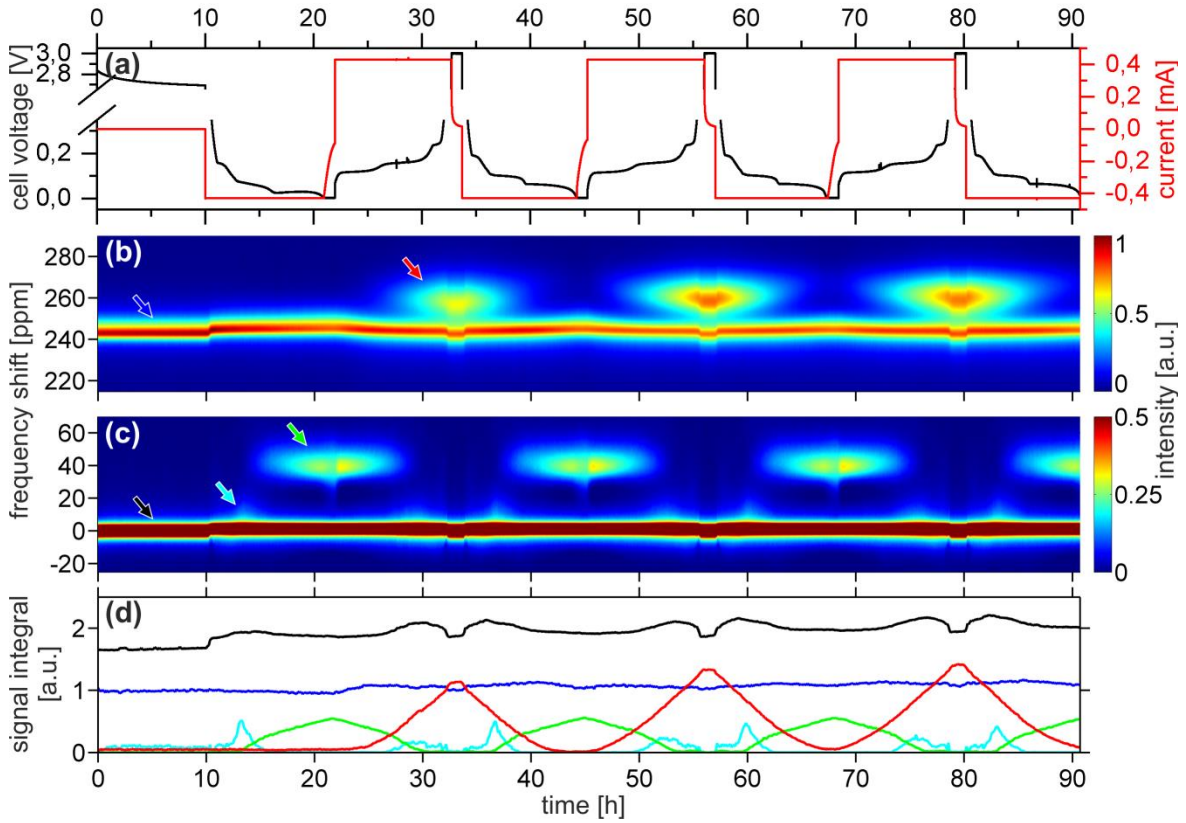

Fig. 28: ^{7}Li in-operando NMR measurement of the first three and a half cycles of a Li-metal vs. graphite battery cell 7. *(a) Charge/discharge voltage (black) and current (red) profiles. (b) Pseudocolor plot of the Li-metal (244 ppm, blue arrow) and Li microstructure (258 ppm, red arrow) signals. The signal was normalized for an initial Li-metal peak intensity of 1. (c) Pseudocolor plot of the electrolyte (-0.5 ppm, black arrow), LiC_{18} (13 ppm, cyan arrow), LiC_{12} (43 ppm) and LiC_6 (38 ppm, green arrow) signals. (d) Signal integral evolution of Li-metal (blue), microstructured Li (red), Li^+ in electrolyte (black), LiC_{18} (cyan, magnified by factor 5), and LiC_{12} combined with LiC_6 (green). The microstructure formation on the Li-metal electrode started with the first charging. By discharging these Li structures were consumed again. The integrals were rescaled such that the initial Li-metal signal integral $I_{LM,0}$ was equal to 1. The NMR measurements were performed with a scan delay of 5 s. For the spectra and the analysis shown in this figure 80 FIDs were averaged giving a temporal resolution of around 6.7 min.*

**Adapted from Kayser et al.*[1,2]

electrode with a FWHM of approximately 1.1 kHz (7 ppm) centered at 244 ppm and with a signal-to-noise ratio of approximately 500.

During OCV at a state-of-charge (SOC) of 100%, the Li-metal and Li^+ signals were stable. Shortly after the beginning of discharging (at a SOC of about 93%), the peak centers of both signals shifted by approximately 300 Hz (2 ppm). During lithiation of the graphite electrode the transition of diamagnetic to paramagnetic graphite takes place[54]. The corresponding susceptibility changes could be the reason for the center frequency shifts and the Li^+ intensity changes. By reversing the current from discharge to charge no similar effects were observed. However, at the end of delithiation, again at an SOC of about 93%, the peaks shifted back to their initial frequency positions. The line shapes were not affected. In experiments on cells without graphite (e.g. LCO vs. Li-metal, chapter 6.1) these effects were not found. In addition, the graphite lithiation led to the growth of a signal centered at approximately 13 ppm at the beginning of discharging. This was reported to be originating from LiC_{18} as a result of Li intercalation[119]. Then signals for LiC_{12} and LiC_6 grew at 43 ppm and 38 ppm, respectively, accompanied by a decrease of LiC_{18}. The reverse process occurred during charging and the NMR spectra showed the delithiation of the graphite electrode. The corresponding voltage plateaus were in accordance with the known staging behavior in graphite[128].

Changes of the Li-metal surface morphology during the first discharge were indicated by rf phase changes of the Li-metal signal in combination with a broadening towards lower field by approximately 300 Hz and a slow decrease of the Li-metal signal integral I_{LM} by around 3%. The reason could be a roughening of the Li-metal surface[122,129]. Charging the cell for the first time led to an increasing Li-metal integral I_{LM} by approximately 35% and a Li microstructure signal with a FWHM of about 2.3 kHz (15 ppm) centered at approximately 258 ppm. The increase of the Li-metal signal is in accordance with experiments and simulations in which skin depth issues have been taken into account[15]. A microstructure formation during the first Li deposition on the Li-metal electrode is consistent with several SEM[123,129], optical microscopy[130], X-ray tomography[131] and electron paramagnetic resonance (EPR)[47] investigations. The *in-operando* NMR data showed an almost linear growth and decrease of the Li microstructure signal integral $I_{\mu L}$ for the second half of charging and the corresponding first half of discharging, respectively, as expected for a constant current experiment[15,32,39]. With one electron at most one Li^+ ion can be reduced and deposited on the Li-metal electrode and vice versa[45].

A slope of $dI_{\mu L}/dt \approx 0.13\ \Delta I_{LM,0}$ was calculated by a linear regression during charge, and during discharge the Li microstructure signal decreased to almost zero with approximately the same but negative slope of $dI_{\mu L}/dt \approx -0.13\ I_{LM,0}\ h^{-1}$. This indicated that the previously formed Li microstructure was reversibly removed. Nevertheless, the Li microstructure NMR signals only vanished completely after the first discharge. Remaining signals were found after the next two discharges in combination with an increased maximum Li microstructure signal at the end of each charging. This is consistent with optical microscopy investigations, which revealed the formation of Li microstructures growing out of holes and thereby pushing away the 'old' microstructure layer[130]. Vertically growing microstructures can percolate the separator, as shown in Fig. 25. Once broken or oxidized far enough, they can lose contact, thereby get electrochemically inactive and thus cannot be removed[111]. On the long run these porous Li structures can become large enough to cause a short circuit between the electrodes.

5.2. Long-run *in-operando* NMR of the Li microstructure growth*

To further investigate the formation of microstructured Li, the Li-metal vs. graphite cell 6 was cycled for around 1400 h (Fig. 24) with C/8.6 (0.5 mA). When assembling, the electrodes and the three glass fiber separators were compressed less strongly than in the container of cell 7 until a cell thickness of 0.5 mm was obtained. Due to the duration of the experiment, NMR measurements could only be conducted stroboscopically. The last measurement after around 1100 h cycling is show in Fig. 29 as a 3D surface plot. Remarkably, the intensities of the Li microstructure signals were more than twice as high as the Li-metal intensity. In Fig. 30 the signal evolutions determined by peak fitting are shown.

The cell operation was started with a long discharge for 60 h with C/43 (0.1 mA), including 20 h voltage hold at 1 mV to search for Li microstructure signals caused by overlithiation and plating of the graphite electrode[22]. A Li microstructure signal increase of slightly less than 5% compared to the pristine Li-metal signal $I_{LM,0}$ was found. At the same time, a shifting Li-metal rf phase and a decrease of the signal integral I_{LM} by approximately 5% was observed, indicating changes of the Li-metal surface morphology occurring already during the first discharge. Alternatively, a small amount of metallic Li on top of the graphite electrode may have formed during discharging[22]. Within the first three cycles, $I_{\mu L}$ reached an approximately twice as high maximum value than in the first cell. This is consistent with the finding that pressure on the electrodes reduces the microstructure layer thickness[19]. Another cause could be the increased current rates during the first couple of cycles.

Using a C/8.6 current for long-run operation, with each cycle both the maximum microstructure signal after charging and the minimum signal after discharging increased. Microstructure layers are poorly connected to the Li-metal surface via a few contacting points that can be dissolved during discharging[47,53,123]. As a consequence, parts of the microstructure can become electrochemically inactive and thereby cannot be removed anymore. These disconnected structures, called 'dead Li',

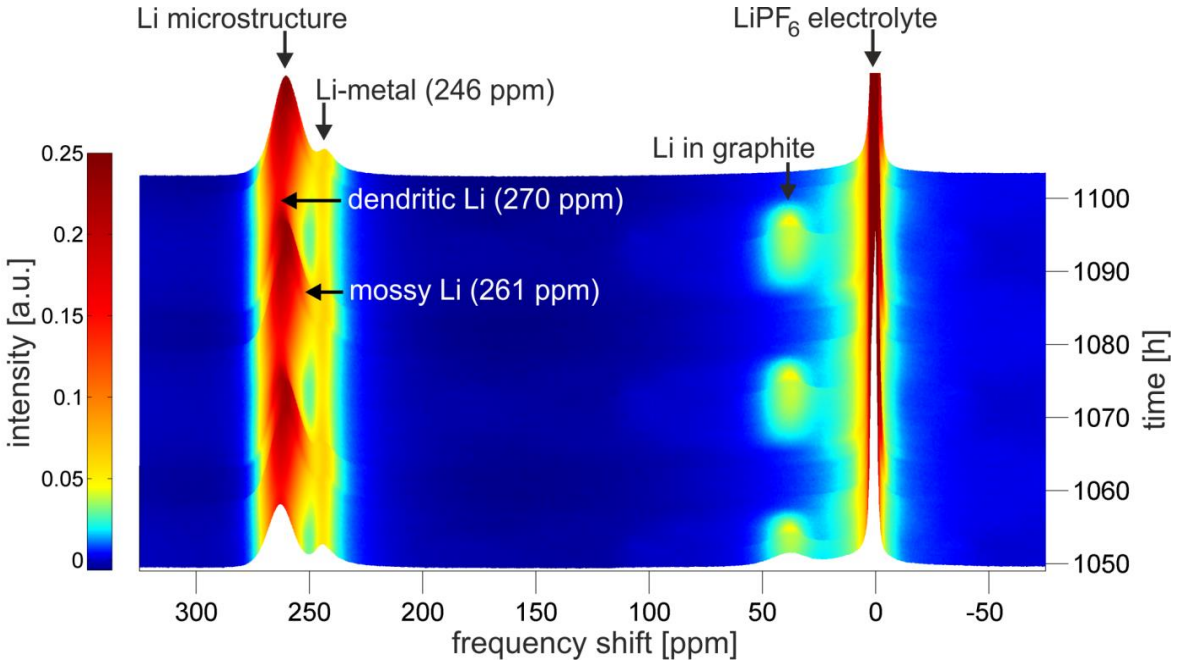

Fig. 29: ^{7}Li in-operando NMR spectra of the Li-metal vs. graphite cell 6 after around 1100 h operation time. *The developed in-operando container enables cycling for several thousand hours. Long-run in-operando NMR investigations can be interrupted such that in between other experiments can be performed. This figure shows a measurement after around 1100 h cell operation time. The measurement is part of a measurement series shown in Fig. 30 together with the signal integral evolutions. To our knowledge, such long-run in-operando NMR investigations have not been reported so far*.*

******Adapted from Kayser et al.*[1,2]

appear to grow quite continuously, which indicates that for a given C-rate in a particular cell the same amount of Li is irreversibly deposited per cycle[47]. For the C/8.6 cycles a linear fit was used to approximate the increase of residual microstructure. A slope of 0.004 $\Delta I_{LM,0}$ for both the maxima and minima of the long-term evolution of $I_{\mu L}$ was found (yellow and green lines, respectively, in Fig. 29b). Different voltage hold times most probably led to small deviations from an exactly linear growth, but non-uniform growth of microstructured Li (Fig. 25) may be another factor.

The line approximating the minima evolution could be extrapolated to the signal integral $I_{\mu L,min}$ at the point of the short circuit at t=1400 h, yielding a value of $I_{\mu L,min}(t=1400\ h) = 4.4\ I_{LM,0}$. It is tempting to speculate that long-run *in-operando* studies could give an estimate for the Li microstructure signal $I_{\mu L}$ at which a short circuit can be expected and use this to estimate the state-of-health at a particular point in time or the cell lifetime under different operating conditions by extrapolation from a much shorter run. However from Fig. 25 it is evident that the formation of dead Li is not necessarily uniform in the whole cell, therefore the suitability of such a method requires better statistical evidence from a larger set of identical test cells.

After an operation time of 1100 h the microstructure signal at its maximum within a cycle reached a value of more than five times the pristine Li-metal signal integral $I_{LM,0}$. Since for thick layers of bulk Li-metal the signal is eventually limited by the skin effect, such a signal increase indicates a fairly complex dependence of the signal amplitude on the cell geometry as well as the morphology of the Li-metal. This shows that each signal component in the Li NMR spectrum of a battery cell needs to be referenced independently for a quantitative data analysis.

Cycle by cycle the average center frequency of the microstructure signal shifted toward lower field (Fig. 30a). Compared to the first cycle, a shift of about 600 Hz (4 ppm) was measured after 1100 h. Slow irreversible growth of porous metallic lithium into the previously diamagnetic electrolyte may increase the effect of Knight shift and thereby cause such a frequency shifts toward lower field[22]. This long-

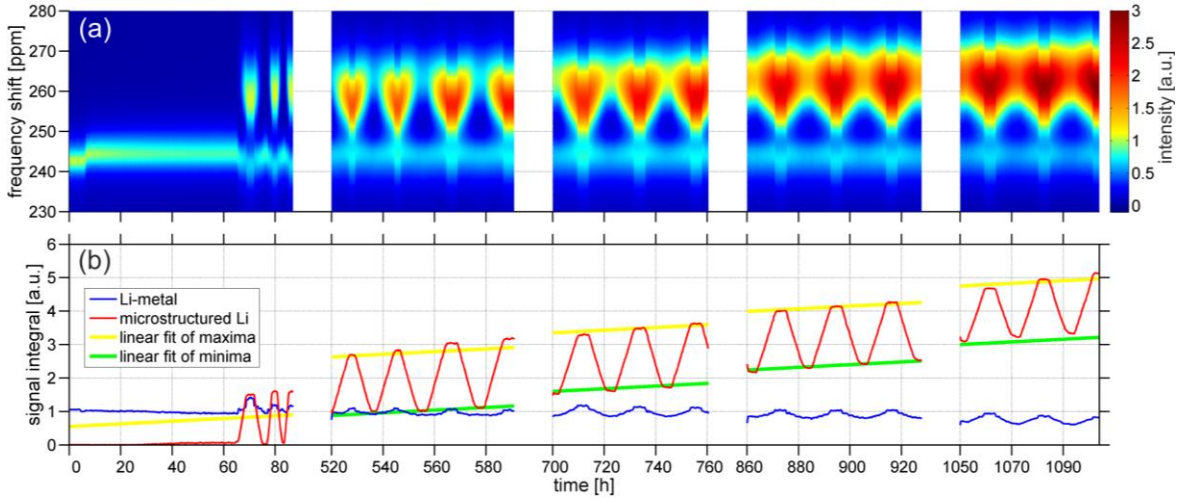

Fig. 30: Long-run ^{7}Li in-operando NMR measurements of the Li microstructure formation in the Li-metal vs. graphite cell 6. *(a) Pseudocolor plot of the Li-metal (244 ppm) and Li microstructure (260 ppm) signals. Within 1100 h the microstructure center frequency shifted by around 600 Hz toward lower field and the signal reached an intensity of more than five times the pristine Li-metal signal. (b) Signal integral evolution of Li-metal (blue) and microstructured Li (red). A linear increase of the maxima and minima of the microstructure signal was approximated by to lines (yellow and green) with a slope of 0.004 $\Delta I_{LM,0}$. In (a) $I_{LM,0}$ was normalized to 1. The integrals in (b) were rescaled such that the signal integral of $I_{LM,0}$ was equal to 1. The charge/discharge profile is depicted in Fig. 24 and post-mortem photographs are shown in Fig. 25. The NMR measurements were performed with a scan delay of 5 s. For the spectra and the analysis shown in this figure 80 FIDs were averaged giving a temporal resolution of around 6.7 min.*

term shift was accompanied by a shift of the microstructure frequency within each cycle by about 3 ppm. An alternating growth and decline of two separate resonances for mossy and dendritic Li was not observed, but a fairly continuous state-of-charge dependent shift, which may be caused by a gradual morphology or density change of the microstructured Li between charged and discharged state of the cell[19]. Furthermore, the almost instantaneous shift by about 1.5 ppm once a certain degree of graphite intercalation was reached, which was previously described for the first cell, could be observed as well for the full cell lifetime. While the resonance frequency of the microstructured Li was fairly selective regarding the state of the cell, the FWHM only changed little between about 15 ppm for the fully charged cell and about 13.5 ppm (2.1 kHz) for the discharged cell.

The slope of the microstructure signal during cycling of cell 6 was showing a somewhat different behavior than for cell 7 that was more strongly compressed during assembly. First of all, $I_{\mu L}$ increased and decreased fairly linearly while Li was deintercalated and intercalated, respectively, from/into the graphite. Using C/8.6 current, the signal evolution after 520 h showed an average slope of 0.27 $\Delta I_{LM,0}$ during charge and of -0.27 $\Delta I_{LM,0}$ during discharge. After 1050 h an average slope of 0.23 $\Delta I_{LM,0}$ during charge and of -0.23 $\Delta I_{LM,0}$ during discharge was observed. For the C/2.15 (2 mA) and the C/4.3 (1 mA) cycles immediately after the formation cycle the signal evolution was less linear, which may have been caused by a less uniform microstructure formation and increased consumption of the bulk metallic Li electrode due to the increased current density[53,109–111].The slope of $I_{\mu L}$ increased for C/2.15 during charging up to 0.8 $\Delta I_{LM,0}$ and decreased during discharging down to at most -0.7 $\Delta I_{LM,0}$. For C/4.3 a maximum signal increase rate of 0.55 $\Delta I_{LM,0}$ and a maximum decrease rate of -0.5 $\Delta I_{LM,0}$ were found. The difference of the slope between charge and discharge, while at the same time the cell efficiency stayed fairly high (Fig. 24), points towards an increased rate at which the bulk Li was consumed at higher C-rates.

6. NMR experiments on lithium cobalt oxide (LCO) cells

LCO electrodes can be used versus Li-metal (cell 8) as well as versus graphite electrodes (cell 9). During charging LCO is oxidized and at the counter electrode Li is deposited on the Li-metal surface or intercalated into graphite (see chapter 2.1.1). NMR can follow these extraction and re-insertion processes in LCO battery cells, as illustrated in Fig. 31. At 0 % SOC the signal of the $LiCoO_2$ active material is centered at approximately -30 ppm and has a FWHM of around 100 ppm[22,25,64]. During charging this LCO signal decreases and a second, broader (≥150 ppm) signal for $Li_{0.5\leq x<1}CoO_2$ emerges and shifts downfield[64]. This process is reversed during discharging.

Using LCO vs. Li-metal a Li microstructure is growing (chapter 6.1). In LCO vs. graphite cells a Li microstructure formation does not occur under moderate cycling conditions (*i.e.* C-rates below 1C and temperatures above 0 °C), but *in-operando* NMR measurements indicated non-reversible LCO phase transformations depending on the upper cutoff voltage (chapter 6.2). Using cell potentials above 4.2 V (vs. the Li/Li^+ redox potential) leads to an increased capacity degradation (as also shown in chapter 4.4). For many applications fast charging is beneficial, but it can result in the formation of metallic and microstructured Li on the graphite electrode. In-operando NMR measurements can follow this Li plating process and thus could enable to determine possible low-temperature cell capabilities like the maximum charging rate. In chapter 6.3 a fast charging experiment on the LCO vs. graphite cell 11 at -20 °C is presented.

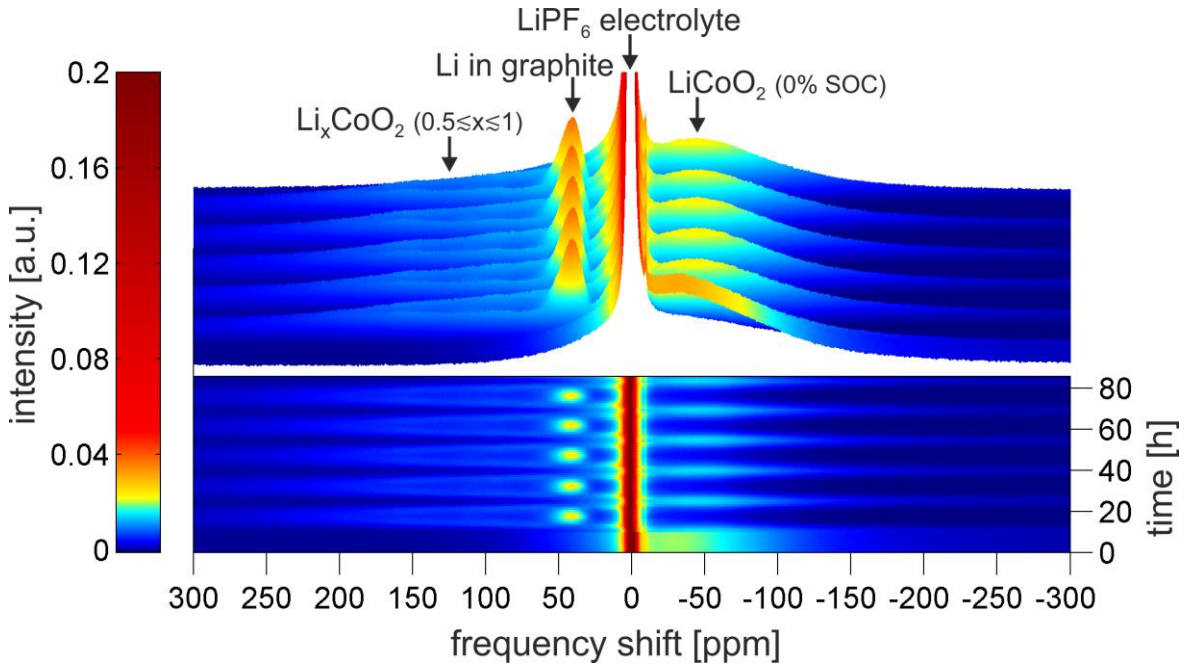

Fig. 31: ^{7}Li in-operando NMR spectra of the LCO vs. graphite battery cell 9. *During charging the intercalation of Li in graphite (42 ppm) as well as the oxidation of LCO and therefore a $LiCoO_2$ signal (-30 ppm) decrease were visible. During Li extraction from LCO the center frequency of the $Li_{0.5\leq x<1}CoO_2$ signal shifted towards higher frequencies up to 120 ppm. By discharging these processes were reversed and a reformation of LCO was observed. For a high reversibility the upper cutoff voltage at the end of charging was set to 4.0 V and thus the amount of extracted LCO was below 50 %. The spectra were normalized to the pristine electrolyte peak intensity to indicate the small signal intensity of LCO and Li in graphite. Below the 3D graph a pseudocolor plot was projected on a flat surface for better visibility. The same measurement is shown in Fig. 33 as a pure pseudocolor plot together with the current/voltage profile and further discussed in chapter 6.2*

6.1. Li microstructure formation in LCO vs. Li-metal cells

Similar to the Li microstructure formations in the Li-metal vs. graphite cells 6 and 7, the growth of mossy and dendritic Li was observed by ^{7}Li NMR in LCO vs. Li-metal cells. An *in-operando* measurement of LCO vs. Li-metal cell 8 is shown in Fig. 32. The signal integrals were normalized to the pristine Li-metal signal integral $I_{LM,0}$.

After each cycle in a voltage range between 3.0 V and 4.3 V the amount of remaining Li microstructure increased (Fig. 32b and red line in d). The maxima and minima of the Li microstructure signal integral $I_{\mu L}$ were fitted with two straight lines (yellow and orange in Fig. 32d). Slopes of 0.003 $\Delta I_{LM,0}$ and 0.002 $\Delta I_{LM,0}$ for the maxima and minima, respectively, of the long-term evolution of $I_{\mu L}$ were found. Compared to the slope of 0.004 $\Delta I_{LM,0}$ found for the Li-metal vs. graphite cell 6 (chapter 5.2, Fig. 30), the growth rate of remaining Li microstructures for cell 8 was half. One reason could be the difference of the current rates. For cell 8 a C-rate of C/10 (0.4 mA) and for cell 6 a C-rate of C/8.6 (0.5 mA) in combination with voltage hold steps were applied (Fig. 32a and Fig. 24 on the right). Another reason could be a dependence on the cell materials and slightly different cell pressures[19].

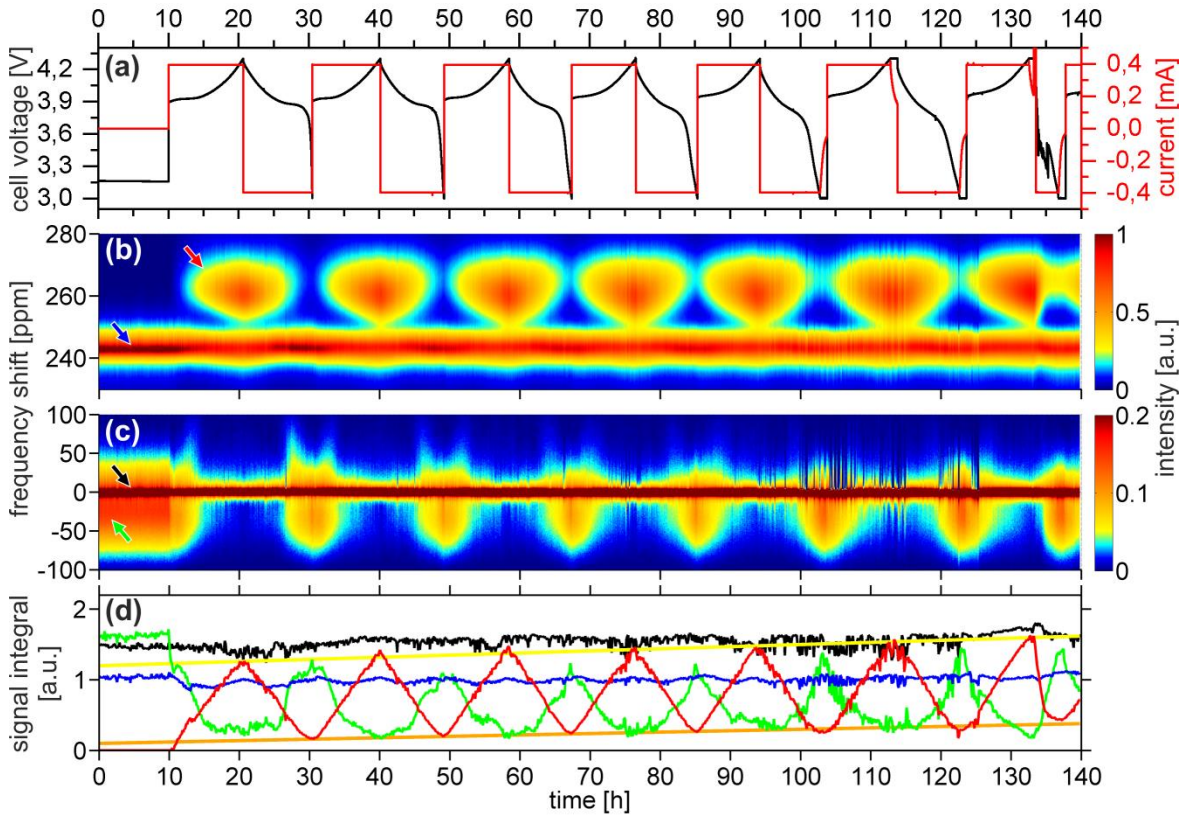

Fig. 32: ^{7}Li in-operando NMR measurement of the LCO vs. Li-metal cell 8. *(a) Charge/discharge voltage (black) and current (red) profiles. The cell was cycled between 3.0 V and 4.3 V with C/10 current. (b) Pseudocolor plot of the Li-metal (243 ppm, blue arrow) and Li microstructure (260 ppm, red arrow) signals. The signal was normalized for an initial Li-metal peak intensity of 1. (c) Pseudocolor plot of the electrolyte (-0.5 ppm, black arrow) and LCO (initially centered at -30 ppm, green arrow) signals. (d) Signal integral evolution of Li-metal (blue), microstructured Li (red), Li^{+} in electrolyte (black) and LCO (green). The microstructure formation on the Li-metal electrode started with the first charging. By discharging these Li structures were consumed again. The LCO integral I_{LCO} (green) is the sum of all Li_xCoO_2 contributions. The integrals were rescaled such that the initial Li-metal signal integral $I_{LM,0}$ was equal to 1. The NMR measurements were performed with a scan delay of 5 s. For the spectra and the analysis shown in this figure 80 FIDs were averaged giving a temporal resolution of around 6.7 min.*

The LCO signal integral I_{LCO} (green line in Fig. 32d) was constant during OCV and immediately decreased by around 30 % at the beginning of the first charging during the very first Li extraction with $\Delta x \approx 0.02$ from $Li_{1.00}CoO_2$ to approximately $Li_{0.98}CoO_2$. One reason could be a kinetic effect due to Li ions slowly diffusing out of the material in competition with more Li extracted from the surface. In LCO Li^+ ions are stored in between CoO_2 layers[60] and changes deep inside the material close to the shielding current collector foil might be invisible for ^{7}Li NMR with an rf frequency of more than 150 MHz. Moreover a slow (spatial) relaxation of Li ions may cause a change of the electron configuration and hence a change in conductivity. Initially the electrical conductivity of $Li_{1.00}CoO_2$ is low and an increase of the Li_xCoO_2 conductivity with decreasing x down to $x \approx 0.5$ was observed[132]. Thereby the concomitant decrease of the skin depth in combination with a Li extraction from regions close to the LCO surface could lead to the rapid signal loss. In this case quite a drastic increase of the conductivity in this small range of $\Delta x \approx 0.02$ would occur. An experiment to verify this hypothesis could be an *in-operando* NMR measurement in combination with *in-situ* EIS as described in chapter 4.5.

The rapid LCO signal decrease was also reported in literature several times[22,64,132,133] and was attributed to the formation of a paramagnetic species. Remarkably, it was claimed *in-operando* NMR could detect a small amount of Li deficiency in LCO due to its high sensitivity to the appearance of paramagnetic centers[35,134,135]. Shimoda et al.[64] suggested that during charging the diamagnetic Co^{3+} ions could be oxidized to paramagnetic Co^{4+} ions. This could lead to a strong electron-nuclear dipolar interaction and thereby to the rapid LCO signal loss. However, in this case, the ^{7}Li NMR signal would not simply go away, but would be converted into a paramagnetically broadened signal. Thus, the occurrence of paramagnetic centers does not cause the loss of NMR signal a priori. Another possibility could be an oxygen redox mechanism ($O^{2-} \leftrightarrow O^-$) in the LCO while the cobalt oxidation state remains constant at Co^{3+}. This was indicated by X-ray absorption spectroscopy[136,137] and *in-operando* EPR measurements[138]. In case of EPR a very strong change of the paramagnetism during the first cycle (from paramagnetic to diamagnetic) was observed, but no paramagnetism afterwards (in particular no Co^{4+} paramagnetism, which is expected to show a very clear signature in the EPR spectrum since it is a spin-1/2 state).

A mixed redox mechanism simultaneously incorporating both cobalt and oxygen oxidation was suggested by *in-operando* magnetometry measurements of the magnetic susceptibility[139,140] and photoelectron spectroscopy in combination with density of states (DOS) calculations[141]. However, the different bands are energetically so close that the conclusions can change completely depending on the exact simulation protocol of ab-initio calculations.

After the rapid decrease at the beginning of the first charging, the LCO signal integral I_{LCO}, which is the sum of all Li_xCoO_2 contributions, increased slightly by around 5 % within approximately 1 h (Fig. 32d). This is in accordance with findings of Shimoda et al.[64] and resulted from a second LCO signal of Li_xCoO_2 with $x < 1$, which was growing with the Li removal. The $Li_{x<1}CoO_2$ signal increased down to $x \approx 0.75$, while for the same period the $Li_{1.0}CoO_2$ signal further decreased. Thereby the sum of all LCO signals I_{LCO} calculated by peak fitting increased for approximately 1 h. Moreover, the signal re-increase could be caused by a kinetic effect such that Li-ions inside LCO diffuse to less shielded regions close to the electrode surface. This might be verified by stopping charging the cell immediately after the 30 % signal drop. In case of a kinetic effect the signal re-increase would not be strictly connected with additional extraction of Li-ions.

Hereon I_{LCO} decreased almost linearly to around 20 % of its pristine value $I_{LCO,0}$ at OCV. This minimum value of 0.2 $I_{LCO,0}$ was reached approximately 3 h before the end of charging (4.2 V) and then I_{LCO} was almost constant. The reason could be the skin depth of the LCO electrode. This might be verified by *in-operando* measurements at different magnetic fields (in particular low fields), which changes the skin depth and allows to distinguish between conductivity induced and paramagnetic effects.
In addition, the center frequency of the $Li_{x<1}CoO_2$ signal shifted towards higher frequency up to around 120 ppm until the end of charging with $x \approx 0.5$. One reason could be the Knight shift associated with the increasing electrical conductivity of $Li_{x<1}CoO_2$[64,132] during charging. Another reason could be a changing susceptibility due to changing lattice constants during insertion and extraction of Li[142].
During discharging the different processes were reversed and Li^+ ions were re-inserted into the LCO electrode. The signal evolutions of I_{LCO} during the discharges were mirrored by the evolutions during the subsequent charges, except of the first charging. After all discharges the LCO signal integral did not fully recover to its pristine value $I_{LCO,0}$. The difference between the maximum of I_{LCO} after discharging and $I_{LCO,0}$ was similar to the rapid 30 % signal decrease at the beginning of the first charging. The reason could be that the discharged LCO still contained a small amount of paramagnetic cobalt oxide because some Li^+ ions were not inserted back to reach $Li_{1.00}CoO_2$. The irreversible capacity loss within the first cycle calculated from the electrochemical measurement was in agreement with a Li amount of $\Delta x \approx 0.02$, which was not inserted back upon discharging. One reason, which may cause an incomplete re-insertion and irreversible capacity loss, could be the SEI formation on Li_xCoO_2[64,106].
Within cycling this maximum LCO signal $I_{LCO,max}$ after discharging and the minimum LCO signal after charging $I_{LCO,min}$ ($\approx 0.2\ I_{LCO,0}$) varied by around 10 %, but no clear trend towards higher or lower values was visible. This indicated a good reversibility of the LCO transformation using a voltage range between 3.0 V and 4.3 V vs. Li-metal. The difference between $I_{LCO,max}$ and $I_{LCO,min}$ was approximately 0.5 $I_{LCO,0}$ for all cycles. In contrast, the shape of the integral evolution changed cycle by cycle and became more linear. This could indicate that the formation was not finished after a single cycle, but that several cycles have to be considered. Alternatively, this could also be due to cell aging or degradation.
During the seventh discharging a short circuit occurred and forced a rapid oxidation of the Li microstructure. The short circuit was found by a post-mortem analysis and was caused by a microstructure growth at the edge of the separator. Even though this involved a rapid LCO reformation, the maximum LCO integral at the end of this discharge was around 70 % of $I_{LCO,0}$ as well. Remarkably, two cycles before the short circuit occurred, significant disturbances of the NMR spectra can be seen. It is tempting to speculate that such signal disruptions may forecast cell problems, but they need to be investigated in more detail. Another reason could be changes of the resonant circuit adjustment, which can cause instantaneous decreases of the signal intensities and phase shifts. The *in-operando* container with segregated NMR reference, which is introduced in the appendix 12.2, might help to determine the reason in future experiments.

6.2. Standard operation and overcharging of LCO vs. graphite cells

Cycling the LCO vs. graphite cell 3 in a voltage range between 3.0 V and 4.0 V enabled a battery operation for more than 3000 h (chapter 4.4). The upper cutoff voltage of 4.0 V for LCO vs. graphite, instead of 4.3 V as used for Li-metal vs. graphite, accounts for the standard potential difference. Compared to the standard potential $E^0_{\mathrm{Li}} \approx$ -3.04 V for the redox reaction describing the metallic Li formation on a Li-metal electrode, the standard potential for the redox reaction describing the reduction of Li^+-ions in graphite is $E^0_{\mathrm{LiC}} \approx$ -2.84 V.

The LCO vs. graphite cell 9 was assembled with three glass fiber separators, 1 µm copper coated PEEK contacting sticks and an electrode spacing of 0.5 mm. An *in-operando* NMR measurement of the first five cycles of cell 9 is shown in Fig. 33. As soon as charging was started a rapid decrease of the LCO signal integral I_{LCO} (green line) down to approximately 70 % of the initial OCV value $I_{\mathrm{LCO,0}}$ was observed (Fig. 33c). Most likely, as for the LCO vs. Li-metal cell 8 (chapter 6.1), the reason was a kinetic effect due to Li ions slowly diffusing out of the material in competition with more Li extracted from the surface or the formation of paramagnetic centers, which led to a strong electron-nuclear dipolar interaction[64,132]. After the rapid decrease, I_{LCO} increased by around 15 % within 2 h. As for cell 8, this could be caused by a re-increase of the Knight shifted Li_xCoO_2 signal due to a changing electron configuration or a Li-ion diffusion toward the electrode surface.

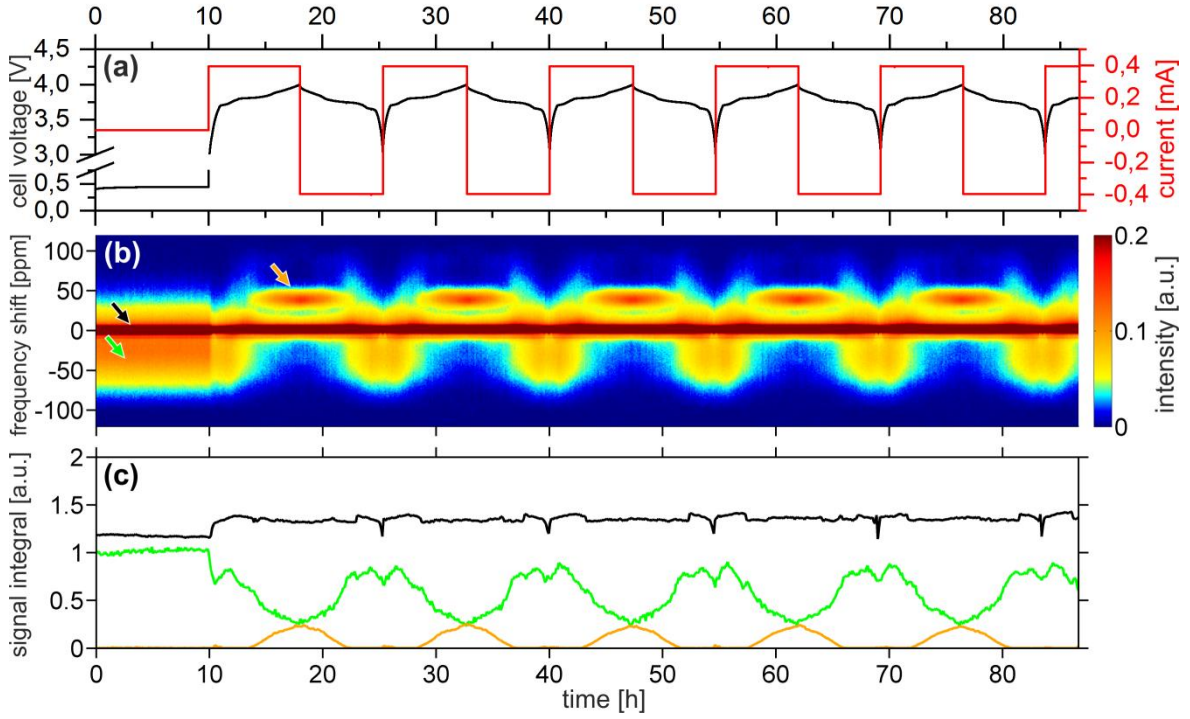

Fig. 33: ^{7}Li in-operando NMR measurement of the LCO vs. graphite cell 9. *(a) Charge/discharge voltage and current profiles. (b) Pseudocolor plot of the LCO (initially centered at -30 ppm, green arrow), electrolyte (-0.5 ppm, black arrow) and LiC_6 (38 ppm, orange arrow) signals. The signal was normalized for an initial electrolyte peak intensity of 1. (c) Signal integral evolution of LCO (green), Li^+ in the electrolyte (black) and LiC_6 (orange). The battery was cycled in a voltage range between 3 V and 4 V with a current rate of C/10 (0.4 mA). The NMR measurement indicated a reversible oxidation and reformation of LCO during charging and discharging, respectively. The integrals were rescaled such that the initial LCO signal integral $I_{LCO,0}$ was equal to 1. The NMR measurements were performed with a scan delay of 5 s. For the spectra and the analysis shown in this figure 80 FIDs were averaged giving a temporal resolution of around 6.7 min.*

At the end of charging I_{LCO} decreased to around 30 % of $I_{LCO,0}$. During discharging I_{LCO} first recovered to around 80 % of $I_{LCO,0}$. Then it stayed constant for approximately the last third of discharging before it decreased by around 10 % at the very end of discharging. The signal decrease could be caused by a diffusion of Li-ions towards the current collector such that the amount of Li in regions within the skin depth of the electrode surface decreases.

The signal evolutions of I_{LCO} during the charging was almost mirrored by the evolution during the discharging, but differences were slightly visible at the beginning of charging compared to the end of discharging. Within the five measured cycles the maximum of I_{LCO} at the end of discharging and the minimum of I_{LCO} at the end of charging were constant. This indicated a good reversibility of the LCO transformation using an upper cutoff voltage of 4.0 V vs. graphite.

Intensity changes and center frequency shifts of the Li^+ signal (black line in Fig. 33) were observed shortly after the beginning of charging and shortly before the end of discharging. The reason could be the transition of paramagnetic to diamagnetic graphite[54] and corresponding susceptibility changes, as described in chapter 5.1 for the Li-metal vs. graphite cell 7.

Using higher cutoff voltages for charging leads to a higher amount of oxidized LCO. This is called overcharging and involves non-reversible changes of the LCO material[22]. An *in-operando* NMR measurement with cutoff voltages of 4.3 V, 4.8 V and 5.0 V is shown in Fig. 34. The LCO vs. graphite cell 10 was assembled with three glass fiber separators, 1 µm copper coated PEEK contacting sticks and

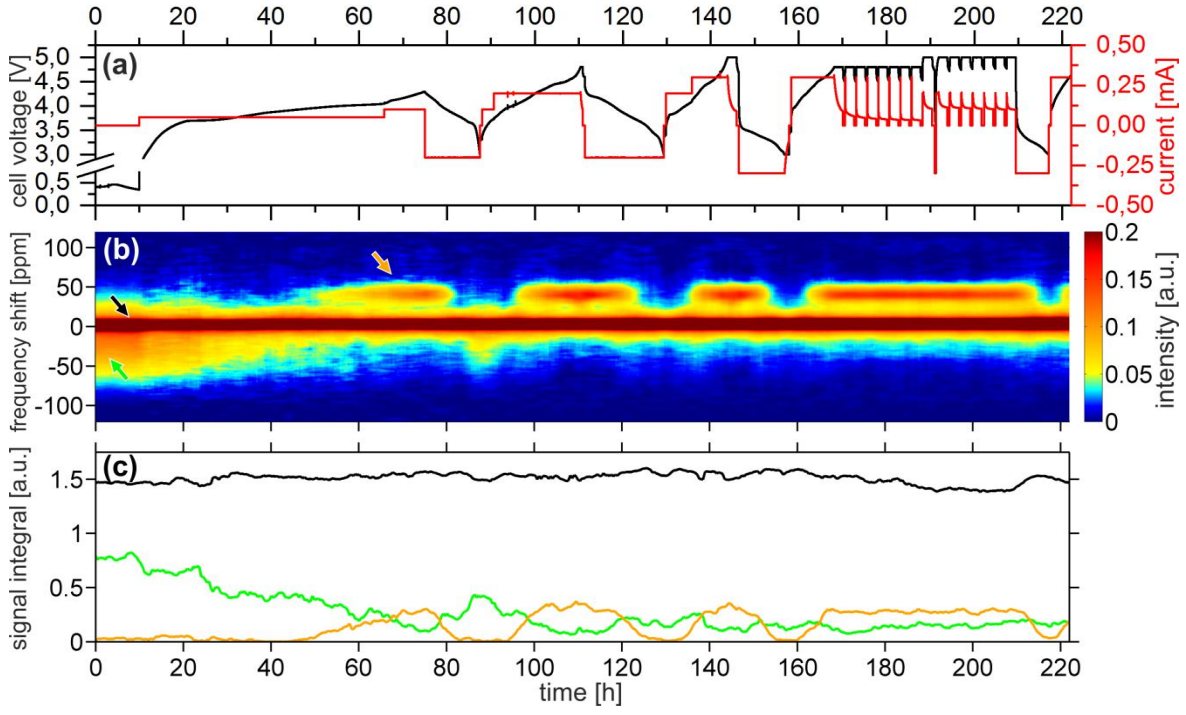

Fig. 34: ^{7}Li in-operando NMR measurement during overcharging of the LCO vs. graphite cell 10. *(a) Charge/discharge voltage and current profiles. (b) Pseudocolor plot of the LCO (initially centered at -30 ppm, green arrow), electrolyte (-0.5 ppm, black arrow) and LiC_6 (38 ppm, orange arrow) signals. The signal was normalized for an initial electrolyte peak intensity of 1. (c) Signal integral evolution of LCO (green), Li^+ in the electrolyte (black) and LiC_6 (orange). The upper cutoff voltage was increased from 4.3 V for the first charging up to 5 V for the fourth cycle. A non-reversible decrease of the LCO signal was observed and indicated overcharging for such high voltages. Moreover, the signal integral of the electrolyte decreased slowly by applying 5 V, indicating most likely a degradation. The NMR measurements were performed with a scan delay of 10 s and a previous version of the battery line filters. For the spectra and the analysis shown in this figure 160 FIDs were averaged giving a temporal resolution of around 26.7 min.*

an electrode spacing of 0.4 mm. Because this measurement was performed at an early stage of this work, a previous version of the frequency filter system for the battery lines was used (for details see appendix 12.4). Thereby the signal-to-noise ratio was smaller by a factor of approximately 20 and to account for this the amount of averaged FIDs was doubled.

After the first charging to 4.3 V the LCO signal still recovered at the end of discharging and a signal integral I_{LCO} of around 50 % of $I_{LCO,0}$ was found. After the second charging to 4.7 V and the subsequent discharge I_{LCO} recovered to approximately 30 % of $I_{LCO,0}$. Using an upper cutoff voltage of 5.0 V for I_{LCO} after discharging a value of around 20 % of $I_{LCO,0}$ was found. After charging with a chain of several voltage holds (at 4.8 V and later 5.0 V) and OCV steps, no recovery of the LCO signal during discharging was found. This measurement indicated that cycling of a LCO battery is the less reversible the higher the upper cutoff voltage is chosen and thus is in agreement with the capacity degradation measurements presented in chapter 4.4.

6.3. Li plating on graphite electrodes at low temperature

Fast charging capabilities of battery cells are important especially for electric vehicles. The shorter travel is interrupted by charging breaks, the more pleasant electro mobility becomes. The maximum charging current of most state-of-the-art Li-ion cells is limited by the graphite electrode[143,144]. Graphite is advantageous in terms of energy density because the redox potential for the Li intercalation reaction is only approximately 200 mV above the Li/Li^+ redox potential[145] (see chapter 2.1.1). This enables cell voltages up to 4 V and higher without using Li-metal, but involves the risk of an undesired solid Li formation upon charging:

$$Li^+(aq) + e^- \xrightarrow{charge} Li(s)$$

This reaction can occur at the graphite electrode when no more Li can be intercalated or if the maximum charge transfer rate is reached and a drop of the local potential below the Li/Li^+ redox potential occurs[146,147]. The onset of this Li plating on a graphite electrode depends primarily on the current density[148,149] and the temperature[147,150], but electrode parameters like SOC, active material loading[151],

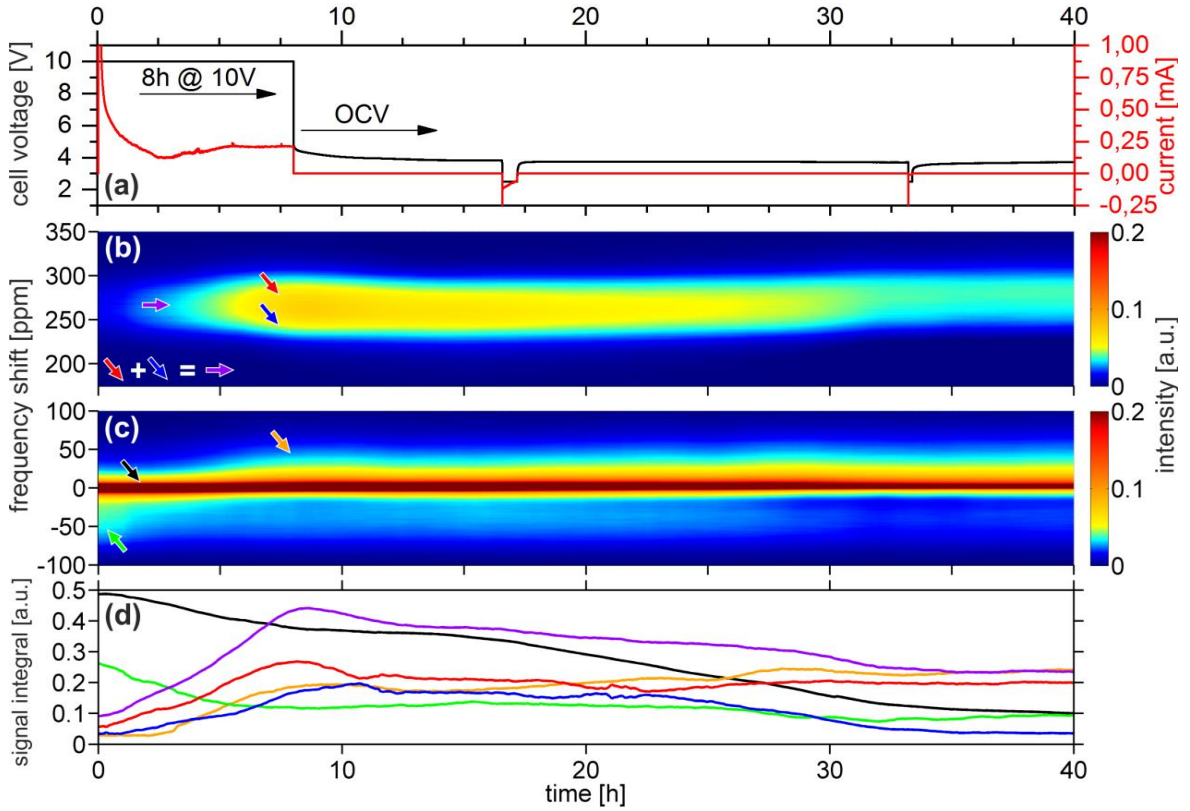

Fig. 35: ^{7}Li in-operando NMR measurement of Li plating in the LCO vs. graphite cell 11 at -20 °C. *(a) Charge/discharge voltage and current profiles. To charge the battery cell at -20 °C as fast as possible, 10 V were applied for 8 h. The charging current started at 12 mA. The current axis ends at 1 mA for a better visibility of the current decrease (red line). (b) Pseudocolor plot of metallic Li (244 ppm, blue arrow) and Li microstructure (270 ppm, red arrow) signals. (c) Pseudocolor plot of the LCO (initially centered at -30 ppm, green arrow), electrolyte (-0.5 ppm, black arrow), LiC_{12} (43 ppm) and LiC_6 (38 ppm, orange arrow) signals. The signal was normalized for an initial electrolyte peak intensity of 1. (d) Signal integral evolution of metallic Li (blue), microstructured Li (red), the sum of metallic and microstructured Li (purple), LCO (green), Li^+ in the electrolyte (black, rescaled by factor 1/3) and LiC_{12} combined with LiC_6 (orange). The in-operando spectra revealed an increase of Li plating during fast charging and indicated a slow diffusion of lithium into graphite. The NMR measurements were performed with a scan delay of 5 s. For the spectra and the analysis shown in this figure 80 FIDs were averaged giving a temporal resolution of around 6.7 min.*

porosity and tortuosity[152] are important factors as well. Li plating leads to a capacity loss caused by active lithium and electrolyte consumption and decreases the current rate capability due to an impedance build-up[149]. Moreover, the formation of conductive Li structures can lead to an internal shorting and thus is a serious safety issue[149].

An *in-operando* NMR measurement of the LCO vs. graphite cell 11 at -20°C is shown in Fig. 35. To induce Li plating, the cell was charged by applying 10 V for 8 h while the current was free to take any value. The reason for this high voltage were several unsuccessful experiments in advance, in which only a very small amount of Li plating was found. By applying 10 V the charging current started with a peak value of 12 mA (3C-rate) and decreased to approximately 0.25 mA within 2.5 h (Fig. 35a).

The signal integral of the electrolyte I_{Li^+} decreased by approximately 20 % during the 8 h of charging with 10 V (Fig. 35d). This indicated a degradation of the electrolyte[20]. After charging I_{Li^+} was almost constant for around 5 h and then decreased with roughly the same rate as found during fast charging. At the end of the *in-operando* measurement I_{Li^+} was decreased to around 20 % of its pristine value.

The *in-operando* NMR spectra (Fig. 35b) showed increasing signals, which could be attributed to metallic Li (248 ppm) and microstructured Li (261 ppm and 270 ppm). Most likely the unsuccessful experiments in advance were the reason for intensities unequal to zero at t = 0 s. However, peak fitting of the spectra revealed a growing amount of Li plating during the whole 8 h of charging (purple line in Fig. 35d). This is schematically depicted in Fig. 36 on the left. Because at -20 C the Li^+ transfer in graphite was slowed down but still possible, the spectra fits showed an increase of the LiC_{12} (43 ppm) and LiC_6 (38 ppm) signals as well. These signals were overlapping with the much broader LCO signal (initially centered at -30 ppm), which shifted towards positive ppm values upon charging. The difference of the peak widths enabled to distinguish between the different signals by using peak fitting.

After charging, the NMR measurement was continued for another 32 h at -20°C and OCV. Within the first 3 h the spectra showed an ongoing increase of the metallic Li signal integral I_{LM} while for the same period the Li microstructure integral $I_{\mu L}$ decreased. This could indicate morphology changes of the plated Li layer like a redistribution of deposited Li structures, which may lead to more dense and thereby metallic accumulations. Within the next 10 h, I_{LM} and $I_{\mu L}$ decreased in parallel by approximately 15 %. This could be attributed to a slow intercalation of parts of the solid Li plating layer into graphite:

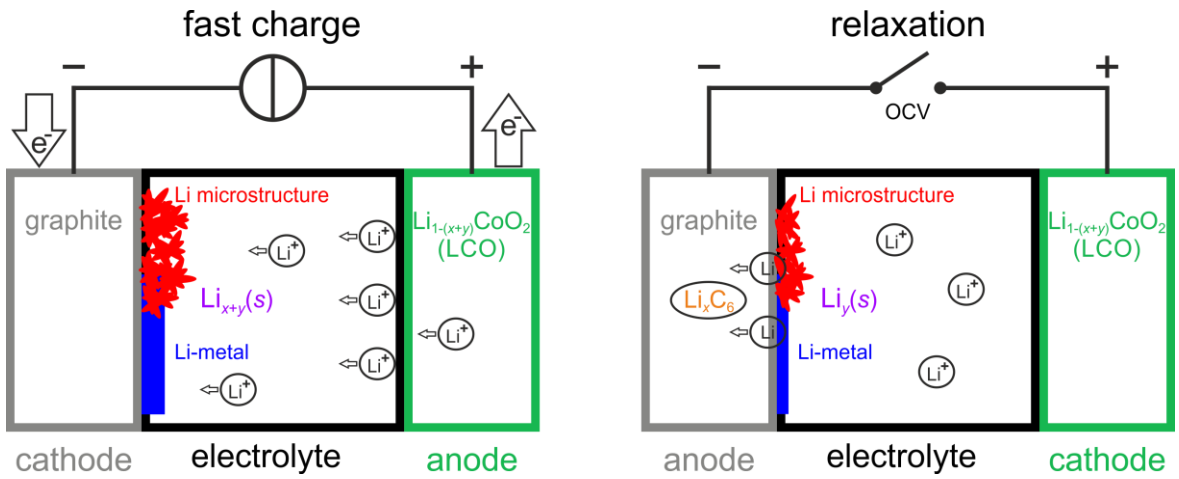

Fig. 36: Schematic drawing of transport and transformation processes in a LCO vs. graphite battery cell during and after Li plating. *As indicated by the in-operando NMR data a Li-microstructure as well as Li-metal grow upon fast charging at -20 °C. The reason is a slow Li-ion diffusion in graphite at low temperatures. During relaxation after charging the plated Li slowly diffuses into graphite. The NMR measurement revealed a faster decrease of Li-metal than Li microstructures.*

$$y\mathrm{Li}(s) + \mathrm{Li}_x\mathrm{C}_6(s) \xrightarrow{OCV} \mathrm{Li}_{x+y}\mathrm{C}_6(s)$$

with ($0 \leq x+y \leq 1$). This is schematically depicted in Fig. 36 on the right. Values of the diffusion coefficient for Li^+-ions in graphite varying over several orders of magnitude have been reported[153,154]. Analyzing the NMR signal evolutions of a particular cell could enable to estimate the diffusion coefficient under various conditions.

After around 15 h OCV, a faster decrease of the metallic Li signal integral I_{LM} than before was found and within the next 10 h I_{LM} decreased to its initial value $I_{LM,0}$ before fast charging with 10 V. In contrast to this, after around 15 h OCV the Li microstructure signal integral $I_{\mu L}$ increased by approximately 10 % within 5 h and then was constant for the last 12 h. This indicated remaining Li microstructures on the graphite electrode, which were not intercalated during 32 h OCV, as observed for metallic parts of the Li plating layer.

7. Experiments on Si-air cells

Silicon anodes for metal-air cells can be used in combination with aqueous KOH electrolytes. The low toxicity of such Si-air cells presents a major advance compared to polluting Li-ion cells. This benefit is accompanied by a corrosion of Si in KOH electrolytes, which leads to an undesired dissolution of the anode. NMR measurements of the Si corrosion products after full dissolution of Si-wafers in four aqueous electrolytes with different KOH concentrations are the topic of chapter 7.1. By dissolving different amounts of Si-wafers, 0.5 M and 1 M Si concentrations in the electrolytes were obtained.

To investigate the influence of temperature on the corrosion rate, the formation of the Si corrosion products in approximately 4 M KOH electrolyte was measured with time-resolved *in-situ* NMR (chapter 7.2). Three measurements were performed at 20 °C, 40°C as well as 60 °C, and in a fourth measurement at 60 °C a PEG electrolyte additive was used to mitigate the Si corrosion.

Finally, the developed *in-operando* container for metal-air cells was loaded with Si-wafer, air cathode and KOH electrolyte, as described in chapter 3.2.3. The attempt of following the formation of corrosion products (~95% at.) and Si products from electrochemical discharge reactions (~5% at.) with *in-operando* NMR is presented in chapter 7.3.

All aqueous KOH solutions were prepared by Dr. Yasin Emre Durmus (FZJ IEK-9).

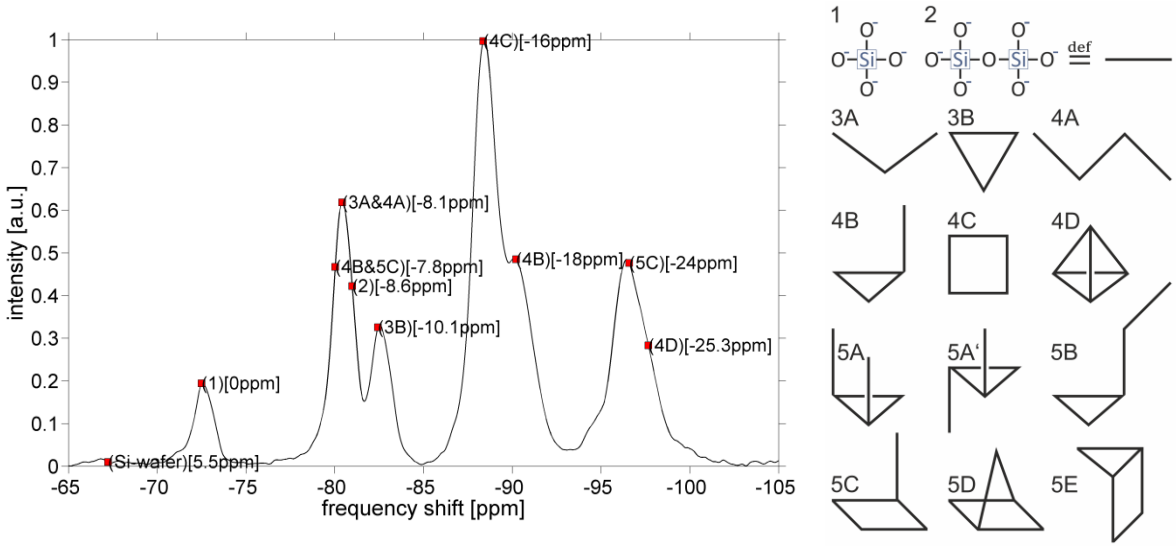

Fig. 37: ^{29}Si NMR spectrum of 4 M KOH aqueous electrolyte after dissolution of a Si-wafer anode and structural formulas of Si corrosion products. *Left: The spectrum was composed of several overlapping signals from different silicates. Based on the investigations of Knight et al.[73] different silicate structures were assigned to specific frequency shifts. In general higher negative chemical shifts can be attributed to bigger structures. The frequency shifts given in the signal labels are referred to the Si monomer at -72.3 ppm from tetramethylsilane (TMS). Right: Structures of silicates found in aqueous KOH solutions after dissolution of Si. The silicate labeled with 1 is called monomer and represents a Si atom surrounded by four oxygen atoms. In case of full deprotonation, no further hydrogen atoms are bound to the oxygen atoms, which thereby become negative. Silicate structure 2 (disilicate) consists of two Si atoms bridged via an oxygen atom. To simplify the structural formulas a straight line is used to represent this structure. Thus, the trisilicates 3A and 3B consist of three Si atoms. 3A has two oxygen bridges, whereas 3B is cyclic due to three oxygen bridges. Similar to this the tetrasilicates with four Si atoms can form chained (4A), cyclic (4C, 4D) and mixed structures (4B). In case of five or more Si atoms the silicate structures become more complex. Signals of structure 5C could be identified, but signals of larger silicates were not observed.*

7.1. Silicate compositions in aqueous KOH electrolytes

Dissolving Si in aqueous KOH solution leads to the formation of corrosion products[48]. These products exhibit different NMR frequency shifts and thus can be distinguished[73,155–160]. Exemplarily the ^{29}Si NMR spectrum of approximately 4 M KOH aqueous electrolyte after dissolution of a Si-wafer anode is shown in Fig. 37 on the left and the corresponding structural formulas are shown on the right. This identification of the corrosion products is based on high resolution ^{29}Si NMR investigations performed at 750 MHz by Knight et al.[73]. Therefor SiO_2 was dissolved in KOH solutions and the spectra were composed of more than 200 sharp signals, which in large part could be assigned to approximately 50 specific silicate structures. In Fig. 37 only fourteen of these structures are shown. The smallest corrosion product is the Si monomer (monosilicate), which is labeled with 1. Linked by oxygen atoms the Si atoms can form chained (e.g. 2, 3A, 4A), cyclic (e.g. 3B, 4C, 4D) and complex (e.g. 4B and 5) oligomeric silicates. The NMR signal with least negative chemical shift corresponds to the monomer, whereas signals with higher negative chemical shifts in general can be assigned to larger silicates. The frequency shift of a Si atom embedded in such a molecule depends on its surrounding atoms. Hence the silicates 1, 2, 3B, 4C and 4D exhibit only one resonance signal due to their symmetry. Because two different surroundings are given for the Si atoms in the silicates 3A, 4A and 5D, these structures show two signals with different frequency shifts. The more complex the silicates become, the more signals they exhibit. The biggest structure that could be identified was the pentasilicate 5C. This is why hexasilicates were not included in the analysis of this work. The silicate frequency shifts from monomer to nonasilicates can be found in the supporting information of ref. [73].

To investigate the end-state silicate composition after completed corrosion, plasma cleaned Si-wafers were fully dissolved in 1 M, 2 M, 5 M and 8 M KOH aqueous solution such that final Si concentrations of 0.5 M and 1 M were obtained. For ^{29}Si NMR measurements, the liquid samples (4 ml) were filled in PFA tubes with 15 mm diameter and stabilized to 25 °C. The spectra are shown in Fig. 38. The number of averaged FIDs for each acquired spectrum was 2504 because the signal-to-noise ratio (SNR) of ^{29}Si NMR is poor due to the low gyromagnetic ratio of 8.458 MHz T^{-1} and the low ^{29}Si abundance of 4.7 %[161]. An rf pulse delay of 20 s, a pulse length of 19 µs and a power of 150 W were used. For all corrosion products, longitudinal relaxation time constants, T_1, between 5 s and 8 s were determined with a saturation recovery experiment. Measurements with a pulse delay of 1800 s were performed as well, to search for SiO_2, which exhibits a T_1 time constant of 5 h to 8 h[162,163]. As expected for aqueous solutions with KOH concentrations of 1 M and more, no SiO_2 was found[74,75]. For crystalline Si T_1 relaxation time constants higher than 5000 s were reported[164]. Nevertheless, NMR signals of Si-wafers were visible even with a pulse delays of 10 s.

Depending on the KOH and Si concentration of the solutions the ratios of the silicate species differed significantly (Fig. 38). For high KOH concentrations (5 M, 8 M) the solutions contained more of the Si monomers, whereas along with lower KOH concentrations (1 M, 2 M) the equilibrium shifted towards longer and cyclic silicates. Another effect of an increased K^+:Si^{IV} ratio was a center frequency shift of the silicate resonances towards downfield. For example a shift of 0.5 ppm was observed for the monomer resonance when the K^+:Si^{IV} ratio was increased from 2:1 to 10:1. The reason could be a deprotonation of silicates at higher pH values, which may result in a deshielding of the hydrogen nucleus[156,158,165,166]. All KOH solutions with 1 M dissolved Si-wafers showed a stronger tendency towards oligomerization of larger silicates compared to the corresponding solutions with 0.5 M Si content. In accordance to this the viscosity of the KOH solutions increased with the amount of dissolved Si and thus, as indicated by

NMR, with an increasing concentration of longer chained silicates. As demonstrated by Durmus et al.[48] the discharge potential of Si-air cells with aqueous KOH electrolytes is influenced by the silicate composition. For more viscous solutions with a high content of long and cyclic silicates, lower discharge potential were found than for solutions with a small amount of dissolved Si. This could be due to a decreased ionic conductivity of the electrolyte resulting in a higher ohmic drop in the cell[48]. However, to enable a stable and appropriate discharge current above 0.1 mA/cm^2 of a Si-air cell with KOH electrolyte a concentration of 5 M KOH or higher is necessary[69].

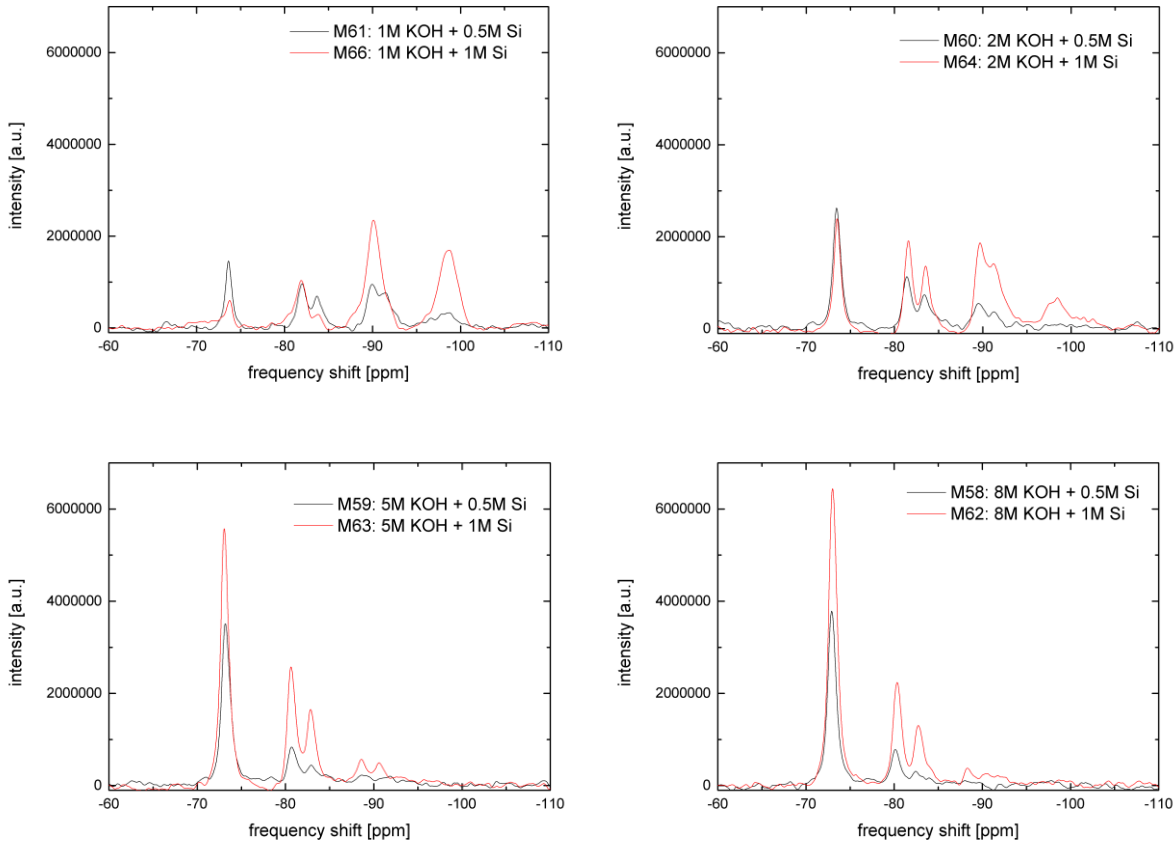

Fig. 38: ^{29}Si ex-situ NMR spectra of Si corrosion products for different KOH solutions. *The spectra were measured after complete dissolution of 0.5 M and 1 M Si-wafers in 1 M, 2 M, 5 M and 8 M KOH aqueous electrolytes. The amount of long and cyclic silicates increased with increasing Si concentration and decreasing KOH concentration. For each acquired spectrum the number of averaged FIDs was 2504. During the corrosion reactions and afterwards the solutions were stored at 25 °C. Two weeks after the NMR measurements shown in this figure, the spectra were acquired for a second time. A comparison verified no significant changes within this period and indicated stable silicate compositions in the KOH solutions.*

7.2. Time-resolved *in-situ* NMR measurements of the Si corrosion

Time-resolved ^{29}Si NMR measurements of the Si corrosion in approximately 4 M KOH electrolyte were conducted at 20°C, 40°C and 60°C to investigate the influence of temperature. After full dissolution of Si-wafers the electrolytes contained approximately 3 M Si. Three measurements were performed at 20 °C, 40°C as well as 60 °C, and in a fourth measurement at 60 °C a PEG electrolyte additive was used to test for a corrosion mitigation of the Si-wafer. After plasma cleaning the Si-wafers were partially broken to fit into 12 mm PFA tubes with electrolyte solution. The tubes were place in the HPBBHT probe such that the Si-wafer fragments at the bottom were positioned approximately 2 mm below the rf coil. The time-resolved spectra of the Si corrosion at 60 °C are shown in Fig. 39. For all four corrosion measurements an rf pulse power of 75 W, a pulse length of 29 µs and a pulse delay of 20 s was used. 600 FIDs were averaged by data post processing to generate a sufficient SNR. Hence, the temporal resolution of the spectra presented in this subchapter is 20 s · 600 / 3600 s/h ≈ 3.33 h. To our knowledge no time-resolved NMR measurements of the Si corrosion were reported so far.

The NMR acquisition was started directly after placing the Si-wafer in the 4 M KOH electrolyte. Therefore the first spectra showed a signal of the Si-wafer centered at approximately -66 ppm (Fig. 39). At 60 C this signal vanished within around 30 h due to the dissolution of the wafer. Along with this, growing silicate signals were observed. The evolutions of the different signals are shown in Fig. 40 for 60 °C with and without PEG corrosion inhibitor as well as in Fig. 41 for 40 °C and 20 C both without inhibitor. A direct comparison of the signal evolutions in the four experiments is shown in Fig. 42

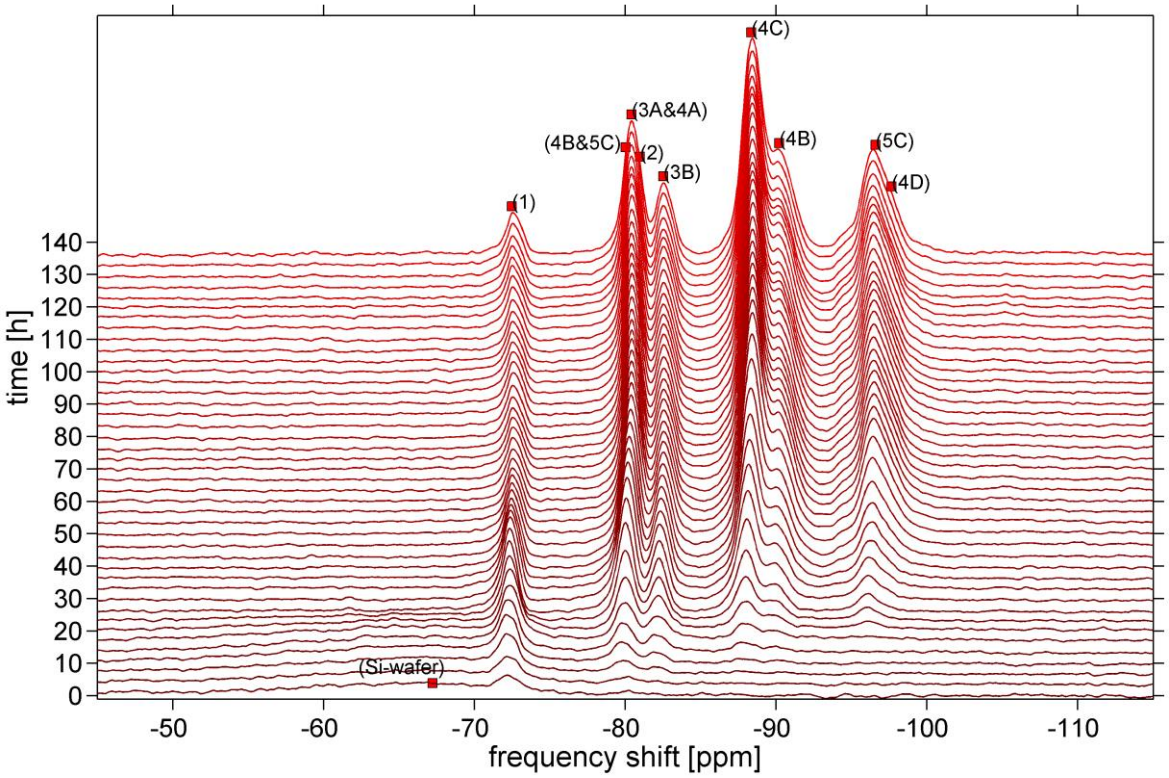

Fig. 39: Time-resolved in-situ ^{29}Si NMR spectra of the silicate formation during corrosion of a Si-wafer in 4 M KOH aqueous electrolyte at 60 °C. *In the first acquired spectra a Si-wafer signal at approximately -66 ppm and already a small amount of monomers (1) at approximately -72.3 ppm were visible. Along with the dissolution and thereby signal decrease of the Si-wafer, the signals of corrosion products increased. Long and cyclic silicates, e.g. tetra- (4B,C,D) and pentasilicates (5C) were formed later than smaller Si structures (1, 2, 3A,B). The intensity evolutions of the different signals are shown in Fig. 40. The temporal resolution of the spectra is 3.33 h.*

separately for each Si structure. The temperature variations in the laboratory between day and night caused oscillations of the NMR intensities. Because the measurements without inhibitor were interrupted once in between for re-adjustment of the resonant circuit, these oscillations were interrupted one-time and then continued phase shifted. The contribution, which was affecting the spectra baselines was decreased by baseline corrections separately of each spectrum. A remaining contribution led to 24 h intensity oscillations most obviously visible for the silicates 4D and 5C (Fig. 42). Most likely the reason was a change of the tuning and matching alignment of the resonant circuit. This could happen due to tuning and matching adjustment mechanics, which are in contact to the non-stabilized laboratory air. Moreover, the measurements were performed at an early stage of this work at which a probe frame tempering was not yet available.

Before the Si-wafer signal I_{Si} decreased due to extensive dissolution, it increased for around 15 h in case of 60 °C, for around 30 h at 40 °C and for approximately 65 h at 20 °C. The reason could be the etching of the Si-wafer[74,75], which started directly after the first contact of wafer and KOH electrolyte. This could change the surface to volume ratio and the surface impedance, and thus could led to susceptibility

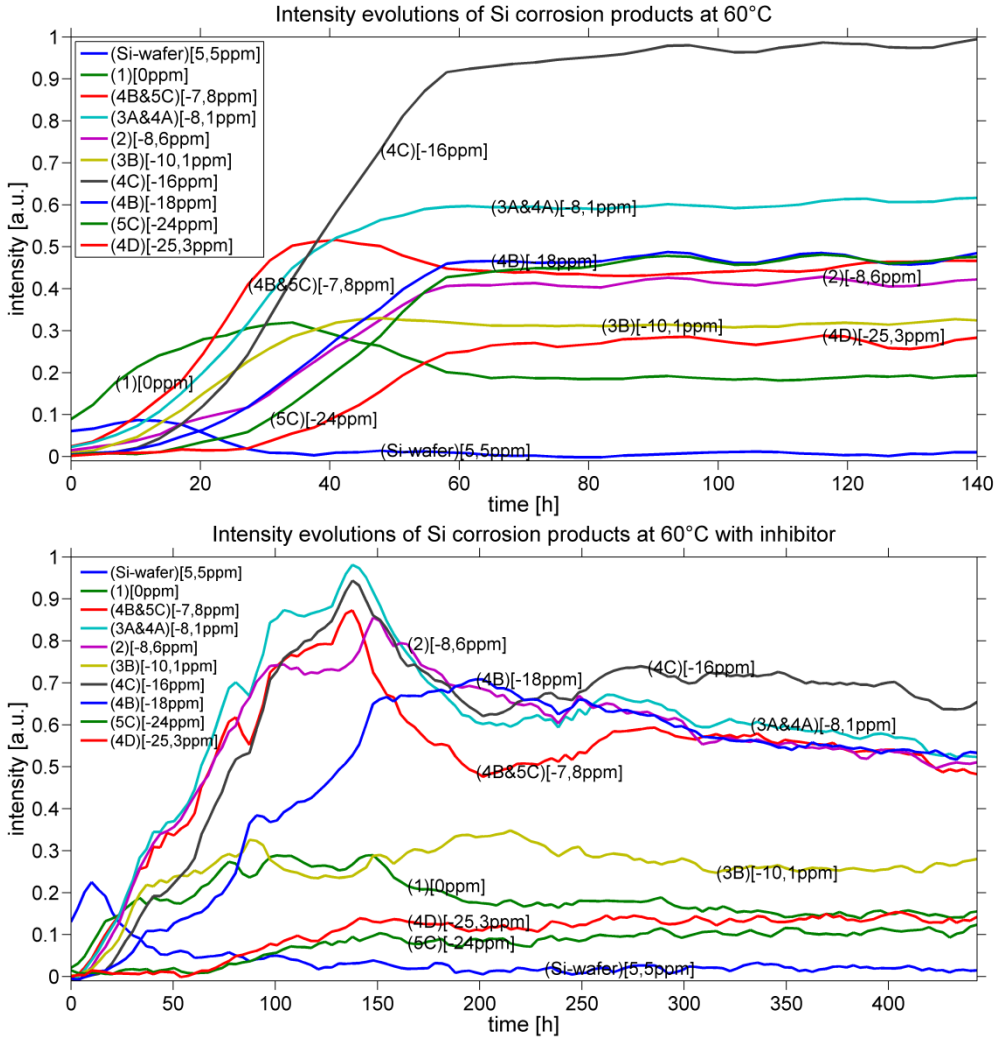

Fig. 40: Time-resolved ^{29}Si in-situ NMR intensity evolutions at 60 °C during corrosion of 3 M Si-wafers in 4 M KOH aqueous electrolytes with and without corrosion inhibitor. *Top panel: At 60 °C without corrosion inhibitor the silicate composition reached a steady equilibrium after approximately 60 h. The measurement was interrupted for re-alignment of the resonant circuit after 56 h. Bottom panel: At 60 °C with PEG inhibitor the signal of the Si-wafer decreased slower and the silicate composition reached a steady equilibrium after approximately 320 h. The resonant circuit was not re-aligned in the NMR measurement with inhibitor. The spectra were normalized for a maximum intensity equal to 1.*

changes. The maximum signal intensity of I_{Si} in the four measurements varied strongly (Fig. 42). Most probably this was because not only one but a few broken Si-wafer pieces were used for the experiments. These pieces had different sizes and moved during the NMR measurements due to the hydrogen evolution (see chapter 2.1.2). Moreover, a lifting of small wafer fragments by hydrogen bubbles such that parts of the wafer were attached to the tube wall inside the rf coil was observed as well. These motions of metallic parts resulted in susceptibility changes and disturbances of the NMR signals.

Using no corrosion inhibitor the Si-wafer intensity I_{Si} decreased the faster the higher the temperature was (Fig. 42). Comparing the decrease of I_{Si} in the measurement with corrosion inhibitor with the three other measurements indicated a mitigation of the corrosion. The dissolution of the Si-wafer at 60 °C with inhibitor lasted for around 200 h and thereby was similar to the dissolution at 20 °C. On the other hand, the decrease of I_{Si} started much earlier at 60 °C with inhibitor than at 20 °C and the onset of the decrease was comparable to the decrease of I_{Si} at 60 °C without inhibitor.

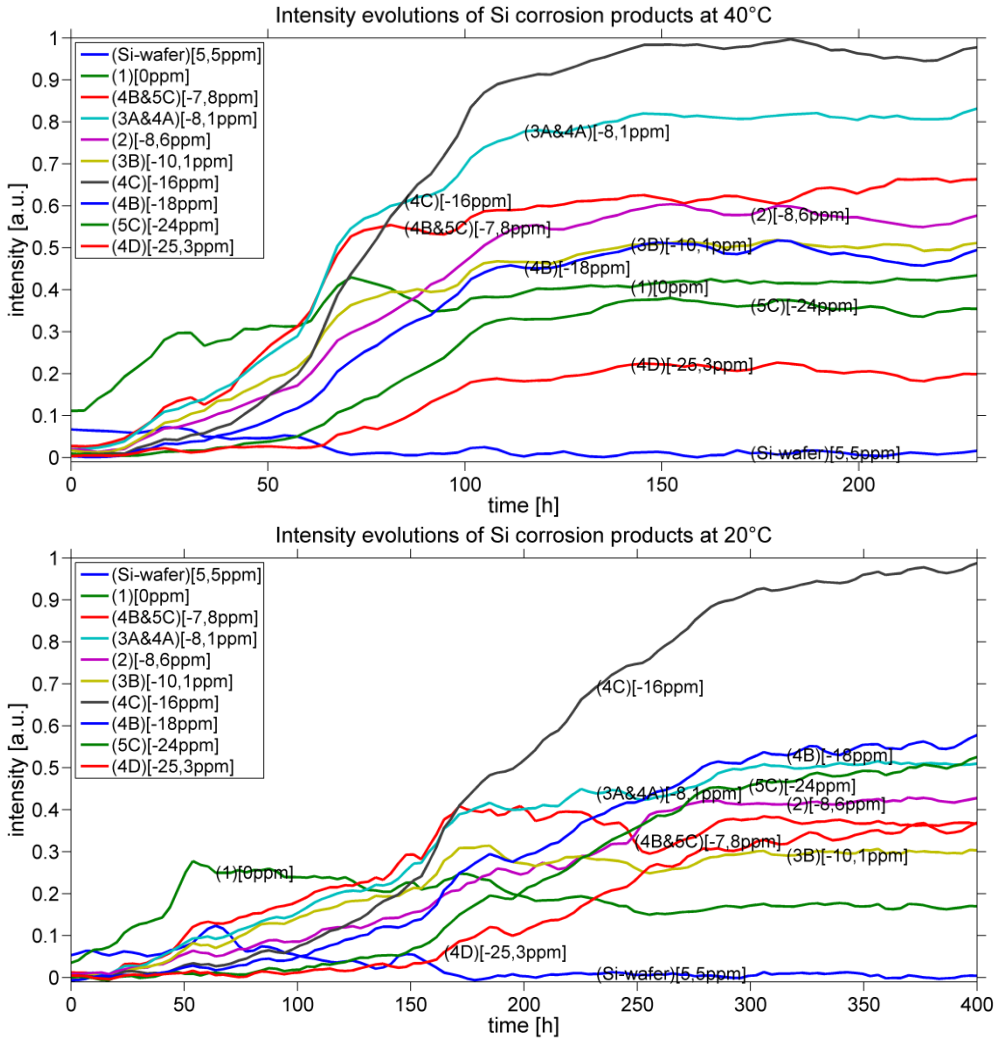

Fig. 41: Time-resolved ^{29}Si in-situ NMR intensity evolutions at 40 °C and 20 °C during corrosion of 3 M Si-wafers in 4 M KOH aqueous electrolytes without inhibitor. *Top panel: At 40 °C the silicate composition reached a steady equilibrium after approximately 150 h. The Si-wafer signal decrease and the silicate formation were slower at 40 °C than at 60 °C (Fig. 40). The measurement was interrupted for re-alignment of the resonant circuit after 165 h. Bottom panel: At 20 °C the signal of the Si-wafer decreased slower than at 40 °C and the silicate composition reached a steady equilibrium after approximately 320 h. The measurement was interrupted for re-alignment of the resonant circuit after 333 h. The spectra were normalized for a maximum intensity equal to 1.*

In all experiments the signal of the Si monomers $I_{(1)}$ appeared first and was already slightly visible in the first spectra. At 60 °C and without using an inhibitor, $I_{(1)}$ reached its maximum value after approximately 35 h (Fig. 40 top), whereas with inhibitor $I_{(1)}$ increased much slower and for around 100 h

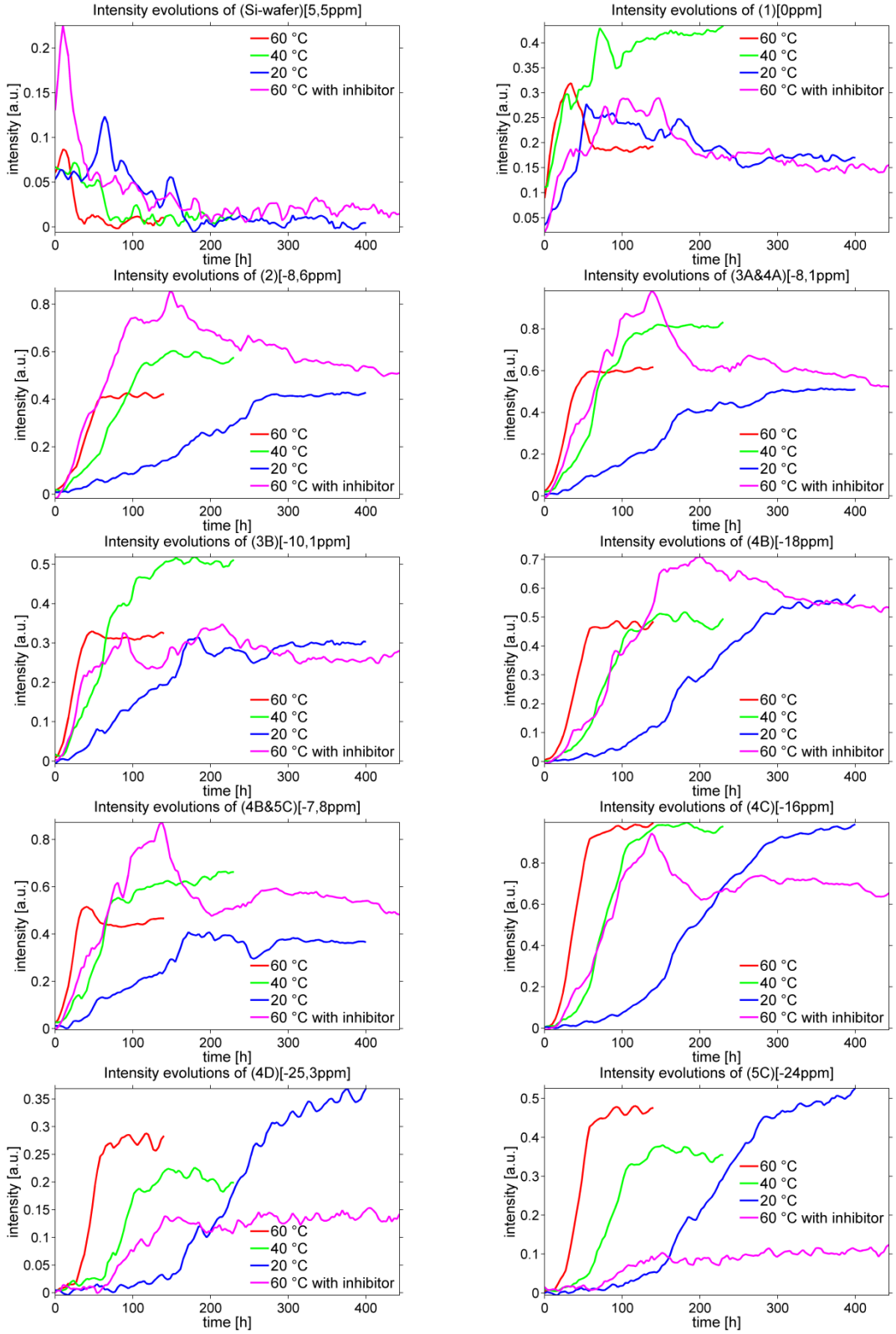

Fig. 42: Comparison of ^{29}Si intensity evolutions during Si-wafer corrosion at 60 °C, 40 °C and 20 °C. *At 60 °C two measurements with and without PEG corrosion inhibitor were performed. Without inhibitor the Si-wafer NMR intensity decreased the faster, the higher the temperature was. Along with this the intensities of all silicates increased faster for elevated temperatures. Using the inhibitor mitigated the formation rate of all silicates aside from the disilicate (2). Large silicates like 4D and 5C were affected most.*

(Fig. 40 bottom). At 40 °C, $I_{(1)}$ increased for around 70 h and faster than for a temperature of 20 °C, at which, however, $I_{(1)}$ increased for around 55 h. Thus, $I_{(1)}$ increased the faster the higher the temperature was. This indicated an enhanced corrosion rate at more elevated temperatures and is in accordance to a faster Si-wafer intensity decrease for higher temperatures. Remarkably, the monomer signal evolution at 60 °C using the corrosion inhibitor was almost comparable to the evolution at 20 °C without inhibitor. Another effect of temperature, which was more pronounced in the experiments at 60 °C, was an overshooting of $I_{(1)}$. Because a decrease of $I_{(1)}$ can be attributed to a lowering of the monomer concentration, this indicated a subsequent reaction of monomers to larger silicates. A reaction pathway was suggested by Kinrade et al. and an illustration can be found in ref.[167]. Following this pathway, the silicate growth could proceed by electrophilic attacks of monomers on the negative oxygen ligands of the various Si structures. For example, two monomers could form the disilicate (2), the reaction of a monomer and a disilicate (2) could form the trisilicate 3B and the tetrasilicate 4B could be caused by the reaction of a monomer with the trisilicate 3B.

Comparing the evolutions of the larger silicates (2) to (5C) for the three measurements without inhibitor showed for all of these structures a faster growth the higher the temperature. Taking the measurement with inhibitor at 60 °C into account, only the formation rate of the disilicate was not decreased. The trisilicates increased faster than at 40 °C but slower than at 60 °C without inhibitor. The tetrasilicate formation rate was almost similar to the rate at 40 °C and the pentasilicate signal increased almost as slow as at 20 °C. Moreover the end state intensities of the 4C, 4D and 5C silicate signals were lower than in the measurements without inhibitor. Thus, the inhibitor mitigated the corrosion and shifted the equilibrium towards small disilicates. This might be favorable in terms of low viscosity and accordingly high ionic conductivity[48]. PEG di-acid is known to covalently couple to Si via C–O bonds, as shown e.g. by X-ray photoelectron spectroscopy (XPS) investigations[168] and thereby can encapsulate a variety of molecules[169,170] as well as Si-based microdevices[171–173] and Si nanoparticles[174,175]. It was successfully used to mitigate the corrosion in metal-air cells with Al anodes[78,81,82,176,177] as well as with Zn anodes[79,83] and can be used to prevent iron corrosion in water[80]. Hydrophobic PEG layers and films on the surface of Si-wafers were studied in detail as well[178–182]. Moreover PEG led to a suppression of dendrite growth on Zn anodes[84,183] and was tested in cells with Li-metal[122,184]. It can form self-assembled monolayers, which can be stable up to 120 °C[185]. Other possibilities to mitigate the corrosion of Si anodes are for example hydrogen-terminating and alkyltrichlorosilane-based self-assembled monolayer coatings[186]. Moreover, non-aqueous electrolytes like ionic liquids exhibiting a lower corrosion rate can be used[187].

Another effect observed in case of using the PEG inhibitor was an overshooting of all silicate signal intensities, the least pronounced for the large silicates 4D and 5C. Increasing signals, which could compensate the decreasing signals after overshooting, were not observed. The reason could be a SiO_2 formation, which could be stabilized by PEG[188] and would not have been detected by NMR due to the long T_1 relaxation time constant of SiO_2.

The end state silicate composition of the measurement at 60 °C without inhibitor, shown in the last spectrum of Fig. 39, is similar to the composition of 1 M KOH solution after dissolution of 1 M Si (Fig. 38). Taking the uncertainty of the KOH content during sample preparation into account (basis with ≥85 % KOH), this is in agreement with the findings described in chapter 7.1 for electrolyte solutions with a K^+:Si^{IV} ratio close to 1:1. The end state silicate composition in the measurement at 20 °C was similar to the one at 60 °C, whereas the end state at 40 °C indicated a higher concentration of smaller

silicates. The reason was most likely an approximately 10 % smaller amount of dissolved Si-wafer in the 40 °C experiment (for details see chapter 3.4.2) such that the K^+:Si^{IV} ratio was changed. This is in agreement with the findings of chapter 7.1 as well.

7.3. *In-operando* NMR measurements of Si-air cells

To test the discharge performance of the developed *in-operando* metal-air battery setup, a cell container was loaded with a Si-wafer anode, an air cathode and aqueous 5 M KOH electrolyte, as described in chapter 3.2.3. The pump reservoir initially contained 3 ml electrolyte and 1 ml remained after starting the flow such that the capillary tubes and the cell container were filled. The discharge profile of this cell, numbered with 12 and thereby continuing the numbering of the previous chapters, is shown in Fig. 43 on the left. Cell 12 was tested outside the NMR at 25 °C and with continuous electrolyte flow but without gas supply.

5 h after starting the electrolyte flow the discharge of cell 12 was started with a current density of 0.026 mA/cm^2 (10 µA). During the first 4 h the cell voltage decreased from approximately 1.15 V to 1.0 V. For around 15 h the voltage was almost constant and above 1 V. Then the pump rate of the electrolyte supply was reduced from approximately 1 ml/min to around 0.01 ml/min. Hereon a decrease of the cell voltage was observed and the evolution of hydrogen caused disturbances of the cell voltage. Most likely the low flow rate was not sufficient to remove enough hydrogen and bubbles blocked the air cathode. After 30 h discharging (15 h with low pump rate) and a decrease down to 0.88 V the electrolyte pump rate was increased again for a flow rate of 1 ml/min. This resulted in a recovery of the cell voltage. Another 12 h later, after approximately 42 h discharging, a voltage of 1.0 V was measured. Then the pump was switched off, the cell voltage decreased again and a few hours later first cell voltage disturbances occurred. These voltage breakdowns became more frequently and after 50 h the discharge was stopped. Most likely the accumulation of hydrogen at the air cathode led to interruptions of the ionic conductivity. By disassembling the cell, the Si-wafer anode was removed. On its surface the dissolution by the KOH electrolyte was clearly visible and an almost homogeneous etching depth of approximately 0.3 mm was found.

The Si-air cell 13 was assembled for ^{29}Si *in-operando* NMR measurements. The probe temperature was stabilized to 25 °C. Electrolyte flow (different rates, 5 M KOH solution) and synthetic air supply (10 ml/min) were used. This enabled almost the complete consumption of the Si-wafer anode before the battery current flow ended (see photograph in Fig. 44). To our knowledge thereby the first well

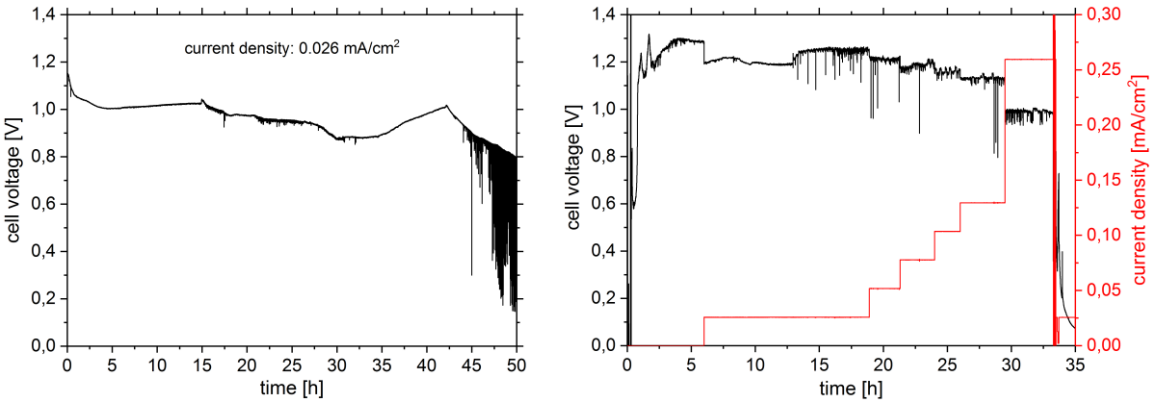

Fig. 43: Discharge current/voltage profiles of Si-air cell 12 (outside NMR) and cell 13 (inside NMR). *Left: Si-air cell 12 was discharged outside the NMR for a first testing. Electrolyte flow but no gas supply were used. The electrolyte pump rate was decreased after 15 h, then increased again after 30 h and finally switched off after 42 h. Right: The discharge of Si-air cell 13 was performed in the NMR and with electrolyte and gas supply. The current density was increased up to 260 µA/cm². A higher discharge current caused a breakdown of the cell voltage. In the acquired in-operando NMR spectra no silicate signals were visible and thus they are not shown for this discharge test. The next discharge test of cell 13 during in-operando NMR measurements is shown in Fig. 44.*

performing setup for NMR investigations of metal-air battery cells was realized. Beforehand, the pulse parameters were optimized by pumping TMS through the cell container and the B_0 homogeneity was increased by shimming with a flow of 1M LiCl solution. A minimum ^{7}Li FWHM of approximately 50 Hz (≈ 0.63 ppm) was reached, which is one order of magnitude higher than for the Li-ion *in-operando* container. The reason could be susceptibility effects of the Si-wafer and the thin-film gold coating, which was deposited on roughly half of the separator ring of the metal-air container (chapter 3.2.2). To improve the spectral resolution this coating may be decreased in size and the metal anode might be positioned below the coil.

The current/voltage profile of the first discharge test of cell 13 is shown in Fig. 43 on the right. After 6 h OCV the discharge current was increased stepwise up to 0.26 mA/cm^2 (0.1 mA). Along with this the cell voltage decreased with each current enhancement. Further increasing the current led to a voltage breakdown. An electrolyte flow of 2 ml/min was used. Because silicate NMR signals were not observed during this discharge, the first electrochemical measurement is presented without *in-operando* spectra.

The second discharge test of Si-air cell 13 during *in-operando* NMR measurements was performed after full recovery of the OCV. About 2 h after the stepwise increase of the current up to 0.26 mA/cm^2 the electrolyte pump rate was reduced to approximately 0.01 ml/min. Therefore the cell voltage was not stable using this high current density and decreased (Fig. 44 on the left). Even for smaller discharge currents of 0.23 mA/cm^2 and 0.13 mA/cm^2, which were tested after around 5 h of discharging, an ongoing voltage decrease was observed. Thus, after roughly 7 h the electrolyte pump rate was increased

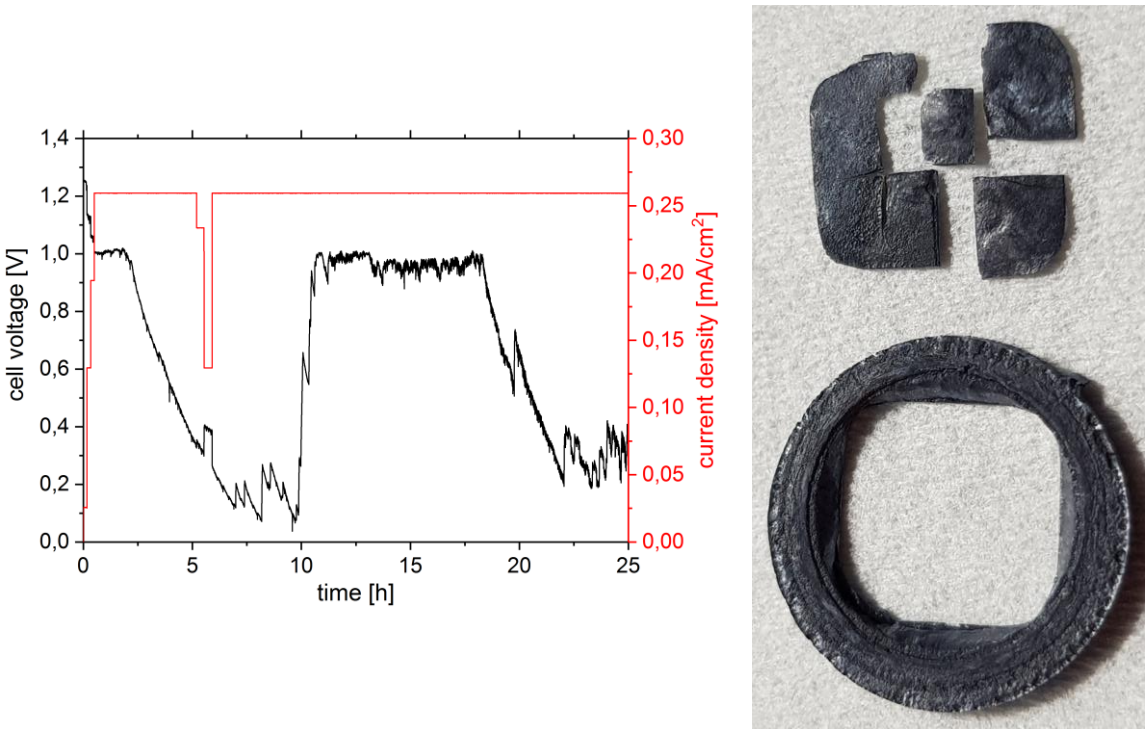

Fig. 44: Second discharge current/voltage profile of Si-air cell 13 during in-operando NMR and photograph of the Si-wafer anode after discharging. *<u>Left</u>: The second discharge test of cell 13 was performed after complete recovery of the cell voltage, which broke down at the end of the first test (Fig. 43). After decreasing the electrolyte flow rate to approximately 0.01 ml the cell voltage decreased. By increasing the flow rate stepwise a discharge voltage of around 1 V for a flow rate of approximately 0.5 ml/min was found. The corresponding in-operando ^{29}Si NMR measurement is shown in Fig. 45. <u>Right</u>: The photograph shows the Si-wafer anode after the end of discharging for cell 13. The (almost rectangular) parts, shown at the top, were such thin that they broke apart from the remaining Si-wafer, shown at the bottom. Thereby the active surface of the Si-wafer surface changed and strong fluctuations of the cell voltage were observed in the last 5 h of discharging.*

step-by-step. Thereby flow rates of approximately 0.03, 0.05, 0.1, 0.125, 0.15 and 0.3 ml/min were tested first. Nevertheless, that the voltage increased with each flow rate enhancement, the continuous decrease of the voltage was not stopped with these low flow rates. Thus, the flow rate was increased to 0.5 ml/min and a cell voltage of around 1 V was obtained. This electrolyte flow and thereby the cell voltage were kept constant for around 8 h. Then, a second time the flow rate was decreased to approximately 0.01 ml/min and hence the voltage dropped. This voltage decrease was not stopped after 20 h of discharging by a flow rate increase to 0.5 ml/min and also not by an increase to 1 ml/min after 22 h. Neither without discharging the voltage recovered. After disassembling cell 13 its Si-wafer anode was found broken (photograph in Fig. 44). A Si-wafer ring and a thin plate, which broke off from the middle of the ring, were left. In total approximately 0.042 g Si-wafer were dissolved in the electrolyte. This was by a factor of around 9 less than in the *in-situ* measurements (chapter 7.2) and resulted in a Si concentration of 0.5 M at the end of discharging.

In this second test of cell 13 the discharge current was not decreased to generate as much as possible Si products from the electrochemical discharge. In general, without inhibitor around 20 times more Si reacts due to corrosion than due to electrochemical oxidation[48]. Thereby the mass loss is around 95 % and higher currents shift this value more towards oxidation products. These silicates from discharge may lead to a different silicate composition than found in pure corrosion NMR experiments (chapter 7.1 and 7.2).

The *in-operando* ^{29}Si NMR measurement of cell 13 during the second discharge test is shown in Fig. 45. An rf pulse power of 300 W, a pulse length of 9 µs and a pulse delay of 10 s were used. The SNR was such low that 3440 spectra were averaged resulting in a temporal resolution of roughly 9.6 h. The spectra contained a strong signal of the Si-wafer anode with a frequency shift of only approximately 3.5 ppm referred to the Si monomer. Compared to the time-resolved *in-situ* measurements (chapter 7.2) the Si

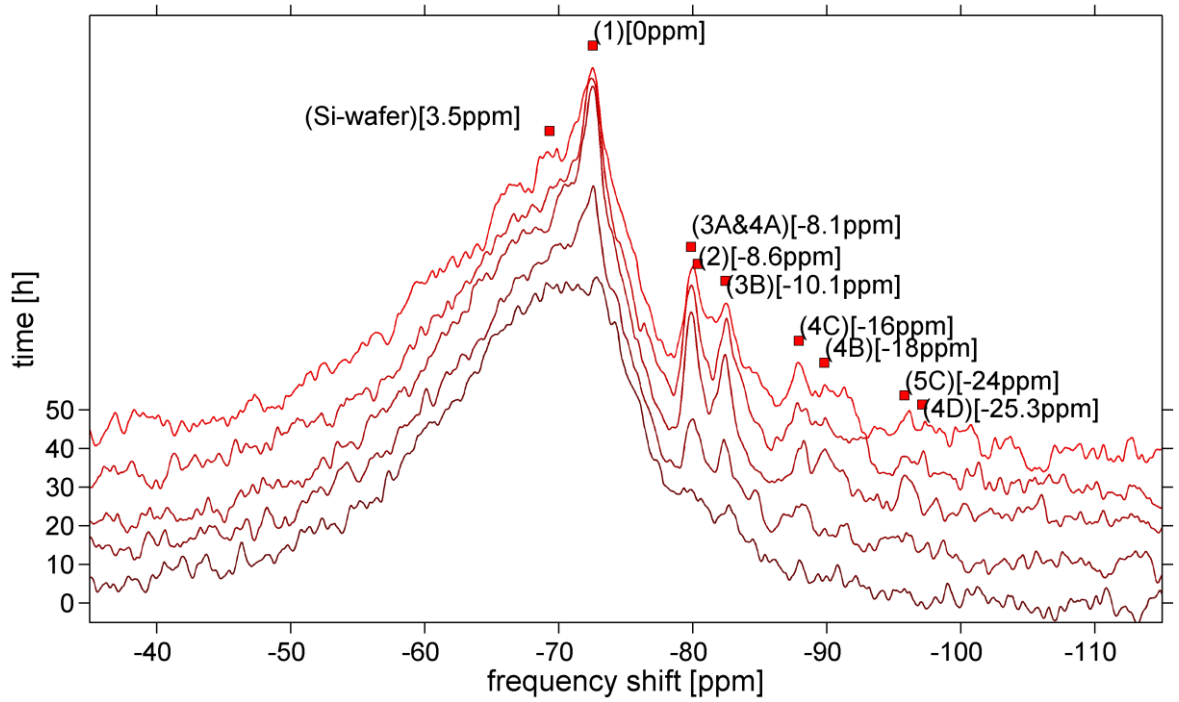

Fig. 45: ^{29}Si in-operando NMR measurement of Si-air cell 13. *Silicate signals were slightly visible at the beginning of the second discharge test of cell 13. These signals grew upon discharging and overlapped with a strong and broad signal of the Si-wafer. A higher amount of Si monomers than of long and cyclic silicates was observed. A low temporal resolution of roughly 9.6 h was chosen for a sufficient SNR. The discharge current/voltage profile is shown in Fig. 44*

wafer signal was much more intense, because during *in-operando* measurements the wafer was positioned in the rf coil at the lower edge. In the *in-situ* measurement the Si-wafer fragments were placed approximately 2 mm below the rf coil in a tube. Disassembling cell 13 showed remaining Si-wafer parts after the end of discharge (photograph in Fig. 44). Therefore the NMR signal of the wafer did not vanish in the *in-operando* measurement (Fig. 45), but a broadening of the Si-wafer signal line shape was observed in the last spectrum. The reason for this change of the line shape could be broken Si-wafer parts, which fall off the anode. These parts could move due to the hydrogen evolution and thereby turn their orientation with respect to the B_0 field.

Signals of Si corrosion products were slightly visible in the first NMR spectrum of the second discharge test and overlapped with the strong signals of the Si wafer (Fig. 45). An increase of these silicate signals was observed in the next spectra. The Si monomer (1) intensity increased during the first 30 h and then slightly decreased. This could be assigned to the overshooting effect, which was observed for the monomer in all *in-situ* measurements (chapter 7.2). Along with this the intensity of disilicates (2) and trisilicates (3A, 3B) increased significantly during the first 30 h and then was almost constant. The signals of the larger tetrasilicates (4B,C,D) and the pentasilicate (5C) grew during the entire *in-operando* NMR measurement. After nearly 48 h the NMR acquisition was stopped, because discharging with a stable cell voltage was no longer possible roughly 24 h after the acquisition and the second discharge test were started (Fig. 44). The silicate composition shown in the last spectrum of the *in-operando* measurement was most similar to the end state composition found for a K^+:Si^{IV} ratio of 4:1 (chapter 7.1). Calculating this ratio for the 3 ml of 5 M KOH electrolyte of Si-air cell 13 by taking the amount of dissolved Si-wafer (0.042 g) into account, gave a K^+:Si^{IV} equal to approximately 10:1. For such a ratio a higher concentration of Si monomers compared to long and cyclic silicates was expected. It is tempting to speculate that the electrochemical discharge could cause this effect, but the SNR of the measurement was too low for a detailed interpretation of the spectra.

Nevertheless, Si corrosion in different electrolytes may be measured time-resolved or even *in-operando* such that reaction constants and reaction pathways under different conditions might be determined by solving kinetic equations[167]. This could help to identify possible mitigations to reduce corrosion reactions in Si-air and many other metal-air batteries. The development of a rectangular cell container prototype, which could increase the filling factor of the rf coil an thereby the SNR, is presented in the appendix 12.1.

8. Conclusion & outlook*

For long-run *in-operando* NMR measurements a cylindrical NMR battery cell container was developed (chapter 3.2). A reliable cycling behavior and the long-time gas-tight sealing of the container design were demonstrated by current rate capability tests and charge–discharge cycles for more than 3000 h (chapter 4.3 and 4.4). The container was placed in a custom 3D-printed mount with a numerically optimized saddle coil, fixed on a commercial NMR probe (chapter 3.3). A comparison of numerically estimated with experimental spin nutation curves demonstrated a good agreement of experiment and simulation (chapter 4.2).

Thin-film conductive coatings with thicknesses below the skin depth of the rf pulses were used for contacting the electrodes (chapter 4.1). Thereby the amount of metal inside the cell container is minimized and a variety of electrode connection designs become possible. This thin-film contacting technique was patent-registered[3]. For the presented metal-air cell container the thin-film contacting is indispensable (chapter 3.2.3), while for the Li-ion cell design the thin-film contacting sticks can be substituted by full metal sticks (chapter 3.2.2). To decrease screening of the rf pulses in the Li-ion cell container, in future thin-film contacting could be used to produce plastic carriers with conductive coatings for Li-ion electrode materials instead of attaching the electrode materials on copper or aluminum foils (in general around 20 µm thickness). Moreover the thin-film contacting could enable reducing disturbances of the magnetic field and minimizing artifacts in imaging applications.

To demonstrate the performance of *in-operando* NMR the formation of microstructured Li on Li-metal electrodes was investigated (chapter 5 and 6.1). Gradual morphology or density change of the microstructured Li between charged and discharged state of the cell most likely caused a state-of-charge dependent frequency shift[19]. Even after 1000 h a quite continuous growth of 'dead Li' was measured, which indicates that the same amount of Li is irreversibly deposited per cycle for a given C-rate in a particular cell[47]. These findings indicate that when using a long-term stable cell, *in-operando* NMR is a suitable tool to characterize the complex dependence of the microstructure morphology, the thickness of the porous Li layer as well as enhanced current densities on the cell performance and aging[53,58,109–111]. This might help to identify successful dendrite mitigation strategies, such as enhanced cell pressure, additives or different load profiles. However, since dendrite formation is not necessarily uniform inside a cell (as seen in Fig. 25), further investigations are necessary to assess whether it is possible to predict the state-of-health or the lifetime of a cell by extrapolation from a short *in-operando* NMR run. In addition, non-uniform dendrite formation has the effect that the presented approach is only semi-quantitative, since the skin effect may lead to an individual variation of the B_1 distributions inside each cell. Also, a changing Li morphology during cycling induces temporally changing shielding of certain parts of the cell and could alter its rf impedance, which would influence the signal amplitude. Hence careful referencing is indispensable for quantitative applications. To face this issue two new versions of the *in-operando* container for Li-ion cells were prepared on paper (appendix 12.2 and 12.3). One of it in combination with plastic inserts and thin-film contacting also opens up the possibility for an integration of a third reference electrode into the container.

After NMR investigations of the Li microstructure formation in a Li-metal vs. graphite cell, *in-situ* EIS measurements inside the NMR were performed (chapter 4.5). The correlative analysis by *in-operando* NMR and high-resolution EIS yields the potential to unambiguously identify processes relevant for the electrochemical impedance response of a battery. EIS is much more sensitive to processes on the surface

*****Adapted from Kayser et al.*[1,2]

of a material than NMR. Therefore, other processes such as the formation of surface films on the graphite electrode[114], which may not be observable by NMR, need to be considered as well in a quantitative description of the ion mobility in a battery cell. This will require a more detailed comparison of EIS and NMR data at more SOC values and possibly the incorporation of additional, complementary methods[189] that are also sensitive to lithium ion dynamics.

The high reversibility of the electrochemical processes in LCO vs. graphite cells can enabled long battery lifetimes (chapter 4.4) and a Li microstructure formation did not occur under moderate cycling conditions *i.e.* C-rates below 1C and temperatures above 0 °C (chapter 6.2). Using cell potentials above 4.2 V (vs. the Li/Li^+ redox potential) led to an increased capacity degradation. In-operando NMR measurements indicated non-reversible LCO phase transformations depending on the upper cutoff voltage. Such NMR investigations might be used to determine appropriate battery cycling parameters.

For many applications fast charging is beneficial, but the lower the temperature the more the diffusion of Li into graphite slows down. This can lead to the formation of metallic and microstructured Li on the graphite electrode and thereby limits the maximum charging rate. In-operando NMR measurements can follow this Li plating process and thus could enable a determination of possible low-temperature cell capabilities (chapter 6.3). Moreover, the decrease rates of the different ^{7}Li signals indicated a faster diffusion into graphite for metallic Li than for microstructured Li. By analyzing the NMR signal evolutions of a particular cell it could become possible to estimate under various conditions the diffusion coefficients for which values over several orders of magnitude have been reported[153,154].

The rf pulse skin depth played an important role in the observed ^{7}Li NMR signal evolutions. For a more detailed understanding it would be necessary to correlate the NMR signal with the skin depth. For the future, *in-operando* NMR measurements at different magnetic fields (in particular low fields), which changes the skin depth and allows to distinguish between conductivity induced and paramagnetic effects, could be performed.

To improve the reliability of *in-operando* NMR measurements at low temperatures, tuning and matching of the resonant circuit might be performed stroboscopically. Thereby changes of the circuit resonance adjustment, which lead to NMR intensity variations, could be corrected. A tuning and matching automatization becomes easy by the use of an robot[20,135]. Moreover, the low temperature long-time capability is a crucial issue. The most comfortable equipment for gas cooling is an electric refrigerator, which easily can enable -50 °C for weeks and longer. For this work cooling was performed with a circulating cooler bottle, which runs out of liquid nitrogen after around 20 h.

Si-air battery cells with aqueous KOH electrolytes are promising new battery systems for a post-lithium era and the low toxicity of these cells presents a major advance compared to polluting Li-ion cells. However, this benefit is accompanied by a corrosion of Si in KOH electrolytes, which leads to an undesired dissolution of the Si anode (chapter 7). ^{29}Si NMR measurements were performed to reveal the composition of the Si corrosion products after dissolution of two different amounts of Si-wafers in aqueous electrolytes with four different KOH concentrations (chapter 7.1). For high K^+:Si^{IV} ratios the solutions contained more Si monomers, whereas along with lower K^+:Si^{IV} ratios the equilibrium shifted towards longer and cyclic silicates. In accordance to this the viscosity of the KOH solutions increased with the amount of dissolved Si and thus with an increasing concentration of longer chained silicates. Relating to Si-air cells with aqueous KOH electrolytes the discharge potential is influenced by the silicate composition. For more viscous solutions lower discharge potential were found than for solutions with a small amount of dissolved Si[48,70].

To investigate the influence of temperature on the Si corrosion rate, the formation of silicates in 4 M KOH electrolyte was measured with time-resolved *in-situ* NMR (chapter 7.2). Three measurements at 20 °C, 40°C and 60 °C revealed a faster corrosion for higher temperatures. Moreover, in a fourth measurement at 60 °C it became possible to mitigate the Si corrosion by using a PEG electrolyte additive. Thereby it was demonstrated that time-resolved NMR can be used to identify possible corrosion mitigation strategies for the development of long-lasting Si-air batteries.

Finally, the discharge capabilities of Si-air cells in the developed *in-operando* NMR container for metal-air batteries were investigated (chapter 7.3). Current densities up to 0.26 mA/cm^2 (0.1 mA) and almost the entire consumption of the Si-wafer anode were possible. Moreover, the growth of Si corrosion products was observed in an *in-operando* NMR measurement during discharging. Nevertheless, a low SNR in this measurement indicated the need for further improvement of the metal-air cell container such that a distinct differentiation between corrosion products and Si products from electrochemical discharge reactions becomes possible. Therefor a rectangular cell container prototype, which could increase the filling factor of the rf coil an thereby the SNR was developed and is presented in the appendix 12.1.

Several extensions of the *in-operando* NMR setup developed during this work are possible. One is a mechanical system, which moves the *in-operando* probe inside the superconducting NMR magnet. A prototype is shown in Fig. 46. The displacement of the cell in the stray field of the NMR magnet can be controlled with micrometer precision. Due to the high magnetic field gradient this enables to excite thin layers and a special resolution in direction of the B_0 field of approximately 15 µm becomes possible[42,43]. For e.g. a 19.6 T magnet a fringe field gradient strength of 72 T/m was reported[42]. This is nearly

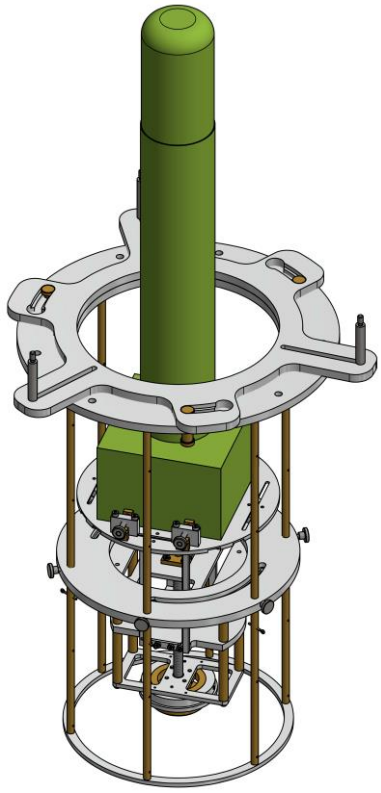

Fig. 46: CAD drawing of a stray field system for 1D high resolution battery imaging. *Using a mechanical system to move the in-operando probe (green) inside the superconducting NMR magnet the cell can be excited in the stray field. Due to the high magnetic field gradient this enables to excite thin layers and a spatial resolution in direction of the B_0 field of approximately 15 µm becomes possible[42,43]. Thereby processes at the anode can be distinguished from processes in the separator or at the cathode. The CAD drawing was constructed by Christian Hellenbrandt (FZJ IEK-9).*

50 times stronger than provided by commercial microimagers[45]. Along with this, processes at the anode can be distinguished from processes in the separator or at the cathode. In case of porous electrodes an observation of transport and transformation processes inside the materials might be possible.

Another extension of the *in-operando* NMR setup can be a frequency filter for the rf signal cable of the probe. This filter could be a band-pass such that signals close to the rf frequency are transmitted and other signal like noise are attenuated. Moreover, the filtering of the battery cables can be improved by adding additional low-pass filters to enhance the attenuation of noise on the cell lines and decrease the transmission of the rf pulse signal towards the potentiostat.

In future, a variety of *in-operando* NMR measurements on different battery cells are possible, even without any further developments and extensions of the setups presented in this work. For the time being, Li-plating during fast charging is in the focus of many research activities. Especially for improvements of electric vehicles safe and long-lasting batteries are desired. In-operando NMR may contribute significantly and shall answer many more remaining questions about the electrochemistry in battery cells.

9. Acknowledgement

Thanks to Prof. Dr. Josef Granwehr for supervision and untiring support. It was a great pleasure for me to work in his research group. Thanks to Prof. Dr. Rüdiger Eichel, Christian Hellenbrandt, Dr. Peter Jakes, Dr. Achim Mester, Dr. Andreas Mertens, Dr. Kevin Schiemann, Severin Foit, Dr. Arvid Niemöller, Dr. Leonard Kröll, Dr. Emre Durmus, Özgür Aslanbas, Andreas Ohligschläger, Dr. Hermann Tempel, Dr. Hans Kungl, Chantal Hake, Michaela Fittkau, Birgit Derksen, Magnus Graf, Daniel Hanß, Dr. Zigeng Liu, Marc and Anja Paulus, Dr. Roland Schierholz, Dr. Simone Köcher, Dr. Philipp Schleker, Dr. Martin Süfke, Dr. Ruoheng Sun, Jörg Ackermann, Sven Jovanovic, Heeyong Park, Saul Montiel Guerrero, Svitlana Eurich, Dr. Shicheng Yu, Dr. Egon Zimmermann, Dr. Ico Vinke, Dr. Bert de Haart, Prof. Dr. Peter Notten, Prof. Dr. Florian Hausen, Svenja Benning, Nino Schön, Lucy Dittrich, Trutz Teurer, Tanja Brambach, Claudia Tropartz and Josef Mertens for excellent collaboration and inspiring discussions. Thanks to Sven Reiter, Heinrich Pier and Knut Dahlhoff from Forschungszentrum Jülich ZEA-1 for the container manufacturing, to Norbert Merl and Torge Thönnessen from Custom Cells for discussions and supply with electrode materials, to Helmut Timmermanns from Forschungszentrum Jülich ZEA-2 for the photography of the setup and to Dr. Dieter Groß, Dr. Klaus Zick, Volker Lehmann and Walter Knöller from Bruker BioSpin GmbH Germany for their help, hospitality and inspiring discussions. Financial support by the German Federal Ministry of Education and Research (BMBF, Project AlSiBat) is gratefully acknowledged.

Many thanks to my wife Anja, my mother and father, my grandparents Oma and Opa Wehner, my new parents Heidi and Günter Böhmer and God for indispensable support and dependability through numerous days and nights.

10. References

(1) Kayser, S. A.; Mester, A.; Mertens, A.; Jakes, P.; Eichel, R.-A.; Granwehr, J. Long-Run in Operando NMR to Investigate the Evolution and Degradation of Battery Cells. *Phys. Chem. Chem. Phys.* **2018**, *20*, 13765.

(2) Kayser, S. A.; Mester, A.; Mertens, A.; Jakes, P.; Eichel, R.-A.; Granwehr, J. Long-Run in-Operando NMR to Investigate the Evolution and Degradation of Battery Cells. *ArXiv* **2017**, *1710.02577*, 1–20.

(3) Kayser, S. A.; Granwehr, J.; Hellenbrandt, C.; Jakes, P.; Niemöller, A.; Eichel, R.-A. Vorrichtung Zur Aufnahme Einer Elektrochemischen Zelle Für Magnet Resonanz Untersuchungen Sowie Verfahren Zur Herstellung Eines Stromabnehmers. DPMA Patent 102016005170, 2016.

(4) Grey, C. P.; Greenbaum, S. G. Nuclear Magnetic Resonance Studies of Lithium-Ion Battery Materials. *MRS Bull.* **2002**, *27* (8), 613–618+594.

(5) Blanc, F.; Leskes, M.; Grey, C. P. In Situ Solid-State NMR Spectroscopy of Electrochemical Cells: Batteries, Supercapacitors, and Fuel Cells. *Acc. Chem. Res.* **2013**, *46* (9), 1952–1963.

(6) Harks, P.-P.; Mulder, F. M.; Notten, P. H. L. In Situ Methods for Li-Ion Battery Research: A Review of Recent Developments. *J. Power Sources* **2015**, *288* (August), 92–105.

(7) Griffin, J. M.; Forse, A. C.; Grey, C. P. Solid-State NMR Studies of Supercapacitors. *Solid State Nucl. Magn. Reson.* **2016**, *74–75*, 16–35.

(8) Gerald, R. E.; Klingler, R. J.; Sandí, G.; Johnson, C. S.; Scanlon, L. G.; Rathke, J. W. ^{7}Li NMR Study of Intercalated Lithium in Curved Carbon Lattices. *J. Power Sources* **2000**, *89* (2), 237–243.

(9) Gerald, R. E.; Sanchez, J.; Johnson, C. S.; Klingler, R. J.; Rathke, J. W. In Situ Nuclear Magnetic Resonance Investigations of Lithium Ions in Carbon Electrode Materials Using a Novel Detector. *J. Phys. Condens. Matter* **2001**, *13* (36), 8269–8285.

(10) Rathke, J. W.; Klingler, R. J.; Gerald, R. E.; Kramarz, K. W.; Woelk, K. Toroids in NMR Spectroscopy. *Prog. Nucl. Magn. Reson. Spectrosc.* **1997**, *30*, 209–253.

(11) Letellier, M.; Chevallier, F.; Clinard, C.; Frackowiak, E.; Rouzaud, J.-N.; Béguin, F.; Morcrette, M.; Tarascon, J.-M. The First in Situ ^{7}Li Nuclear Magnetic Resonance Study of Lithium Insertion in Hard-Carbon Anode Materials for Li-Ion Batteries. *J. Chem. Phys.* **2003**, *118* (13), 6038–6045.

(12) Gozdz, A. S.; Schmutz, C. N.; Tarascon, J.-M.; Warren, P. C. Method of Making an Electrolyte Activatable Lithiul-Ion Rechargeable Battery Cell. US Patent 5456000, 1995.

(13) Tarascon, J. M.; Gozdz, A. S.; Schmutz, C.; Shokoohi, F.; Warren, P. C. Performance of Bellcore's Plastic Rechargeable Li-Ion Batteries. *Solid State Ionics* **1996**, *86–88* (PART 1), 49–54.

(14) Key, B.; Bhattacharyya, R.; Morcrette, M.; Seznec, V.; Tarascon, J. M.; Grey, C. P. Real-Time NMR Investigations of Structural Changes in Silicon Electrodes for Lithium-Ion Batteries. *J. Am. Chem. Soc.* **2009**, *131* (26), 9239–9249.

(15) Bhattacharyya, R.; Key, B.; Chen, H.; Best, A. S.; Hollenkamp, A. F.; Grey, C. P. In Situ NMR Observation of the Formation of Metallic Lithium Microstructures in Lithium Batteries. *Nat. Mater.* **2010**, *9* (6), 504–510.

(16) Chandrashekar, S.; Trease, N. M.; Chang, H. J.; Du, L.-S.; Grey, C. P.; Jerschow, A. ^{7}Li MRI of Li Batteries Reveals Location of Microstructural Lithium. *Nat. Mater.* **2012**, *11* (4), 311–315.

(17) Zhou, L.; Leskes, M.; Ilott, A. J.; Trease, N. M.; Grey, C. P. Paramagnetic Electrodes and Bulk Magnetic Susceptibility Effects in the in Situ NMR Studies of Batteries: Application to $Li_{1.08}Mn_{1.92}O_4$ Spinels. *J. Magn. Reson.* **2013**, *234*, 44–57.

(18) Ogata, K.; Salager, E.; Kerr, C. J.; Fraser, A. E.; Ducati, C.; Morris, A. J.; Hofmann, S.; Grey, C. P. Revealing Lithium–silicide Phase Transformations in Nano-Structured Silicon-Based Lithium Ion Batteries via in Situ NMR Spectroscopy. *Nat. Commun.* **2014**, *5*, 1–11.

(19) Chang, H. J.; Trease, N. M.; Ilott, A. J.; Zeng, D.; Du, L. S.; Jerschow, A.; Grey, C. P. Investigating Li Microstructure Formation on Li Anodes for Lithium Batteries by in Situ ^{6}Li/^{7}Li NMR and SEM. *J. Phys. Chem. C* **2015**, *119* (29), 16443–16451.

(20) Pecher, O.; Bayley, P. M.; Liu, H.; Liu, Z.; Trease, N. M.; Grey, C. P. Automatic Tuning Matching Cycler (ATMC) in Situ NMR Spectroscopy as a Novel Approach for Real-Time Investigations of Li-and Na-Ion Batteries. *J. Magn. Reson.* **2016**, *265*, 200–209.

(21) Gotoh, K.; Izuka, M.; Arai, J.; Okada, Y.; Sugiyama, T.; Takeda, K.; Ishida, H. In Situ ^{7}Li Nuclear Magnetic Resonance Study of the Relaxation Effect in Practical Lithium Ion Batteries. *Carbon N. Y.* **2014**, *79* (1), 380–387.

(22) Arai, J.; Okada, Y.; Sugiyama, T.; Izuka, M.; Gotoh, K.; Takeda, K. In Situ Solid State ^{7}Li NMR Observations of Lithium Metal Deposition during Overcharge in Lithium Ion Batteries. *J. Electrochem. Soc.* **2015**, *162* (6), A952–A958.

(23) Arai, J.; Gotoh, K.; Sayama, R.; Takeda, K. Slow Stabilization of Si-Li Alloys Formed during Charge and Discharge of a Si-C Mixed Electrode Studied by In Situ Solid-State ^{7}Li Nuclear Magnetic Resonance Spectroscopy. *J. Electrochem. Soc.* **2017**, *164* (1), A6334–A6340.

(24) Trease, N. M.; Zhou, L.; Chang, H. J.; Zhu, B. Y.; Grey, C. P. In Situ NMR of Lithium Ion Batteries: Bulk Susceptibility Effects and Practical Considerations. *Solid State Nucl. Magn. Reson.* **2012**, *42*, 62–70.

(25) Arai, J.; Nakahigashi, R.; Sugiyama, T. A Study on the Cycle Life of Lithium-Ion Batteries Using In Situ ^{7}Li Solid-State Nuclear Magnetic Resonance. *J. Electrochem. Soc.* **2016**, *163* (6), A1064–A1069.

(26) Poli, F.; Kshetrimayum, J. S.; Monconduit, L.; Letellier, M. New Cell Design for In-Situ NMR Studies of Lithium-Ion Batteries. *Electrochem. commun.* **2011**, *13* (12), 1293–1295.

(27) Ilott, A. J.; Chandrashekar, S.; Klöckner, A.; Chang, H. J.; Trease, N. M.; Grey, C. P.; Greengard, L.; Jerschow, A. Visualizing Skin Effects in Conductors with MRI: ^{7}Li MRI Experiments and Calculations. *J. Magn. Reson.* **2014**, *245*, 143–149.

(28) Romanenko, K.; Forsyth, M.; O'Dell, L. A. New Opportunities for Quantitative and Time Efficient 3D MRI of Liquid and Solid Electrochemical Cell Components: Sectoral Fast Spin Echo and SPRITE. *J. Magn. Reson.* **2014**, *248*, 96–104.

(29) Poli, F.; Wong, A.; Kshetrimayum, J. S.; Monconduit, L.; Letellier, M. In Situ NMR Insights into the Electrochemical Reaction of Cu_3P Electrodes in Lithium Batteries. *Chem. Mater.* **2016**, *28* (6), 1787–1793.

(30) Niemöller, A.; Jakes, P.; Kayser, S.; Lin, Y.; Lehnert, W.; Granwehr, J. 3D Printed Sample Holder for In-Operando EPR Spectroscopy on High Temperature Polymer Electrolyte Fuel Cells. *J. Magn. Reson.* **2016**, *269*, 157–161.

(31) Xiao, J.; Hu, J. Z.; Chen, H.; Vijayakumar, M.; Zheng, J.; Pan, H.; Walter, E. D.; Hu, M.; Deng, X.; Feng, J.; et al. Following the Transient Reactions in Lithium-Sulfur Batteries Using an in Situ Nuclear Magnetic Resonance Technique. *Nano Lett.* **2015**, *15* (5), 3309–3316.

(32) Hu, J. Z.; Zhao, Z.; Hu, M. Y.; Feng, J.; Deng, X.; Chen, X.; Xu, W.; Liu, J.; Zhang, J. G. In Situ ^{7}Li and ^{133}Cs Nuclear Magnetic Resonance Investigations on the Role of Cs^{+} Additive in Lithium-Metal Deposition Process. *J. Power Sources* **2016**, *304*, 51–59.

(33) Tang, W.; Goh, B.-M.; Hu, M. Y.; Wan, C.; Tian, B.; Deng, X.; Peng, C.; Lin, M.; Hu, J. Z.; Loh, K. P. In Situ Raman and Nuclear Magnetic Resonance Study of Trapped Lithium in the Solid Electrolyte Interface of Reduced Graphene Oxide. *J. Phys. Chem. C* **2016**, *120* (5), 2600–2608.

(34) Salager, E.; Sarou-Kanian, V.; Sathiya, M.; Tang, M.; Leriche, J.-B.; Melin, P.; Wang, Z.; Vezin, H.; Bessada, C.; Deschamps, M.; et al. Solid-State NMR of the Family of Positive Electrode Materials $Li_2Ru_{1-y}Sn_yO_3$ for Lithium-Ion Batteries. *Chem. Mater.* **2014**, *26* (24), 7009–7019.

(35) Tang, M.; Sarou-Kanian, V.; Melin, P.; Leriche, J.-B.; Ménétrier, M.; Tarascon, J.-M.; Deschamps, M.; Salager, E. Following Lithiation Fronts in Paramagnetic Electrodes with in Situ Magnetic Resonance Spectroscopic Imaging. *Nat. Commun.* **2016**, *7* (November), 13284.

(36) Neufeld, A.; Landsberg, N.; Boag, A. Dielectric Inserts for Sensitivity and RF Magnetic Field Enhancement in NMR Volume Coils. *J. Magn. Reson.* **2009**, *200* (1), 49–55.

(37) Jasiński, K.; Młynarczyk, A.; Latta, P.; Volotovskyy, V.; Weglarz, W. P.; Tomanek, B. A Volume

Microstrip RF Coil for MRI Microscopy. *Magn. Reson. Imaging* **2012**, *30* (1), 70–77.

(38) Dietrich, J.; Sebak, A. Automating NEC2 with Matlab for Antenna Analysis and Design. *IEEE CCECE2002. Can. Conf. Electr. Comput. Eng. Conf. Proc. (Cat. No. 02CH37373)* **2002**, *1*, 342–346.

(39) Chang, H. J.; Ilott, A. J.; Trease, N. M.; Mohammadi, M.; Jerschow, A.; Grey, C. P. Correlating Microstructural Lithium Metal Growth with Electrolyte Salt Depletion in Lithium Batteries Using ^{7}Li MRI. *J. Am. Chem. Soc.* **2015**, *137* (48), 15209–15216.

(40) Klett, M.; Giesecke, M.; Nyman, A.; Hallberg, F.; Lindström, R. W.; Lindbergh, G.; Furó, I. Quantifying Mass Transport during Polarization in a Li Ion Battery Electrolyte by in Situ ^{7}Li NMR Imaging. *J. Am. Chem. Soc.* **2012**, *134* (36), 14654–14657.

(41) Klamor, S.; Zick, K.; Oerther, T.; Schappacher, F. M.; Winter, M.; Brunklaus, G. ^{7}Li in Situ 1D NMR Imaging of a Lithium Ion Battery. *Phys. Chem. Chem. Phys.* **2015**, *17* (6), 4458–4465.

(42) Tang, J. A.; Zhong, G.; Dugar, S.; Kitchen, J. A.; Yang, Y.; Fu, R. Solid-State STRAFI NMR Probe for Material Imaging of Quadrupolar Nuclei. *J. Magn. Reson.* **2012**, *225*, 93–101.

(43) Tang, J. A.; Dugar, S.; Zhong, G.; Dalal, N. S.; Zheng, J. P.; Yang, Y.; Fu, R. Non-Destructive Monitoring of Charge-Discharge Cycles on Lithium Ion Batteries Using ^{7}Li Stray-Field Imaging. *Sci. Rep.* **2013**, *3* (1), 2596.

(44) Krachkovskiy, S. A.; Bazak, J. D.; Werhun, P.; Balcom, B. J.; Halalay, I. C.; Goward, G. R. Visualization of Steady-State Ionic Concentration Profiles Formed in Electrolytes during Li-Ion Battery Operation and Determination of Mass-Transport Properties by in Situ Magnetic Resonance Imaging. *J. Am. Chem. Soc.* **2016**, *138* (25), 7992–7999.

(45) Ilott, A. J.; Mohammadi, M.; Chang, H. J.; Grey, C. P.; Jerschow, A. Real-Time 3D Imaging of Microstructure Growth in Battery Cells Using Indirect MRI. *Proc. Natl. Acad. Sci.* **2016**, *113* (39), 10779–10784.

(46) Chen, H.; Cartmell, S.; Wang, Q.; Lozano, T.; Deng, Z. D.; Li, H.; Chen, X.; Yuan, Y.; Gross, M. E.; Carlson, T. J.; et al. Micro-Battery Development for Juvenile Salmon Acoustic Telemetry System Applications. *Sci. Rep.* **2014**, *4*, 3790.

(47) Wandt, J.; Marino, C.; Gasteiger, H. A.; Jakes, P.; Eichel, R.-A.; Granwehr, J. *Operando* Electron Paramagnetic Resonance Spectroscopy – Formation of Mossy Lithium on Lithium Anodes during Charge–discharge Cycling. *Energy Environ. Sci.* **2015**, *8* (4), 1358–1367.

(48) Durmus, Y. E.; Aslanbas, Ö.; Kayser, S.; Tempel, H.; Hausen, F.; de Haart, L. G. J.; Granwehr, J.; Ein-Eli, Y.; Eichel, R.-A.; Kungl, H. Long Run Discharge, Performance and Efficiency of Primary Silicon–air Cells with Alkaline Electrolyte. *Electrochim. Acta* **2017**, *225*, 215–224.

(49) Huggins, R. A. *Advanced Batteries: Materials Science Aspects*; 2009.

(50) Lide, D. R. *CRC Handbook of Chemistry and Physics, 96th Edition, 2015-2016*; 2014.

(51) Winter, M.; Besenhard, J. O.; Spahr, M. E.; Novak, P. Insertion Electrode Materials for Rechargeable Lithium Batteries. *Adv. Mater.* **1998**, *10*, 725–765.

(52) Sethuraman, V. A.; Hardwick, L. J.; Srinivasan, V.; Kostecki, R. Surface Structural Disordering in Graphite upon Lithium Intercalation/Deintercalation. *J. Power Sources* **2010**, *195* (11), 3655–3660.

(53) Orsini, F.; Du Pasquier, A.; Beaudoin, B.; Tarascon, J. M.; Trentin, M.; Langenhuizen, N.; De Beer, E.; Notten, P. In Situ Scanning Electron Microscopy (SEM) Observation of Interfaces within Plastic Lithium Batteries. *J. Power Sources* **1998**, *76* (1), 19–29.

(54) Mukai, K.; Inoue, T. Magnetic Susceptibility Measurements on Li-Intercalated Graphite: Paramagnetic to Diamagnetic Transitions in C_{12}Li Induced by Magnetic Field. *Carbon N. Y.* **2017**, *123*, 645–650.

(55) Nitta, N.; Wu, F.; Lee, J. T.; Yushin, G. Li-Ion Battery Materials: Present and Future. *Mater. Today* **2015**, *18* (5), 252–264.

(56) Yang, Y.; Liu, X.; Dai, Z.; Yuan, F.; Bando, Y.; Golberg, D.; Wang, X. In Situ Electrochemistry of Rechargeable Battery Materials: Status Report and Perspectives. *Adv. Mater.* **2017**, *29* (31), 1–22.

(57) Muench, S.; Wild, A.; Friebe, C.; Häupler, B.; Janoschka, T.; Schubert, U. S. Polymer-Based Organic Batteries. *Chem. Rev.* **2016**, *116* (16), 9438–9484.

(58) López, C. M.; Vaughey, J. T.; Dees, D. W. Morphological Transitions on Lithium Metal Anodes. *J. Electrochem. Soc.* **2009**, *156* (9), A726.

(59) Amatucci, G. G.; Tarascon, J. M.; Klein, L. C. CoO_2, The End Member of the Li_xCoO_2 Solid Solution. *J. Electrochem. Soc.* **1996**, *143* (3), 1114.

(60) Mizushima, K.; Jones, P. C.; Wiseman, P. J.; Goodenough, J. B. Li_xCoO_2: A New Cathode Material for Batteries of High Energy Density. *Solid State Ionics* **1981**, *3–4* (C), 171–174.

(61) Wandt, J.; Jakes, P.; Granwehr, J.; Eichel, R.-A.; Gasteiger, H. A. Quantitative and Time-Resolved Detection of Lithium Plating on Graphite Anodes in Lithium Ion Batteries. *Mater. Today* **2018**, *21* (3), 231–240.

(62) Liu, C.; Neale, Z. G.; Cao, G. Understanding Electrochemical Potentials of Cathode Materials in Rechargeable Batteries. *Mater. Today* **2016**, *19* (2), 109–123.

(63) Chen, Z.; Lu, Z.; Dahn, J. R. Staging Phase Transitions in Li_xCoO_2. *J. Electrochem. Soc.* **2002**, *149* (12), A1604–A1609.

(64) Shimoda, K.; Murakami, M.; Takamatsu, D.; Arai, H.; Uchimoto, Y.; Ogumi, Z. In Situ NMR Observation of the Lithium Extraction/Insertion from $LiCoO_2$ Cathode. *Electrochim. Acta* **2013**, *108*, 343–349.

(65) Chen, Z.; Dahn, J. R. Methods to Obtain Excellent Capacity Retention in $LiCoO_2$ Cycled to 4.5 V. *Electrochim. Acta* **2004**, *49* (7), 1079–1090.

(66) Downing, B. W. Metal-Air Technology. In *Electrochemical Technologies for Energy Storage and Conversion*; 2012; Vol. 1, pp 239–277.

(67) Cheng, F.; Chen, J. Metal–air Batteries: From Oxygen Reduction Electrochemistry to Cathode Catalysts. *Chem. Soc. Rev.* **2012**, *41* (6), 2172.

(68) Kraytsberg, A.; Ein-Eli, Y. Review on Li-Air Batteries - Opportunities, Limitations and Perspective. *J. Power Sources* **2011**, *196* (3), 886–893.

(69) Jakes, P.; Cohn, G.; Ein-Eli, Y.; Scheiba, F.; Ehrenberg, H.; Eichel, R.-A. Limitation of Discharge Capacity and Mechanisms of Air-Electrode Deactivation in Silicon-Air Batteries. *ChemSusChem* **2012**, *5* (11), 2278–2285.

(70) Durmus, Y. E.; Montiel Guerrero, S. S.; Aslanbas, Ö.; Tempel, H.; Hausen, F.; de Haart, L. G. J.; Ein-Eli, Y.; Eichel, R.-A.; Kungl, H. Investigation of the Corrosion Behavior of Highly As-Doped Crystalline Si in Alkaline Si–air Batteries. *Electrochim. Acta* **2018**, *265*, 292–302.

(71) Lee, J. S.; Kim, S. T.; Cao, R.; Choi, N. S.; Liu, M.; Lee, K. T.; Cho, J. Metal-Air Batteries with High Energy Density: Li-Air versus Zn-Air. *Adv. Energy Mater.* **2011**, *1* (1), 34–50.

(72) Balaish, M.; Kraytsberg, A.; Ein-Eli, Y. Realization of an Artificial Three-Phase Reaction Zone in a Li-Air Battery. *ChemElectroChem* **2014**, *1* (1).

(73) Knight, C. T. G.; Balec, R. J.; Kinrade, S. D. The Structure of Silicate Anions in Aqueous Alkaline Solutions. *Angew. Chemie - Int. Ed.* **2007**, *46* (43), 8148–8152.

(74) Seidel, H.; Csepregi, L.; Heuberger, A.; Baumgärtel, H. Anisotropic Etching of Crystalline Silicon in Alkaline Solutions. *J. Electrochem. Soc.* **1990**, *137* (11), 3612.

(75) Palik, E. D.; Gray, H. F.; Klein, P. B. A Raman Study of Etching Silicon in Aqueous KOH. *J. Electrochem. Soc.* **1983**, *130* (4), 956.

(76) Huang, Z.; Geyer, N.; Werner, P.; De Boor, J.; Gösele, U. Metal-Assisted Chemical Etching of Silicon: A Review. *Adv. Mater.* **2011**, *23* (2), 285–308.

(77) Garamoun, A.; Schubert, M. B.; Werner, J. H. Thin-Film Silicon for Flexible Metal-Air Batteries. *ChemSusChem* **2014**, *7* (12), 3272–3274.

(78) Gelman, D.; Lasman, I.; Elfimchev, S.; Starosvetsky, D.; Ein-Eli, Y. Aluminum Corrosion Mitigation in Alkaline Electrolytes Containing Hybrid Inorganic/Organic Inhibitor System for Power Sources Applications. *J. Power Sources* **2015**, *285*, 100–108.

(79) Liang, M.; Zhou, H.; Huang, Q.; Hu, S.; Li, W. Synergistic Effect of Polyethylene Glycol 600 and Polysorbate 20 on Corrosion Inhibition of Zinc Anode in Alkaline Batteries. *J. Appl. Electrochem.* **2011**, *41* (8), 991–997.

(80) Guilminot, E.; Dalard, F.; Degrigny, C. Mechanism of Iron Corrosion in Water-Polyethylene Glycol (PEG 400) Mixtures. *Corros. Sci.* **2002**, *44* (10), 2199–2208.

(81) Umoren, S. A.; Ogbobe, O.; Okafor, P. C.; Ebenso, E. E. Polyethylene Glycol and Polyvinyl Alcohol as Corrosion Inhibitors for Aluminium in Acidic Medium. *J. Appl. Polym. Sci.* **2007**, *105* (6), 3363–3370.

(82) Shukla, J.; Pitre, K. S.; Jain, P. Inhibitive Effect of PEG on the Corrosion of Aluminium in Acidic Medium. *Indian J. Chem. - Sect. A Inorganic, Phys. Theor. Anal. Chem.* **2003**, *42* (11), 2784–2787.

(83) Zhou, H.; Huang, Q.; Liang, M.; Lv, D.; Xu, M.; Li, H.; Li, W. Investigation on Synergism of Composite Additives for Zinc Corrosion Inhibition in Alkaline Solution. *Mater. Chem. Phys.* **2011**, *128* (1–2), 214–219.

(84) Sun, K. E. K.; Hoang, T. K. A.; Doan, T. N. L.; Yu, Y.; Zhu, X.; Tian, Y.; Chen, P. Suppression of Dendrite Formation and Corrosion on Zinc Anode of Secondary Aqueous Batteries. *ACS Appl. Mater. Interfaces* **2017**, *9* (11), 9681–9687.

(85) Levitt, M. . *Spin Dynamics: Basics of Nuclear Magnetic Resonance*; 2000.

(86) Blümich, B. *Essential NMR: For Scientists and Engineers*; 2005.

(87) Granwehr, J. Multiplicative or t_1 Noise in NMR Spectroscopy. *Appl. Magn. Reson.* **2007**, *32* (1–2), 113–156.

(88) Dietrich, W.; Rüdel, C. H.; Neumann, M. Fast and Precise Automatic Baseline Correction of One- and Two-Dimensional Nmr Spectra. *J. Magn. Reson.* **1991**, *91* (1), 1–11.

(89) Wagemaker, M.; Simon, D. R.; Kelder, E. M.; Schoonman, J.; Ringpfeil, C.; Haake, U.; Lützenkirchen-Hecht, D.; Frahm, R.; Mulder, F. M. A Kinetic Two-Phase and Equilibrium Solid Solution in Spinel $Li_{4+x}Ti_5O_{12}$. *Adv. Mater.* **2006**.

(90) Graf, M. F.; Tempel, H.; Köcher, S. S.; Schierholz, R.; Scheurer, C.; Kungl, H.; Eichel, R.-A.; Granwehr, J. Observing Different Modes of Mobility in Lithium Titanate Spinel by Nuclear Magnetic Resonance. *RSC Adv.* **2017**.

(91) Heinzel, T. Surfaces , Interfaces , and Layered Devices. *Electronics* **2007**, 57–95.

(92) Dey, A. N. Electrochemical Alloying of Lithium in Organic Electrolytes. *J. Electrochem. Soc.* **1971**, *118* (10), 1547–1549.

(93) Blundell, D. J.; Osborn, B. N. The Morphology of Poly(Aryl-Ether-Ether-Ketone). *Polymer (Guildf).* **1983**, *24* (8), 953–958.

(94) Rae, P. J.; Brown, E. N.; Orler, E. B. The Mechanical Properties of Poly(Ether-Ether-Ketone) (PEEK) with Emphasis on the Large Compressive Strain Response. *Polymer (Guildf).* **2007**, *48* (2), 598–615.

(95) Frick, A.; Sich, D.; Heinrich, G.; Stern, C.; Gössi, M.; Tervoort, T. A. Relationship between Structure and Mechanical Properties of Melt Processable PTFE: Influence of Molecular Weight and Comonomer Content. *Macromol. Mater. Eng.* **2013**, *298* (9), 954–966.

(96) Yurchenko, M. E.; Huang, J.; Robisson, A.; McKinley, G. H.; Hammond, P. T. Synthesis, Mechanical Properties and Chemical/Solvent Resistance of Crosslinked Poly(Aryl-Ether-Ether-Ketones) at High Temperatures. *Polymer (Guildf).* **2010**, *51* (9), 1914–1920.

(97) Mertens, A.; Granwehr, J. Two-Dimensional Impedance Data Analysis by the Distribution of Relaxation Times. *J. Energy Storage* **2017**, *13*, 401–408.

(98) Pop, V.; Bergveld, H. J.; Regtien, P. P. L.; Op het Veld, J. H. G.; Danilov, D.; Notten, P. H. L. Battery Aging and Its Influence on the Electromotive Force. *J. Electrochem. Soc.* **2007**, *154* (8), A744.

(99) Pop, V.; Bergveld, H. J.; Notten, P. H. L.; Op het Veld, J. H. G.; Regtien, P. P. L. Accuracy Analysis of the State-of-Charge and Remaining Run-Time Determination for Lithium-Ion Batteries. *Meas. J. Int. Meas. Confed.* **2009**, *42* (8), 1131–1138.

(100) Notten, P. H. L.; Danilov, D. L. Battery Modeling: A Versatile Tool to Design Advanced Battery

Management Systems. *Adv. Chem. Eng. Sci.* **2014**, *04* (01), 62–72.

(101) Danilov, D.; Notten, P. H. L. Adaptive Battery Management Systems for the New Generation of Electrical Vehicles. *2009 IEEE Veh. Power Propuls. Conf.* **2009**, No. 2, 317–320.

(102) Pop, V.; Bergveld, H. J.; Op het Veld, J. H. G.; Regtien, P. P. L.; Danilov, D.; Notten, P. H. L. Modeling Battery Behavior for Accurate State-of-Charge Indication. *J. Electrochem. Soc.* **2006**, *153* (11), A2013.

(103) Pop, V.; Bergveld, H. J.; Notten, P. H. L.; Regtien, P. P. L. State-of-the-Art of Battery State-of-Charge Determination. *Meas. Sci. Technol.* **2005**, *16* (12).

(104) Reimers, J. N.; Dahn, J. R. Electrochemical and in Situ X-Ray Diffraction Studies of Lithium Intercalation in Li_xCoO_2. *J Electrochem. Soc.* **1992**, *139* (8), 2091–2096.

(105) Odziemkowski, M.; Irish, D. E. An Electrochemical Study of the Reactivity at the Lithium Electrolyte/Bare Lithium Metal Interface. *J. Electrochem. Soc.* **1992**, *139* (11), 3063–3074.

(106) Peled, E.; Menkin, S. Review—SEI: Past, Present and Future. *J. Electrochem. Soc.* **2017**, *164* (7), A1703–A1719.

(107) Aurbach, D. Review of Selected Electrode-Solution Interactions Which Determine the Performance of Li and Li Ion Batteries. *J. Power Sources* **2000**, *89* (2), 206–218.

(108) Aurbach, D.; Zinigrad, E.; Cohen, Y.; Teller, H. A Short Review of Failure Mechanisms of Lithium Metal and Lithiated Graphite Anodes in Liquid Electrolyte Solutions. *Solid State Ionics* **2002**, *148* (3–4), 405–416.

(109) Aurbach, D. The Correlation Between Surface Chemistry, Surface Morphology, and Cycling Efficiency of Lithium Electrodes in a Few Polar Aprotic Systems. *J. Electrochem. Soc.* **1989**, *136* (11), 3198–3205.

(110) Arakawa, M.; Tobishima, S. ichi; Nemoto, Y.; Ichimura, M.; Yamaki, J. ichi. Lithium Electrode Cycleability and Morphology Dependence on Current Density. *J. Power Sources* **1993**, *43* (1–3), 27–35.

(111) Yamaki, J.; Tobishima, S.; Hayashi, K.; Keiichi Saito; Nemoto, Y.; Arakawa, M. A Consideration of the Morphology of Electrochemically Deposited Lithium in an Organic Electrolyte. *J. Power Sources* **1998**, *74* (2), 219–227.

(112) Schichlein, H.; Müller, A.; Voigts, M.; Krügel, A.; Ivers-Tiffée, E. Deconvolution of Electrochemical Impedance Spectra for the Identification of Electrode Reaction Mechanisms in Solid Oxide Fuel Cells. *J. Appl. Electrochem.* **2002**, *32* (8), 875–882.

(113) Granwehr, J.; Roberts, P. J. Inverse Laplace Transform of Multidimensional Relaxation Data without Non-Negativity Constraint. *J. Chem. Theory Comput.* **2012**, *8* (10), 3473–3482.

(114) Aurbach, D. Common Electroanalytical Behavior of Li Intercalation Processes into Graphite and Transition Metal Oxides. *J. Electrochem. Soc.* **1998**, *145* (9), 3024.

(115) Illig, J.; Schmidt, J. P.; Weiss, M.; Weber, A.; Ivers-Tiffée, E. Understanding the Impedance Spectrum of 18650 $LiFePO_4$-Cells. *J. Power Sources* **2013**, *239*, 670–679.

(116) Wang, C.; Kakwan, I.; Appleby, A. J.; Little, F. E. In Situ Investigation of Electrochemical Lithium Intercalation into Graphite Powder. *J. Electroanal. Chem.* **2000**, *489* (1–2), 55–67.

(117) Chen, K.-H.; Wood, K. N.; Kazyak, E.; LePage, W. S.; Davis, A. L.; Sanchez, A. J.; Dasgupta, N. P. Dead Lithium: Mass Transport Effects on Voltage, Capacity, and Failure of Lithium Metal Anodes. *J. Mater. Chem. A* **2017**, *5* (23), 11671–11681.

(118) Langer, J.; Epp, V.; Heitjans, P.; Mautner, F. A.; Wilkening, M. Lithium Motion in the Anode Material LiC_6 as Seen via Time-Domain ^{7}Li NMR. *Phys. Rev. B - Condens. Matter Mater. Phys.* **2013**, *88* (9), 094304.

(119) Letellier, M.; Chevallier, F.; Béguin, F. In Situ ^{7}Li NMR during Lithium Electrochemical Insertion into Graphite and a Carbon/Carbon Composite. *J. Phys. Chem. Solids* **2006**, *67* (5–6), 1228–1232.

(120) Letellier, M.; Chevallier, F.; Morcrette, M. In Situ ^{7}Li Nuclear Magnetic Resonance Observation of the Electrochemical Intercalation of Lithium in Graphite; 1st Cycle. *Carbon N. Y.* **2007**, *45* (5), 1025–1034.

(121) Chevallier, F.; Poli, F.; Montigny, B.; Letellier, M. In Situ ^{7}Li Nuclear Magnetic Resonance Observation of the Electrochemical Intercalation of Lithium in Graphite: Second Cycle Analysis. *Carbon N. Y.* **2013**, *61*, 140–153.

(122) Xu, W.; Wang, J.; Ding, F.; Chen, X.; Nasybulin, E.; Zhang, Y.; Zhang, J.-G. Lithium Metal Anodes for Rechargeable Batteries. *Energy Environ. Sci.* **2014**, *7* (2), 513–537.

(123) Yoshimatsu, I. Lithium Electrode Morphology during Cycling in Lithium Cells. *J. Electrochem. Soc.* **1988**, *135* (10), 2422–2427.

(124) Aurbach, D.; Weissman, I.; Zaban, A.; Chusid, O. Correlation between Surface Chemistry, Morphology, Cycling Efficiency and Interfacial Properties of Li Electrodes in Solutions Containing Different Li Salts. *Electrochim. Acta* **1994**, *39* (1), 51–71.

(125) Kim, H.; Jeong, G.; Kim, Y.-U.; Kim, J.-H.; Park, C.-M.; Sohn, H.-J. Metallic Anodes for next Generation Secondary Batteries. *Chem. Soc. Rev.* **2013**, *42* (23), 9011.

(126) Ghassemi, H.; Au, M.; Chen, N.; Heiden, P. A.; Yassar, R. S. Real-Time Observation of Lithium Fibers Growth inside a Nanoscale Lithium-Ion Battery. *Appl. Phys. Lett.* **2011**, *99* (12), 1–4.

(127) Michan, A. L.; Leskes, M.; Grey, C. P. Voltage Dependent Solid Electrolyte Interphase Formation in Silicon Electrodes: Monitoring the Formation of Organic Decomposition Products. *Chem. Mater.* **2016**, *28* (1), 385–398.

(128) Zhang, L.; Li, X.; Augustsson, A.; Lee, C. M.; Rubensson, J. E.; Nordgren, J.; Ross, P. N.; Guo, J. H. Revealing the Electronic Structure of LiC_6 by Soft X-Ray Spectroscopy. *Appl. Phys. Lett.* **2017**, *110* (10).

(129) Wood, K. N.; Noked, M.; Dasgupta, N. P. Lithium Metal Anodes: Toward an Improved Understanding of Coupled Morphological, Electrochemical, and Mechanical Behavior. *ACS Energy Lett.* **2017**, *2* (3), 664–672.

(130) Steiger, J.; Kramer, D.; Moenig, R. Microscopic Observations of the Formation, Growth and Shrinkage of Lithium Moss during Electrodeposition and Dissolution. *Electrochim. Acta* **2014**, *136*, 529–536.

(131) Sun, F.; Zielke, L.; Markötter, H.; Hilger, A.; Zhou, D.; Moroni, R.; Zengerle, R.; Thiele, S.; Banhart, J.; Manke, I. Morphological Evolution of Electrochemically Plated/Stripped Lithium Microstructures Investigated by Synchrotron X-Ray Phase Contrast Tomography. *ACS Nano* **2016**, *10* (8), 7990–7997.

(132) Ménétrier, M.; Saadoune, I.; Levasseur, S.; Delmas, C. The Insulator-Metal Transition upon Lithium Deintercalation from $LiCoO_2$: Electronic Properties and ^{7}Li NMR Study. *J. Mater. Chem.* **1999**, *9* (5), 1135–1140.

(133) Murakami, M.; Yamashige, H.; Arai, H.; Uchimoto, Y.; Ogumi, Z. Association of Paramagnetic Species with Formation of LiF at the Surface of $LiCoO_2$. *Electrochim. Acta* **2012**, *78*, 49–54.

(134) Zhou, L.; Leskes, M.; Ilott, A. J.; Trease, N. M.; Grey, C. P. Paramagnetic Electrodes and Bulk Magnetic Susceptibility Effects in the in Situ NMR Studies of Batteries: Application to $Li_{1.08}Mn_{1.92}O_4$ Spinels. *J. Magn. Reson.* **2013**, *234*, 44–57.

(135) Pecher, O.; Halat, D. M.; Lee, J.; Liu, Z.; Griffith, K. J.; Braun, M.; Grey, C. P. Enhanced Efficiency of Solid-State NMR Investigations of Energy Materials Using an External Automatic Tuning/Matching (EATM) Robot. *J. Magn. Reson.* **2017**, *275*, 127–136.

(136) Montoro, L. A.; Abbate, M.; Rosolen, J. M. Changes in the Electronic Structure of Chemically Deintercalated $LiCoO_2$. *Electrochem. Solid State Lett.* **2000**, *3* (9), 410–412.

(137) Uchimoto, Y.; Sawada, H.; Yao, T. Changes in Electronic Structure by Li Ion Deintercalation in $LiCoO_2$ from Cobalt L-Edge and Oxygen K-Edge XANES. *J. Synchrotron Radiat.* **2001**, *8* (2), 872–873.

(138) Niemöller, A.; Jakes, P.; Eichel, R.-A.; Granwehr, J. In Operando EPR Investigations of Redox Mechanisms in $LiCoO_2$. *Chem. Phys. Lett.* **2018**, *submitted*.

(139) Klinser, G.; Topolovec, S.; Kren, H.; Koller, S.; Krenn, H.; Würschum, R. Charging of Lithium Cobalt Oxide Battery Cathodes Studied by Means of Magnetometry. *Solid State Ionics* **2016**,

293, 64–71.

(140) Topolovec, S.; Kren, H.; Klinser, G.; Koller, S.; Krenn, H.; WÃ¼rschum, R. Operando Magnetometry on Li_xCoO_2 during Charging/Discharging. *J. Solid State Electrochem.* **2016**, *20* (5).

(141) Laubach, S.; Laubach, S.; Schmidt, P. C.; Ensling, D.; Schmid, S.; Jaegermann, W.; Thißen, A.; Nikolowski, K.; Ehrenberg, H. Changes in the Crystal and Electronic Structure of $LiCoO_2$ and $LiNiO_2$ upon Li Intercalation and de-Intercalation. *Phys. Chem. Chem. Phys.* **2009**, *11* (17), 3278.

(142) Shimoda, K.; Murakami, M.; Komatsu, H.; Arai, H.; Uchimoto, Y.; Ogumi, Z. Delithiation/Lithiation Behavior of $LiNi_{0.5}Mn_{1.5}O_4$ Studied by In Situ and Ex Situ ^{6,7}Li NMR Spectroscopy. *J. Phys. Chem. C* **2015**, *119* (24), 13472–13480.

(143) Chandrasekaran, R. Quantification of Bottlenecks to Fast Charging of Lithium-Ion-Insertion Cells for Electric Vehicles. *J. Power Sources* **2014**, *271*, 622–632.

(144) Keil, P.; Jossen, A. Charging Protocols for Lithium-Ion Batteries and Their Impact on Cycle Life-An Experimental Study with Different 18650 High-Power Cells. *J. Energy Storage* **2016**, *6*, 125–141.

(145) Dahn, J. R. Phase Diagram of Li_xC_6. *Phys. Rev. B* **1991**, *44* (17), 9170–9177.

(146) Hasan, M. F.; Chen, C.-F.; Shaffer, C. E.; Mukherjee, P. P. Analysis of the Implications of Rapid Charging on Lithium-Ion Battery Performance. *J. Electrochem. Soc.* **2015**, *162* (7), A1382–A1395.

(147) Li, J.; Yuan, C. F.; Guo, Z. H.; Zhang, Z. A.; Lai, Y. Q.; Liu, J. Limiting Factors for Low-Temperature Performance of Electrolytes in $LiFePO_4$/Li and Graphite/Li Half Cells. *Electrochim. Acta* **2012**, *59*, 69–74.

(148) Li, Z.; Huang, J.; Yann Liaw, B.; Metzler, V.; Zhang, J. A Review of Lithium Deposition in Lithium-Ion and Lithium Metal Secondary Batteries. *J. Power Sources* **2014**, *254*, 168–182.

(149) Liu, Q.; Du, C.; Shen, B.; Zuo, P.; Cheng, X.; Ma, Y.; Yin, G.; Gao, Y. Understanding of Undesirable Anode Lithium Plating Issues in Lithium-Ion Batteries. *RSC Adv.* **2016**, *6*, 88683–88700.

(150) Cho, H. M.; Choi, W. S.; Go, J. Y.; Bae, S. E.; Shin, H. C. A Study on Time-Dependent Low Temperature Power Performance of a Lithium-Ion Battery. *J. Power Sources* **2012**, *198*, 273–280.

(151) Gallagher, K. G.; Trask, S. E.; Bauer, C.; Woehrle, T.; Lux, S. F.; Tschech, M.; Lamp, P.; Polzin, B. J.; Ha, S.; Long, B.; et al. Optimizing Areal Capacities through Understanding the Limitations of Lithium-Ion Electrodes. *J. Electrochem. Soc.* **2016**, *163* (2), A138–A149.

(152) Ebner, M.; Chung, D. W.; García, R. E.; Wood, V. Tortuosity Anisotropy in Lithium-Ion Battery Electrodes. *Adv. Energy Mater.* **2014**, *4* (5), 1–6.

(153) Levi, M. D.; Aurbach, D. Diffusion Coefficients of Lithium Ions during Intercalation into Graphite Derived from the Simultaneous Measurements and Modeling of Electrochemical Impedance and Potentiostatic Intermittent Titration Characteristics of Thin Graphite Electrodes. *J. Phys. Chem. B* **1997**, *101* (23), 4641–4647.

(154) Persson, K.; Sethuraman, V. A.; Hardwick, L. J.; Hinuma, Y.; Meng, Y. S.; van der Ven, A.; Srinivasan, V.; Kostecki, R.; Ceder, G. Lithium Diffusion in Graphitic Carbon. *J. Phys. Chem. Lett.* **2010**, *1* (8), 1176–1180.

(155) Engelhardt, G.; Jancke, H.; Hoebbel, D.; Wieker, W. Structural Studies on Silicate Anions in Aqueous Solution by Silicon-29 NMR Spectroscopy. *Zeitschrift f{ü}r Chemie* **1974**, *14* (3), 109–110.

(156) Engelhardt, V. G.; Zeigan, D.; Jancke, H.; Wieker, W. ^{29}Si-NMR Spectroscopy of Silicate Solutions. 2. On the Dependence of the Structure of Silicate Anions in Water Solutions from the Na:Si Ratio. *Zeitschrift für Anorg. und Allg. Chemie* **1975**, *418*, 17–28.

(157) Harris, R. K.; O'Connor, M. J.; Curzon, E. H.; Howarth, O. W. Two-Dimensional Silicon-29 NMR Studies of Aqueous Silicate Solutions. *J. Magn. Reson.* **1984**, *57* (1), 115–122.

(158) Kinrade, S. D.; Swaddle, T. W. Silicon-29 NMR Studies of Aqueous Silicate Solutions. 1. Chemical Shifts and Equilibria. *Inorg. Chem.* **1988**, *27* (23), 4253–4259.

(159) Cho, H.; Felmy, A. R.; Craciun, R.; Keenum, J. P.; Shah, N.; Dixon, D. A. Solution State Structure

Determination of Silicate Oligomers by ^{29}Si NMR Spectroscopy and Molecular Modeling. *J. Am. Chem. Soc.* **2006**, *128* (7), 2324–2335.

(160) Haouas, M.; Taulelle, F. Revisiting the Identification of Structural Units in Aqueous Silicate Solutions by Two-Dimensional Silicon-29 INADEQUATE. *J. Phys. Chem. B* **2006**, *110* (7), 3007–3014.

(161) Uhlig, F.; Dortmund, D. Si NMR Some Practical Aspects. *Inorg. Chem.* **2000**, *2* (46), 208–222.

(162) Kinrade, S. D.; Marat, K.; Knight, C. T. G. Longitudinal ^{29}Si Nuclear Magnetic Relaxation in Aqueous Alkali-Metal Silicate Solutions Revisited. **1996**.

(163) Kinrade, S. D.; Swaddle, T. W. Mechanisms of Longitudinal ^{29}Si Nuclear Magnetic Relaxation in Aqueous Alkali-Metal Silicate Solutions. *J. Am. Chem. Soc.* **1986**, *108* (23), 7159–7162.

(164) Barron, P. F.; Frost, R. L.; Skjemstad, J. O. 29Si Spin–lattice Relaxation in Aluminosilicates. *J. Chem. Soc., Chem. Commun.* **1983**, *0* (10), 581–583.

(165) Svensson, I. L.; Sjoberg, S.; Ohman, L.-O. Polysilicate Equilibria in Concentrated Sodium Silicate Solutions. *J. Chem. Soc. Faraday Trans. 1* **1986**, *82* (12), 3635.

(166) Kinrade, S. D.; Swaddle, T. W. Aqueous Silicate Exchange Dynamics and ^{29}Si Nuclear Magnetic Relaxation: The Importance of Protonation Equilibria. *J. Chem. Soc. Chem. Commun.* **1986**, *0* (2), 120.

(167) Kinrade, S. D.; Swaddle, T. W. Silicon-29 NMR Studies of Aqueous Silicate Solutions. 2. Transverse 29Si Relaxation and the Kinetics and Mechanism of Silicate Polymerization. *Inorg. Chem.* **1988**, *27* (23), 4259–4264.

(168) Popat, K. C.; Sharma, S.; Desai, T. A. Quantitative XPS Analysis of PEG-Modified Silicon Surfaces. *J. Phys. Chem. B* **2004**, *108* (17), 5185–5188.

(169) Kojima, C.; Kono, K.; Maruyama, K.; Takagishi, T. Synthesis of Polyamidoamine Dendrimers Having Poly(Ethylene Glycol) Grafts and Their Ability to Encapsulate Anticancer Drugs. *Bioconjug. Chem.* **2000**, *11* (6), 910–917.

(170) Wuelfing, W. P.; Gross, S. M.; Miles, D. T.; Murray, R. W. Nanometer Gold Clusters Protected by Surface-Bound Monolayers of Thiolated Poly(Ethylene Glycol) Polymer Electrolyte [16]. *Journal of the American Chemical Society*. 1998, pp 12696–12697.

(171) Sharma, S.; Johnson, R. W.; Desai, T. A. Evaluation of the Stability of Nonfouling Ultrathin Poly(Ethylene Glycol) Films for Silicon-Based Microdevices. *Langmuir* **2004**, *20* (2), 348–356.

(172) Sharma, S.; Desai, T. Nanostructured Antifouling Poly(Ethylene Glycol) Films for Silicon-Based Microsystems. *J. Nanosci. Nanotechnol.* **2005**, *5* (2), 235–243.

(173) Sharma, S.; Johnson, R.; Desai, T. Ultrathin Poly (Ethylene Glycol) Films for Silicon-Based Microdevices. *Appl. Surf. Sci.* **2003**, *206* (1–4), 218–229.

(174) Xu, Z.; Li, Y.; Zhang, B.; Purkait, T.; Alb, A.; Mitchell, B. S.; Grayson, S. M.; Fink, M. J. Water-Soluble PEGylated Silicon Nanoparticles and Their Assembly into Swellable Nanoparticle Aggregates. *J. Nanoparticle Res.* **2015**, *17* (1).

(175) Sudeep, P. K.; Page, Z.; Emrick, T. PEGylated Silicon Nanoparticles: Synthesis and Characterization. *Chem. Commun. (Camb).* **2008**, No. 46, 6126–6127.

(176) Awad, M. K.; Metwally, M. S.; Soliman, S. A.; El-Zomrawy, A. A.; bedair, M. A. Experimental and Quantum Chemical Studies of the Effect of Poly Ethylene Glycol as Corrosion Inhibitors of Aluminum Surface. *J. Ind. Eng. Chem.* **2014**, *20* (3), 796–808.

(177) Brito, P. S. D.; Sequeira, C. A. C. Organic Inhibitors of the Anode Self-Corrosion in Aluminum-Air Batteries. *J. Fuel Cell Sci. Technol.* **2013**, *11* (1), 011008.

(178) Papra, A.; Gadegaard, N.; Larsen, N. B. Characterization of Ultrathin Poly(Ethylene Glycol) Monolayers on Silicon Substrates. *Langmuir* **2001**, *17* (5), 1457–1460.

(179) Zhang, M.; Desai, T.; Ferrari, M. Proteins and Cells on PEG Immobilized Silicon Surfaces. *Biomaterials* **1998**, *19* (10), 953–960.

(180) Ostaci, R.-V.; Damiron, D.; Al Akhrass, S.; Grohens, Y.; Drockenmuller, E. Poly(Ethylene Glycol) Brushes Grafted to Silicon Substrates by Click Chemistry: Influence of PEG Chain Length,

Concentration in the Grafting Solution and Reaction Time. *Polym. Chem.* **2011**, *2* (2), 348–354.

(181) Norrman, K.; Papra, A.; Kamounah, F. S.; Gadegaard, N.; Larsen, N. B. Quantification of Grafted Poly(Ethylene Glycol)-Silanes on Silicon by Time-of-Flight Secondary Ion Mass Spectrometry. *J. Mass Spectrom.* **2002**, *37* (7), 699–708.

(182) Sofia, S. J.; Premnath, V.; Merrill, E. W. Poly(Ethylene Oxide) Grafted to Silicon Surfaces: Grafting Density and Protein Adsorption. *Macromolecules* **1998**, *31* (15), 5059–5070.

(183) Banik, S. J.; Akolkar, R. Suppressing Dendrite Growth during Zinc Electrodeposition by PEG-200 Additive. *J. Electrochem. Soc.* **2013**, *160* (11), D519–D523.

(184) Li, Y.; Fedkiw, P. S.; A. Khan, S. Lithium / V_6O_{13} Cells Using Silica Nanoparticle-Based Composite Electrolyte. *Electrochim. Acta* **2002**, *47*, 3853–3861.

(185) Cerruti, M.; Fissolo, S.; Carraro, C.; Ricciardi, C.; Majumdar, A.; Maboudian, R. Poly(Ethylene Glycol) Monolayer Formation and Stability on Gold and Silicon Nitride Substrates. *Langmuir* **2008**, *24* (19), 10646–10653.

(186) Liu, F.; Roper, C. S.; Chu, J.; Carraro, C.; Maboudian, R. Corrosion Mechanism and Surface Passivation Strategies of Polycrystalline Silicon Electrodes. *Sensors Actuators, A Phys.* **2011**, *166* (2), 201–206.

(187) Cohn, G.; Ein-Eli, Y. Study and Development of Non-Aqueous Silicon-Air Battery. *J. Power Sources* **2010**, *195* (15), 4963–4970.

(188) Li, J.; He, L.; Liu, T.; Cao, X.; Zhu, H. Preparation and Characterization of PEG/SiO_2 Composites as Shape-Stabilized Phase Change Materials for Thermal Energy Storage. *Sol. Energy Mater. Sol. Cells* **2013**, *118*, 48–53.

(189) Niemöller, A.; Jakes, P.; Eurich, S.; Paulus, A.; Kungl, H.; Eichel, R.-A.; Granwehr, J. Monitoring Local Redox Processes in $LiNi_{0.5}Mn_{1.5}O_4$ Battery Cathode Material by in Operando EPR Spectroscopy. *J. Chem. Phys.* **2018**, *148* (1), 014705.

11. List of figures

Fig. 1: Schematic drawing of transport and transformation processes in a Li-metal vs. graphite battery cell and corresponding current/voltage profiles. 11
Fig. 2: Schematic drawing of transport and transformation processes in a LCO/graphite battery cell and corresponding current/voltage profiles. 13
Fig. 3: Schematic drawing of two possible transport reactions in metal-air cells and discharge current/voltage profile for a Si-air cell. 15
Fig. 4: Schematic drawing of a spin's magnetic moment rotating around the axis of a magnetic field B_0 and CAD drawing of two rf coils for generating an oscillating magnetic field B_1 perpendicular to B_0. 21
Fig. 5: Free induction decay (FID) of a measured NMR signal after a π/2-pulse. 24
Fig. 6: Apodization, zero-filling and Fourier transformation of a FID and processing of the resulting spectrum with phase- and baseline correction. 25
Fig. 7: In-operando NMR spectra in a 2D and a 3D representation. 28
Fig. 8: Peak fitting of overlapping ^{7}Li NMR signals to reveal the intensity integral evolutions of different compounds. 29
Fig. 9: Schematic drawing of the experimental in-operando NMR setup. 31
Fig. 10: History of Li-ion in-operando container appearance. 32
Fig. 11: Schematic drawings of electrode contacting with thin-film conductive layers attached on plastic carriers. 33
Fig. 12: Design of in-operando NMR container. 35
Fig. 13: In-operando NMR container with gas and electrolyte supply for metal-air battery cells. 37
Fig. 14: Thin-film contacting layers for the connection of the air cathode on the inside of the cell chamber. 38
Fig. 15: CAD drawing of an in-house developed in-operando NMR probe. 39
Fig. 16: Modified HPBBHT in-operando NMR probe with connected battery cell container. 41
Fig. 17: Numerically optimized rf saddle coil. 43
Fig. 18: Scanning electron microscope pictures of two 500 nm gold sputter coatings. 51
Fig. 19: Laser scanning microscope measurement of a 100 nm gold layer and sheet resistance of different gold coatings as a function of applied current in a four probe measurement. 52
Fig. 20: Edge height of different gold layers measured with LSM. 53
Fig. 21: Numerical simulations of the B_1 magnetic field strength and comparison of calculated and measured nutation curves for different contacting sticks. 54
Fig. 22: Current rate capabilities of in-operando cell 1 and standard cell 2. 55
Fig. 23: Capacity degradations of the LCO vs. graphite in-operando cells 3 and 4. 56
Fig. 24: Capacity degradations of the LCO vs. graphite in-operando cell 5 and the Li-metal vs. graphite in-operando cell 6. 57
Fig. 25: Post-mortem photographs of the Li-metal vs. graphite cell 6 taken during disassembling. 58
Fig. 26: In-situ EIS of the Li-metal vs. graphite cell 7 during eleven charge/discharge cycles. 59
Fig. 27: ^{7}Li in-operando NMR spectra of the Li-metal vs. graphite battery cell 7. 61
Fig. 28: ^{7}Li in-operando NMR measurement of the first three and a half cycles of a Li-metal vs. graphite battery cell 7. 62

Fig. 29: ^{7}Li in-operando NMR spectra of the Li-metal vs. graphite cell 6 after around 1100 h operation time. 64
Fig. 30: Long-run ^{7}Li in-operando NMR measurements of the Li microstructure formation in the Li-metal vs. graphite cell 6. 65
Fig. 31: ^{7}Li in-operando NMR spectra of the LCO vs. graphite battery cell 9. 67
Fig. 32: ^{7}Li in-operando NMR measurement of the LCO vs. Li-metal cell 8. 68
Fig. 33: ^{7}Li in-operando NMR measurement of the LCO vs. graphite cell 9. 71
Fig. 34: ^{7}Li in-operando NMR measurement during overcharging of the LCO vs. graphite cell 10. 72
Fig. 35: ^{7}Li in-operando NMR measurement of Li plating in the LCO vs. graphite cell 11 at -20 °C. 74
Fig. 36: Schematic drawing of transport and transformation processes in a LCO vs. graphite battery cell during and after Li plating. 75
Fig. 37: ^{29}Si NMR spectrum of 4 M KOH aqueous electrolyte after dissolution of a Si-wafer anode and structural formulas of Si corrosion products. 77
Fig. 38: ^{29}Si ex-situ NMR spectra of Si corrosion products for different KOH solutions. 79
Fig. 39: Time-resolved in-situ ^{29}Si NMR spectra of the silicate formation during corrosion of a Si-wafer in 4 M KOH aqueous electrolyte at 60 °C. 80
Fig. 40: Time-resolved ^{29}Si in-situ NMR intensity evolutions at 60 °C during corrosion of 3 M Si-wafers in 4 M KOH aqueous electrolytes with and without corrosion inhibitor. 81
Fig. 41: Time-resolved ^{29}Si in-situ NMR intensity evolutions at 40 °C and 20 °C during corrosion of 3 M Si-wafers in 4 M KOH aqueous electrolytes without inhibitor. 82
Fig. 42: Comparison of ^{29}Si intensity evolutions during Si-wafer corrosion at 60 °C, 40 °C and 20 °C. 83
Fig. 43: Discharge current/voltage profiles of Si-air cell 12 (outside NMR) and cell 13 (inside NMR). 86
Fig. 44: Second discharge current/voltage profile of Si-air cell 13 during in-operando NMR and photograph of the Si-wafer anode after discharging. 87
Fig. 45: ^{29}Si in-operando NMR measurement of Si-air cell 13. 88
Fig. 46: CAD drawing of a stray field system for 1D high resolution battery imaging. 92
Fig. 47: CAD drawing of a rectangular in-operando NMR cell and Helmholtz rf coil. 107
Fig. 48: Sectional drawing of battery cell container v.3.7 with NMR reference. 108
Fig. 49: Sectional drawing of in-operando NMR cell container concept v.4.1 with reference capsule. 109
Fig. 50: CAD drawing of the low-pass filter box for connection to the probe's battery lines and measured signal attenuation up to 1.5 GHz. 110

12. Appendix

During the work for this thesis many ideas were considered and several promising approaches were prepared only on paper due to the limited time. One prototype is a rectangular cell design for *in-operando* measurements, which could help to improve the signal-to-noise ratio. This is presented in appendix 12.1.
Because one challenge is time-resolved NMR signal referencing during *in-operando* measurement, two new cylindrical cell designs, which address this issue are described in appendix 12.2 and 12.3. Signal filtering of the battery lines is the topic of chapter 12.4.

12.1. Rectangular iOC for metal-air and electrolysis cells

A CAD model of a rectangular *in-operando* NMR cell prototype for metal-air batteries and electrolysis is shown in Fig. 47. The design enables a higher rf coil filling volume than possible for cylindrical cells with separator inserts as used for the presented metal-air cell container (chapter 3.2.3). Moreover 3D-printing can be applied for the cell manufacturing and several supply channels are possible. Inbetween the plastic parts the electrodes and separator foils can be pressed. To avoid shielding of the rf-pulses by the electrodes, the rf-coil can be integrated into the cell container e.g. by thin-film deposition of a conductive path. In addition, it is possible to combine several cell layers and thereby enable cell stags and thus *in-operando* NMR measurements of high voltage batteries.

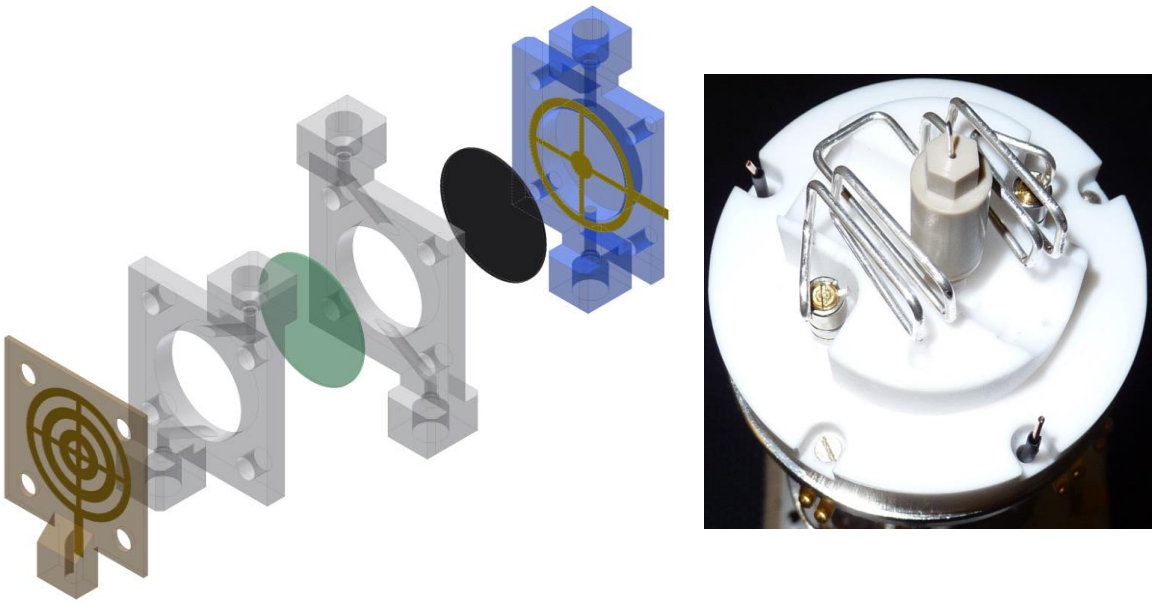

Fig. 47: CAD drawing of a rectangular in-operando NMR cell and Helmholtz rf coil. *Left: For improvement of the coil filling factor and thereby enhancement of the NMR signal, the rectangular iOC could be used in combination with an integrated thin-film deposition coil. A first cell prototype was already made by 3D-printing. Right: The photograph shows a Li-ion iOC v.1.3 in a self-made Helmholtz rf coil. To improve the filling factor for cylindrical cells, saddle coils were used for the version 3 cell containers (Fig. 4, Fig. 17and Fig. 21). In case of a rectangular cell container such a Helmholtz coil could be used for excitation.*

12.2. iOC v.3.7 with segregated NMR reference

For quantitative *in-operando* NMR applications, in which intensity referencing is indispensable, a new version of the *in-operando* container, iOC v.3.7, for Li-ion cells was developed. This containers exhibits the possibility for the integration of a liquid or solid reference material. The high validity of *in-operando* magnetic resonance measurements performed with a (ruby) frequency reference was demonstrated by Niemöller et al.[138], nonetheless EPR was conducted.

The iOC v.3.7 is a modification of the container body of iOC v.3.6 (chapter 3.2.2) and is shown in Fig. 48. The NMR reference is filled in a segregated chamber directly below the cell. This approach requires a container shaft, which provides two connections for the cell contacting and can be realized by using thin-film conductive layers[3]. In addition, such a contacting in combination with plastic inserts opens up the possibility for an integration of a third reference electrode into the container. Moreover, this approach enables the investigation of samples and chemical reactions, which lead to the evolution of hazard gases. Using a container shaft with an exhaust tubing, catching and neutralizing gases outside the NMR becomes possible.

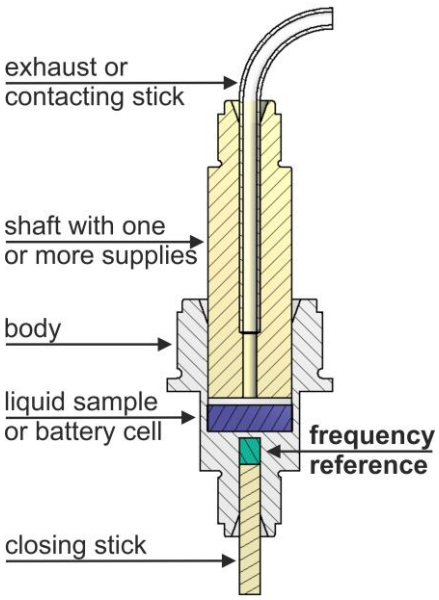

Fig. 48: Sectional drawing of battery cell container v.3.7 with NMR reference. *For an in-operando NMR measurement with reference sample (such as LiCl in water) the container version 3.7 can be used. The reference material (shown in turquois) is filled in a bore close to the inner cell chamber. By using different modifications of the shaft with thin-film coatings the number of electrical connections and supply lines can be adapted. In this figure a hose for exhausting gases resulting from chemical reactions is shown. Instead of this a shaft for Li-ion or metal-air cells can be used as well.*

12.3. iOC v.4.1 with encapsulated NMR reference

For an optimized reproducibility of quantitative *in-operando* NMR applications a new version of the *in-operando* container, v.4.1, for Li-ion cells was prepared on paper. This approach is a modification of the container shaft and shown in Fig. 49. The NMR reference material is filled in a capsule, which is screwed into the modified shaft. Thereby the NMR reference is located above the cell and the container body exhibits, like iOC v.3.6, space for contacting from below. For investigations of spatial magnetic field changes during battery cycling this approach can be extended by adding more or different reference capsules with various distances from the center of the rf coil.

Another extension of iOC v.4.1 is an end stop of the shaft in the body. This end stop enables an exactly reproducible electrode spacing and pressing force in combination with a very easy cell assembly. However, the spacing has to be defined before manufacturing and a set of different shafts with different lengths can be made.

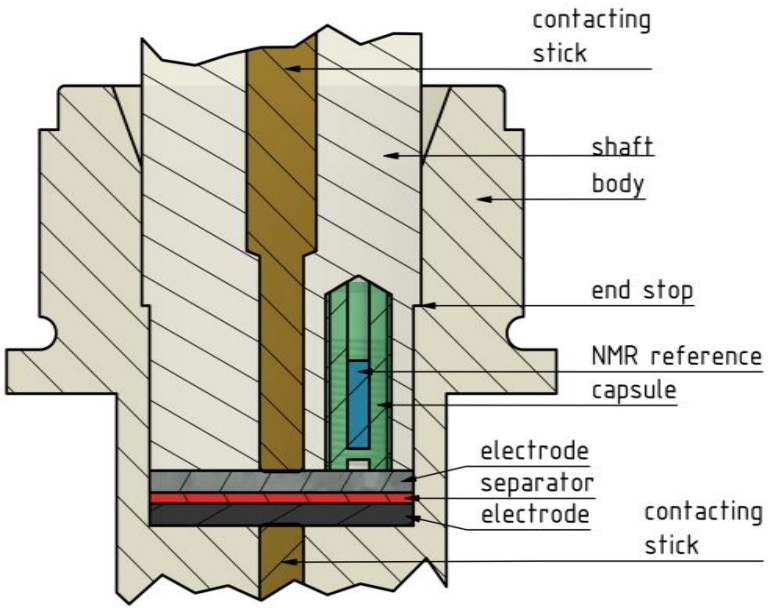

Fig. 49: Sectional drawing of in-operando NMR cell container concept v.4.1 with reference capsule. *For quantitative and highly reproducible in-operando NMR measurements with a NMR reference material the iOC v.4.1 can be used. The reference material (shown in turquois) is filled in a capsule (green), which is screwed into a bore in the shaft close to the inner cell chamber. By using different modifications of the shaft the number of reference capsules can be adapted. An end stop leads to a predefined electrode spacing.*

12.4. Signal filtering of the battery connections

At the bottom plate of the NMR probe semi-rigid cables are connected to low pass frequency filters (API Technologies Spectrum Control 51-311-316) in two shielded boxes (label ⑥ in Fig. 15). Thereby a transmission of signals in the MHz frequency range via the battery cables towards the battery control device is reduced (filter specification: 70 dB @ 1 MHz to 1 GHz). A CAD drawing and the measured attenuation curves of the old and the new self-made filter boxes are shown in Fig. 50. In the old filter box the low-pass filter output was not separated from the filter input by a shielding bridge. Therefore a cross of input and output led to an undesired signal transmission. The resulting SNR in NMR measurements of a Li-metal vs. graphite cell was investigated by averaging 80 FIDs. With connected battery cables but without connected filter boxes, no NMR signal was visible. Therefore the SNR was zero. With disconnected battery cables (and thus disconnected filters and disconnected potentiostat) the maximum signal amplitude after normalization was 0.9997 and a standard deviation (-475 ppm to -462 ppm (100 points)) of 0.00078 was determined. This gives a SNR of approximately 1282. Using the old filter boxes (with connected battery cables (OCV)) a maximum signal amplitude of 0.0218 and a standard deviation (-371 ppm to -365 ppm (100 points)) of 0.00029 was measured. This gives a SNR of approximately 75. With the new filter boxes (with connected battery cables (OCV)) the maximum signal amplitude was 1.0019 and a standard deviation (-475 ppm to -462 ppm (100 points)) of 0.00058 was found. Hence, the new signal filtering enabled a SNR of approximately 1727 and improved the quality of the *in-operando* NMR measurements a lot.

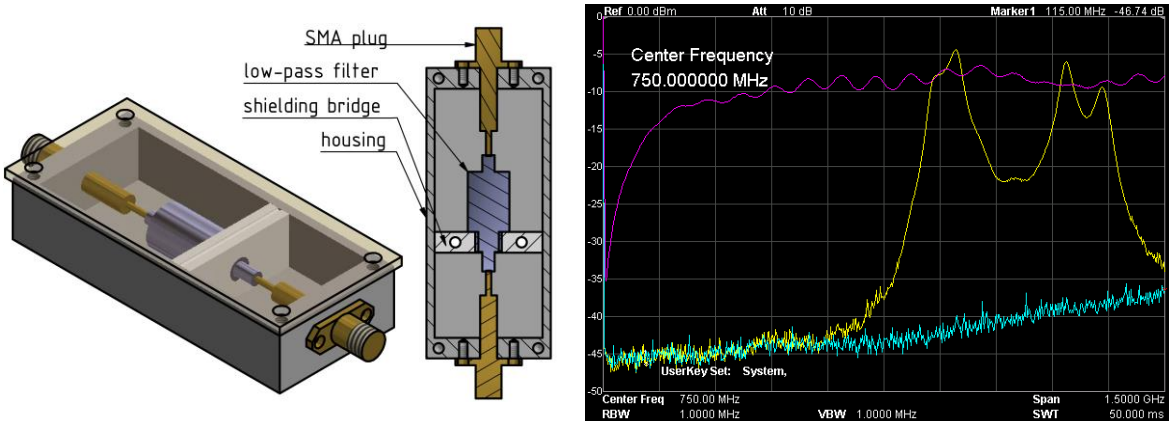

Fig. 50: CAD drawing of the low-pass filter box for connection to the probe's battery lines and measured signal attenuation up to 1.5 GHz. *Left: Input and output of the filter are separated by a shielding bridge to reduce crosstalk. Right: The signal attenuation of the new filter box (yellow) with shielding bridge is much stronger than the attenuation of the old filter box (purple) and hits the noise floor (cyan) for frequencies up to 600 MHz.*